Investigation of Quenching Phenomena on High-Temperature Solid Surface

by

Yutaro Umehara

Submitted to the Department of Mechanical and Intelligent Systems Engineering
in partial fulfillment of the requirements for the degree of
Doctor of Philosophy (Mechanical Engineering)
at the
UNIVERSITY of ELECTRO-COMMUNICATIONS
March 2022

Author .....
Department of Mechanical and Intelligent Systems Engineering

Certified by .....
Kazuhisa Chiba, Co-Supervisor
Professor, University of electro-communications

Certified by .....
Hiroya Mamori
Associate professor, University of electro-communications

Certified by .....
Yasuyuki Takata
Professor, Kyushu university

Certified by .....
Tohru Suzuki
Professor, Tokyo city university

Certified by .....
Tomio Okawa
Professor, University of electro-communications
Thesis Supervisor

Investigation of Quenching Phenomena on High-Temperature Solid Surface

by

Yutaro Umehara

Abstract

The rapid cooling phenomenon for high-temperature objects can be seen in various industrial fields, such as emergency core cooling systems in nuclear power plants and heat treatment in the steel industry. Therefore, industrial fields require two techniques for cooling the high-temperature body. First, a technique to predict the cooling time accurately. It is known that the quenching phenomenon is the key to estimate the cooling time. The quenching phenomenon is that liquid-solid contact starts during the cooling of high-temperature objects and suddenly changes the heat transfer coefficient from low to high. Previous research developed various quenching models to estimate cooling time. However, since it is difficult to observe the quenching phenomenon due to occurring quickly and locally, existing models were not based on the actual quenching phenomenon. Thus, as the models include the experimental parameters, the prediction values were not precise in different experimental conditions. In this study, to define a new quenching model, the details of the quenching phenomenon are elucidated by using a high-speed camera and high-speed Infrared-ray (IR) camera. Moreover, it is confirmed that the new quenching model's prediction value agrees with the previous study's experimental value in $\pm 30\%$. Second, a technique to enhance the cooling performance. Nanofluid is a liquid that contains nanometer-sized particles in a base liquid, such as oil and water. Current researches reported that nanofluid could accelerate the cooling performance by unique quenching phenomenon. Especially, the nanoparticle layer which was formed on the surface during the cooling in nanofluid is the reason. However, the mechanism was not clarified. The present study analyzes the details of the nanoparticle layer (Roughness, Wettability, Wickability, Thickness, etc.). The results show that the low thermal conductivity of the nanoparticle layer leads to high cooling performance. The mechanism is summarized as the new model to predict nanofluid's enhancement ratio. Finally, nanofluid is applied to the coolant for heat treatment. As a result, it is discovered that nanofluid has two important features about heat treatment, uniform, and rapid cooling. However, the hardness of the sample conducted the heat treatment in nanofluid does not show a great difference against pure liquid.

Thesis Supervisor: Tomio Okawa
Title: Professor, University of electro-communications

Acknowledgments

Professor Tomio Okawa: You have taught me over the past six years. It was a pleasure to be one of your students in both the laboratory and classroom. I am pleasure that you gave me a lot of inspirations and idea to continue research activity. It was an honor to have you as my advisor.

Associate professor Koji Enoki: You have taught me over the past six years. I greatly appreciate the time you giving me fruitful advises for experimental set up and the details of research work. This work would not have been possible without your help.

To laboratory members of Okawa & Enoki laboratory from 2016 to 2021: Thanks for all the fun and hope to have a lot more throughout the years.

Family: Thanks for supporting with me throughout the years, I wouldn't be in this position without you guys, and I love you all.

Contents

1 Introduction **17**

1.1 Background 17

1.2 Literature survey 21

1.2.1 Quenching phenomenon during falling liquid film cooling . . . 21

1.2.2 Quenching phenomenon in nanofluids 27

1.3 Objective of this work 32

2 Experimental correlation of heat transfer coefficient distribution during falling liquid film cooling **35**

2.1 Introduction 35

2.2 Experimental methods 36

2.2.1 Experimental apparatus 36

2.2.2 Experimental procedure 38

2.2.3 Experimental condition 38

2.2.4 Calculation method of HTC distribution 39

2.3 Results and discussion 43

2.3.1 Wetting velocity 43

2.3.2 Correlations for the heat transfer coefficient distribution . . . 44

2.4 Calculation of wetting velocity 58

2.4.1 Comparisons of experimental and calculated wetting velocities 58

2.4.2 Prediction of wetting velocity on thicker wall 59

2.5 Conclusions 61

3 Phenomenological interpretation of heat flux distribution in the vicinity of quenching front **63**

3.1 Introduction . . . 63

3.2 Experimental . . . 63

3.2.1 Experimental apparatus . . . 63

3.2.2 Calculation method of wall heat flux distribution . . . 71

3.3 Result and discussion . . . 73

3.3.1 Quenching phenomenon near the liquid film front . . . 73

3.3.2 Relationship between heat flux distribution and liquid film condition . . . 76

3.3.3 The length of sputtering region . . . 77

3.3.4 Parameter effect against critical parameters . . . 83

3.4 New quenching model . . . 85

3.4.1 Validation of new quenching model with current experiment results . . . 87

3.4.2 Validation of new quenching model with previous experiment results . . . 87

3.5 Conclusions . . . 89

4 The Mechanism of Nanofluid Quenching **93**

4.1 Introduction . . . 93

4.2 Experimental descriptions . . . 94

4.2.1 Nanofluid . . . 94

4.2.2 Experimental objects . . . 96

4.2.3 Experimental apparatus and procedure . . . 98

4.2.4 Calculation methods of wall superheat and wall heat flux . . . 100

4.3 Result and discussion . . . 101

4.3.1 Qualitative descriptions of the results of quenching experiment 101

4.3.2 Effects of surface properties on T_{MHF} . . . 111

4.3.3 Effects of the low-thermal-conductivity layer on the heat transfer surface . . . 114
4.3.4 Proposal of a new model for T_{MHF} . . . 120
4.3.5 Conclusions . . . 123

5 Evaluation of the Performance of Nanofluid as Quenching Coolant 125
5.1 Introduction . . . 125
5.2 Literature review . . . 125
5.3 Experimental . . . 126
5.3.1 Temperature distribution measurement experiment in the test piece during immersion cooling . . . 127
5.3.2 Measurement experiment of test piece hardness by aging treatment . . . 127
5.4 Result and discussion . . . 128
5.4.1 Temperature distribution in test piece during immersion cooling 128
5.4.2 Hardness of test piece after aging treatment . . . 129
5.5 Conclusions . . . 134

6 Conclusions and recommended future work 135

Nomenclatures 138

Publications 145

A Estimation of the temperature difference between the two sides of the copper plate 147

B Calculation method of the minimum heat flux point 149

C Uncertainty analysis 151
C.1 Uncertainty of HTC in Chapter 2 . . . 151
C.1.1 The uncertainty of thermal diffusion term . . . 152
C.1.2 The uncertainty of thermal inertia term . . . 154

C.1.3 The uncertainty of temperature difference 156
C.1.4 The uncertainty of HTC 157
C.2 Uncertainty of HTC in Chapter 3 159
C.2.1 The uncertainty of heat flux 159
C.2.2 The uncertainty of temperature difference 160
C.2.3 The uncertainty of HTC in Si 161

List of Figures

1-1 Emergency cooling in nuclear power plant 18

1-2 Boiling curve 20

1-3 Falling liquid film cooling image 22

1-4 Existing models of HTC for quenching phenomenon 24

1-5 Thermal conductivity ratio against volume fraction in water based Al_2O_3 nanofluid [1] 29

1-6 Temperature dependence of thermal conductivity of nanofluid with prediction values (Eqs. (1.14, 1.16)) [2] 29

1-7 Image of the process of forming nanoparticle layer and the nanoparticle layer by single nucleation site [3] 30

2-1 Schematic diagram of the experimental apparatus. 37

2-2 Instantaneous temperature distribution taken by the IR camera (T_{w0} = 300°C, Γ = 0.08 kg/m·s, δ = 0.1 mm) 39

2-3 An example of averaged HTC profile plotted against wall temperature (T_{w0} = 330 °C, Γ = 0.24 kg/m·s, δ = 0.1 mm) 42

2-4 Comparisons of measured wetting velocity with Yamanouchi's equation 45

2-5 Parametric trends of h_{peak} 46

2-6 Parametric trends of ΔT_{wet} 47

2-7 Relation between wall heat flux and wall superheat (boiling curves) . 48

2-8 Correlations for the peak heat transfer coefficient and the wetting temperature 51

2-9 HTC distributions in the wet region 54

2-10 HTC distributions in the dry region 55
2-11 Fitting of HTC distribution 56
2-12 Graphical representation of the proposed correlation for the heat transfer coefficient distribution in comparison with experimental data (T_{w0} = 330°C, Γ = 0.24 kg/m·s, δ = 0.1 mm) 57
2-13 Transient of calculated wetting front position (T_{w0} = 330 °C, Γ = 0.24 kg/m·s, δ = 0.1 mm) 60
2-14 Comparison of the calculated wetting velocities with the experimental data 61
2-15 Variations of the experimental and calculated wetting velocities with wall thickness (T_{w0} = 300°C, Γ = 0.08 kg/m·s) 62

3-1 Experimental apparatus 66
3-2 Wavelength dependence of transmittance in silicon wafers [4] 67
3-3 Wavelength dependence of transmittance in ITO film [5] 67
3-4 Silicon wafer 69
3-5 Silicon wafer of heat transfer plate 70
3-6 Temperature distribution during quenching 71
3-7 Heat flux distribution against wall temperature during quenching phenomenon 73
3-8 Series of synchronized images during quenching phenomenon near liquid film front 75
3-9 The phenomenon in sputtering region during liquid film cooling (High speed camera image, Temperature distribution, and Heat flux distribution from left) 77
3-10 The length of sputtering region in heat flux spatial distribution (T_{w0} = 300 °C, Γ = 0.3 kg/m·s) 79
3-11 Bubble occurrence causes the advancement of liquid film front 80
3-12 Example of bubble size near liquid film front(T_{w0} = 250 °C, Γ = 0.17 kg/m·s) 81

3-13 The length of sputtering region vs bubble size 82
3-14 CHF correlation from Monde's dimensionless equation 84
3-15 Comparison between temperature of CHF and contact temperature . 84
3-16 New quenching model ($T_{w0} = 300$ °C, $\Gamma = 0.28$kg/m · s) 86
3-17 Validation for new quenching model with current experimental results of wetting velocity 86
3-18 Validation for new quenching model with previous experimental results of wetting velocity 90

4-1 Photo of nanofluids used in the present experiments (titanium dioxide, alumina, and silica from the left side). 95
4-2 Geometries of the Inconel 718 specimen (values in parentheses are for the SUS304 specimen) [unit: mm] 97
4-3 Experimental apparatus and procedure 99
4-4 Quenching characteristics of high-temperature test piece in distilled water 102
4-5 Boiling phenomenon during quenching of high-temperature rodlet in distilled water (second run) 104
4-6 Quenching characteristics of high-temperature test piece in silica nanofluid (0.4kg/m^3) 106
4-7 Boiling phenomenon during quenching of high-temperature rodlet in silica nanofluid (second run). (*)1st MHF indicates the ordinary MHF corresponding to boiling transition from film boiling to transition boiling. 107
4-8 Cooling and boiling curves in different nanofluids. 109
4-9 Photos of the test piece taken after the 5th run 110
4-10 Effect of surface roughness Sa on ΔT_{MHF} 112
4-11 Effect of wettability on enhancement of ΔT_{MHF} 112
4-12 Effect of wickability on enhancement of ΔT_{MHF} 114
4-13 Effect of average nanoparticle layer thickness on enhancement of ΔT_{MHF} 118
4-14 Temperature transients calculated using Kikuchi et al.'s model 120

4-15 Temperature history after liquid-solid contact on the silica nanoparticle surface from 1000 °C 122
4-16 Effect of contact time on enhancement of ΔT_{MHF} 122

5-1 Dimension of the test piece (SUS304) 127
5-2 Temperature transients measured at two elevations within the test piece (SUS304, ϕ 15 $\times$ 30 mm) 130
5-3 Transients of temperature difference between the two elevations within the test piece (SUS304, ϕ 15 $\times$ 30 mm) 130
5-4 Transient of test piece (Inconel718, ϕ16$\times$30 mm) temperature during cooling after solution treatment 132
5-5 Hardness of test pieces (Inconel718, ϕ 16 $\times$ 30 mm) measured after aging treatment 133

A-1 Comparison of the temperature profiles on the front and back sides of the copper plate 148

B-1 Boiling curves in distilled water to determine minimum heat flux point 150
B-2 Boiling curves in silica nanofluid to determine minimum heat flux point 150

List of Tables

2.1 Experimental conditions 40
2.2 Thermal properties of the materials of copper plate and black paint . 40

3.1 Contact angle of silicon wafer before experiment [°] 68
3.2 Contact angle of silicon wafer after experiment [°] 68
3.3 Experimental conditions 68
3.4 Experimental condition by Yu et al. [6] 89

4.1 Properties of test piece materials [7] [8] 96
4.2 Parameters used in the Kikuchi model [9] 118
4.3 Properties of the nanoparticle layer materials [10] and water vapor [11] 119
4.4 Estimated properties of the nanoparticle layers 119

5.1 Time-averaged cooling rate 131

C.1 The uncertainty factor of D_1 152
C.2 The uncertainty factor of D_2 153
C.3 The uncertainty factor of thermal diffusion term 154
C.4 The uncertainty factor of I_1 155
C.5 The uncertainty factor of I_2 155
C.6 The uncertainty factor of thermal inertia term 156
C.7 The uncertainty factor of temperature difference 156
C.8 The uncertainty factor of HTC 157
C.9 The uncertainty factor of Q 159
C.10 The uncertainty factor of temperature difference in Si 160

C.11 The uncertainty factor of HTC in Si 161

Chapter 1

Introduction

1.1 Background

The cooling of high-temperature objects in a short time is an essential technology in the industry. In nuclear industries, when severe accidents occur due to loss of coolant accident (LOCA) in light water reactor (LWR), the rapid cooling technique needs to remove the decay heat of nuclear fuels. The meltdown occurred in the Fukushima Dai-ichi nuclear power plant due to the LOCA caused by total loss of power. It was reported that molten fuels melted the pressure vessel and leaked out from the vessel in the power plant after the meltdown. The installation of an emergency core cooling system (ECCS) is considered to prevent LOCA. Spray cooling is one of the emergency core cooling systems. Fig. 1-1(a) shows an overview of the spray cooling system. Coolant injects from the top of the inside pressure vessel, and then coolant falls along the fuel rods to remove the decay heat. When ECCS is not enough to remove the decay heat, nuclear fuels melt by their decay heat. In-vessel retention (IVR) works to keep the molten core in the reactor vessel. Fig.1-1(b) shows overview of IVR. IVR injects the coolant around the pressure vessel to remove the decay heat of the molten fuel through the wall of the pressure vessel. Coolant needs the characteristics of a high heat transfer coefficient. Therefore, understanding the cooling performance of high-temperature objects is essential for the nuclear industry to prevent severe accidents.

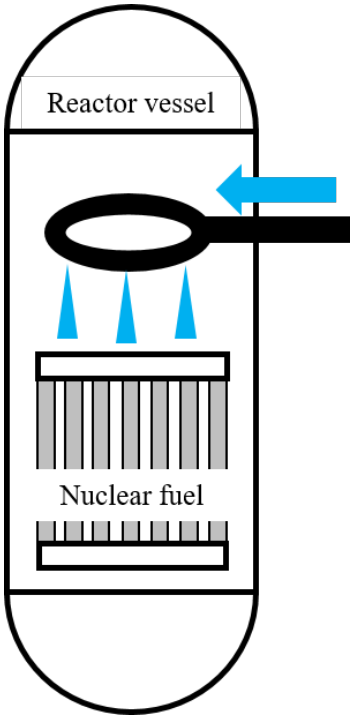

(a) Spray cooling image

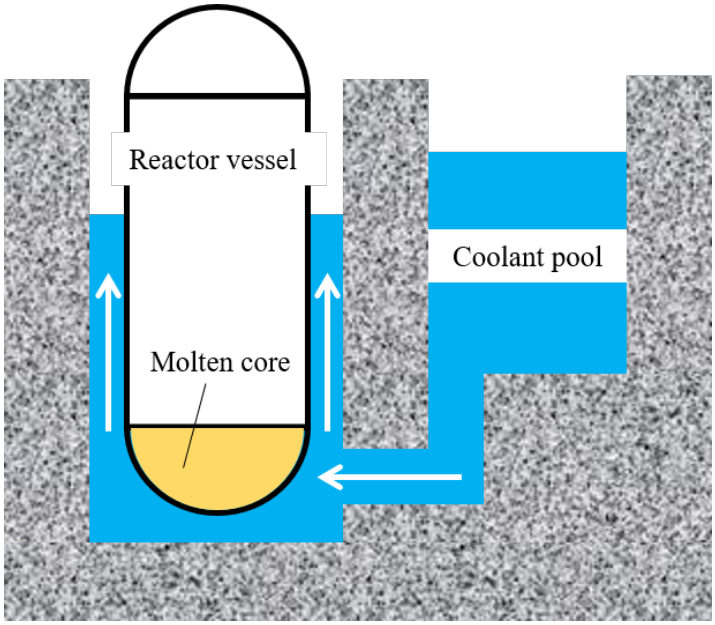

(b) In-vessel retention (IVR) image

Figure 1-1: Emergency cooling in nuclear power plant

In steel industries, the rapid cooling technique plays a significant role in making products. The quenching process is one of the heat treatments for hardening steel

products and is conducted as follows. First, the products keep at a high temperature for a while. Then, the products cool down in a short time. Through the process, the properties of the products are improved, especially hardness. The improvement rate of hardness by the quenching process depends on cooling speed. It is also essential for the steel industry to understand cooling performance to make good products.

From the above example, the cooling technique for high-temperature objects is of great importance in various industries. Thus, many studies have been conducted for heat transfer techniques. The boiling heat transfer technique has been used as one of the high efficient cooling methods and studied for a long time. Nukiyama [12] reported an overview of boiling heat transfer as a boiling curve representing wall superheat against wall heat flux. Figure 1-2 shows the boiling curve in pool boiling that liquid moves only by natural convection, bubble growth, and detachment in the presence of a heating surface in a stationary liquid.

Here explain the characteristics of boiling heat transfer under controlling wall heat flux. When wall temperature is over point A by increasing heat flux, bubbles occur on the heat transfer surface. This boiling mode is called nucleate boiling and leads to a high heat transfer coefficient due to stirring liquid by bubbles. As wall heat flux increases, the number of nucleation sites increases, bubbles make bubble coalescence. Finally, bubble coalescence becomes vapor film and covers the heat transfer surface at point B. This point is called the critical heat flux point (CHF). After that, the wall temperature suddenly escalates from B to D. This phenomenon is called boiling transition and is an important parameter for equipment with boiling heat transfer to determine the heat load limit. At point D, vapor film covers the heat transfer surface. This phenomenon is called film boiling and causes low heat transfer. Next, wall heat flux is decreased from point D. Film boiling continues until the minimum heat flux point (point C). Then, wall heat flux is further reduced, the transition (point C to E) occurs. Finally, nucleate boiling starts at point E. Focusing on the history of the boiling curve, different history exists in increasing heat flux and decreasing heat flux cases. It is called hysteresis. Furthermore, a transition boiling regime is observed from point C to B under controlling wall temperature or cooling of high-temperature

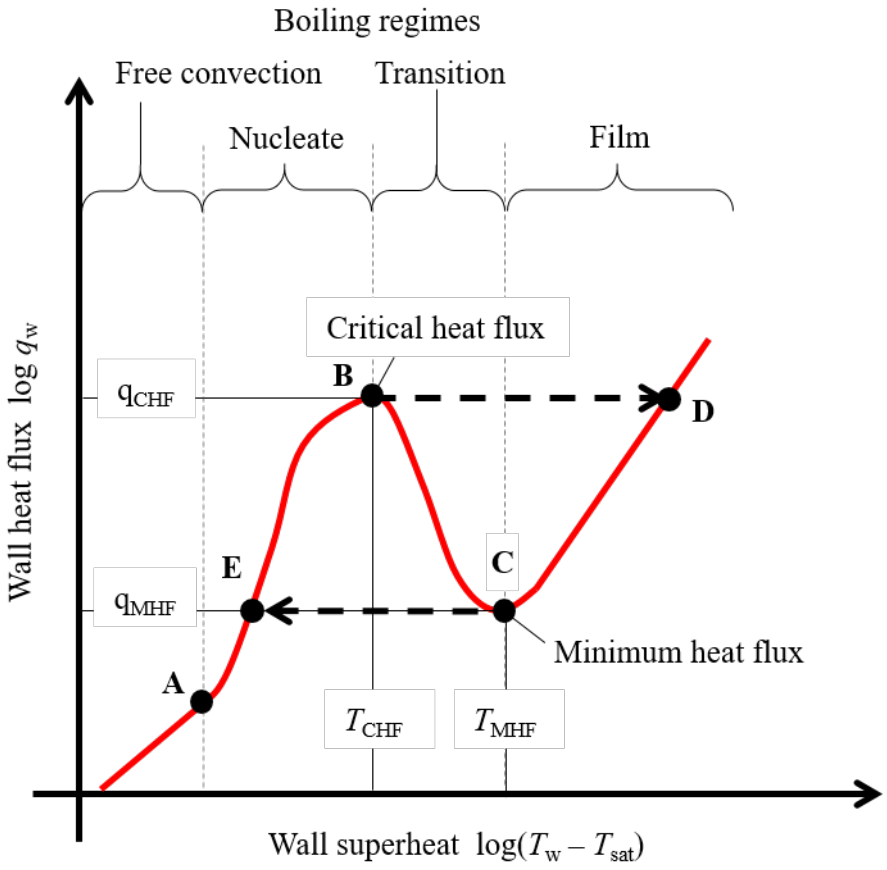

Figure 1-2: Boiling curve

objects. The quenching phenomenon has to do with the transition boiling regime closely.

It is widely known that the quenching phenomenon is the key to predict cooling performance for high-temperature objects. Many studies have been conducted to elucidate the mechanism of the quenching phenomena.

1.2 Literature survey

1.2.1 Quenching phenomenon during falling liquid film cooling

When a liquid film falls along a vertical wall of sufficiently high temperature in Fig. 1-3, a part of the liquid film is spluttered as droplets due to violent boiling caused at the lower edge of the liquid film [13–15]. This phenomenon resembles the Leidenfrost effect [16] that is most commonly observed for the water droplets on a hot pan. In consequence of spluttering, it is known that the lower edge of the liquid film that is called the wetting front, moves in the downward direction more slowly than expected from the free fall assumption [17].

Advancing of quenching front indicates the cooling performance. Here explains the basic idea about the analysis of the velocity of quenching front in Fig. 1-3. The heat conduction equation of the heat transfer plate is represented by

$$\rho c \frac{\partial T}{\partial t} = \frac{\partial}{\partial x}\left(\lambda \frac{\partial T}{\partial x}\right) + \frac{\partial}{\partial y}\left(\lambda \frac{\partial T}{\partial y}\right) + \frac{\partial}{\partial z}\left(\lambda \frac{\partial T}{\partial z}\right) \tag{1.1}$$

where ρ, c, λ, and T is density, specific heat, thermal conductivity, and temperature. To calculate the velocity of quenching front, the following assumptions are applied to the equation.

1. the plate is infinite in z direction.
2. the velocity of quenching front V_{wet} is constant in z direction.
3. the liquid film comes on the surface of which temperature is lower than wetting temperature T_0.

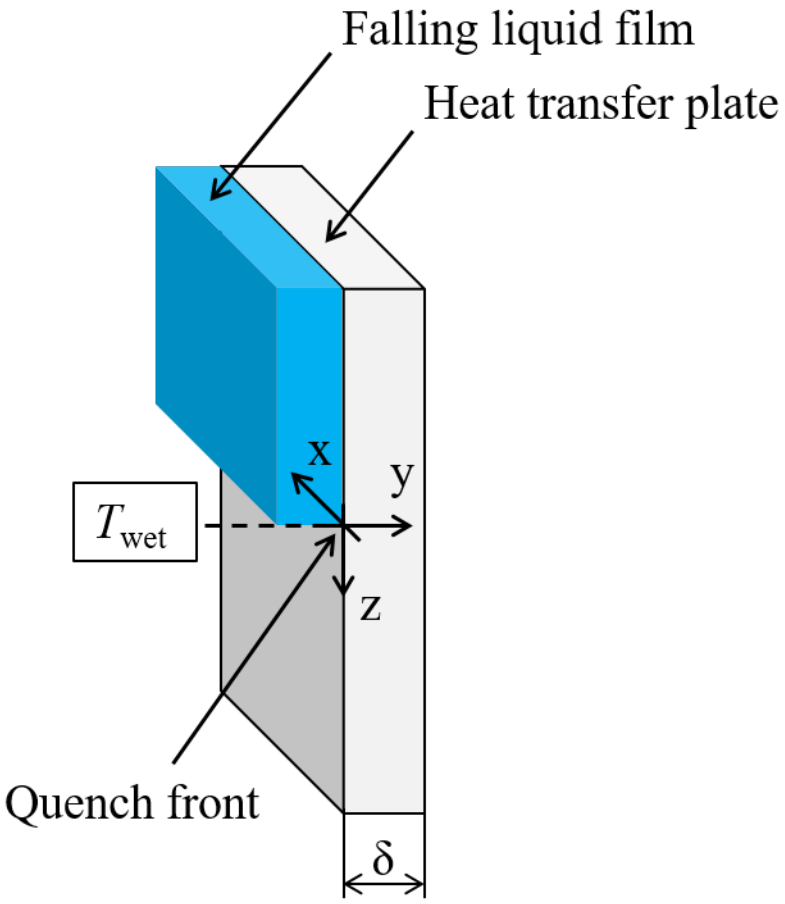

Figure 1-3: Falling liquid film cooling image

4. temperature distribution in x-direction is uniform.

From the assumption of 2, temperature profile also moves with the same velocity, then

$$\frac{\partial T}{\partial t} = -V_{wet}\frac{\partial T}{\partial z} \tag{1.2}$$

From the assumption of 4, and so

$$\rho c\frac{\partial T}{\partial t} = \frac{\partial}{\partial y}\left(\lambda\frac{\partial T}{\partial y}\right) + \frac{\partial}{\partial z}\left(\lambda\frac{\partial T}{\partial z}\right) \tag{1.3}$$

Finally, Eq. (1.1) is transformed to

$$V_{wet}\rho c\frac{\partial T}{\partial z} + \frac{\partial}{\partial y}\left(\lambda\frac{\partial T}{\partial y}\right) + \frac{\partial}{\partial z}\left(\lambda\frac{\partial T}{\partial z}\right) = 0 \tag{1.4}$$

The quenching velocity can be calculated from the above equation by using the four boundary conditions as follows,

1. $T = T_{sat}$ (z = -∞)
2. $T = T_{w0}$ (z = +∞)
3. $\frac{\partial T}{\partial y} = 0$ (y = δ)
4. $-\lambda\frac{\partial T}{\partial y} = h(T - T_{sat})$ (y = 0)

Still, it is not easy to get the quenching velocity due to the following reasons. First, heat transfer coefficient h changes in the direction of z. Second, wetting temperature T_{wet} is affected by the various factors, such as surface condition and property. Previous researches suggested various values about h and T_{wet} as the input parameter to calculate reasonable quenching velocity.

Heat transfer coefficient distribution

Some existing HTC distribution models are summarised in Fig. 1-4. Existing research proposed that HTC distribution is defined as two regions: wet and dry, upper stream and downstream from the quenching front. Yamanouchi [18], Duffey et al. [19], and

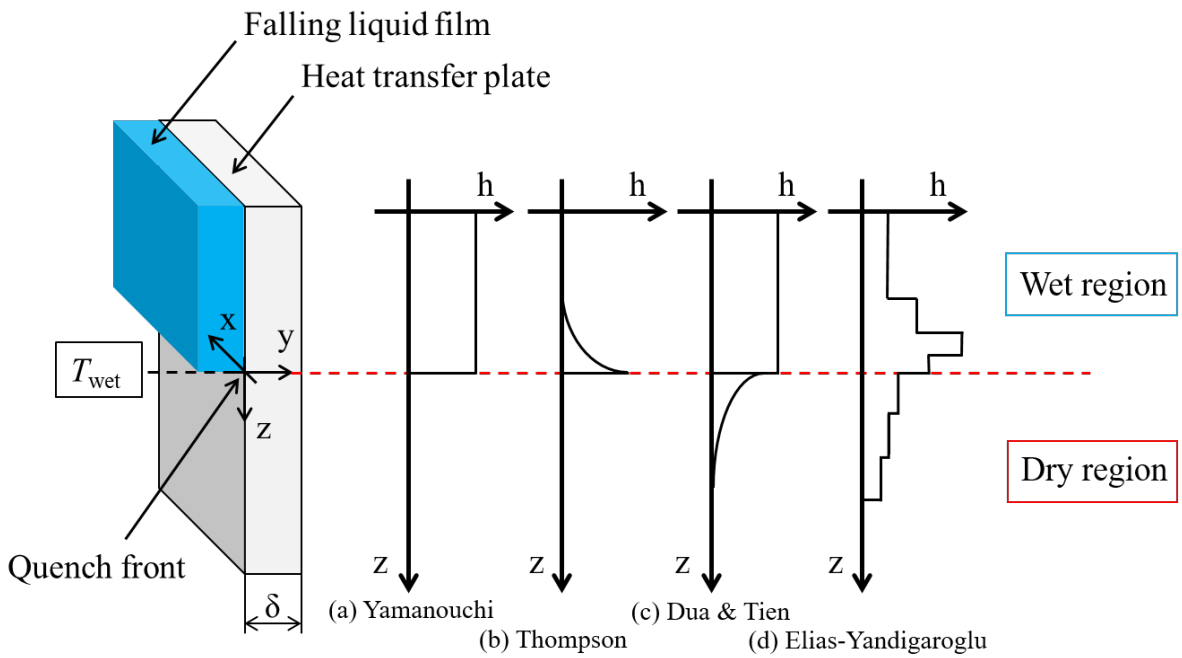

Figure 1-4: Existing models of HTC for quenching phenomenon

Tien et al. [20] designated that HTC distribution can be expressed by two constant values in Fig. 1-4 as follows. HTC in dry region was equal to zero (adiabatic) and in wet region was depended on liquid flow rate G in Eq. (1.5), whereas Blair [21] set constant value ($= 17$ kW/m^2·K).

$$h_{wet} = 4(e^{4.4\Gamma})^2 \tag{1.5}$$

Thompson [22] depicted HTC in dry region as equal to zero (adiabatic) and in wet region had the variation with wall temperature. (Fig. 1-4(b) and Eq. (1.6))

$$h_{wet} = R(1.8T + 32)^3 \tag{1.6}$$

where, R is a parameter that depends on pressure and initial wall temperature. On the other hand, some researchers insisted that precursory cooling effect dominants in the dry region. At the quench front, the liquid film is sputtered away as droplets, and then it contacts the surface in the dry region. And also, droplets change the bulk temperature. As a result, the heat transfer (radiation and conduction) enhances in the

dry region. This cooling mode is called precursory cooling. Dua's model [23] reflected on the effect of precursory cooling as an exponentially decaying HTC distribution in Fig. 1-4(c). HTC in the wet region was a constant value (= 17 kW/m^2·K). HTC in the dry region considered the effect of flow rate that changes the number and size of droplets.

$$h_{dry} = \frac{h_{wet}(T_{w0} - T_{sat})}{N} e^{0.05\tilde{z}} \tag{1.7}$$

$$\tilde{z} = \frac{2\lambda}{\rho c V_{wet}} z \tag{1.8}$$

$$N = \frac{160}{\Psi} + 1 \tag{1.9}$$

where, Ψ is flow rate per unit perimeter (= g/cm·s).

Since two-region models are too simple to express the complex quenching phenomenon, Elias-Yandigaroglu [17] and Sun et al. [24] considered multiple regions of HTC in their models. Elias-Yandigaroglu [17] considered that four different heat transfer modes (simple-phase convection, nucleate boiling, transition boiling, and film boiling) occur during liquid film cooling. In simple-phase convection, a constant convective HTC was applied. The Rohsenow correlation [25] for pool-boiling was used to predict HTC in the nucleate boiling region. The transition boiling HTC was determined by Ramu's correlation [26]. In the film boiling region, Bromley [27] equation was adopted. They applied these values to each region divided by trial and error to obtain an accurate quench velocity.

Wetting temperature

Wetting temperature is the wall temperature at the quench front. This value was determined from two ideas, minimum heat flux (MHF) point, and critical heat flux (CHF) point. First, the MHF point is the wall temperature at which liquid-solid contact begins.

Yamanouchi guessed that wetting temperature is equal to Leidenfrost temperature (= 250°C; copper and water case) from the experiment [18].

Dua's model also selected 260°C which is related with the MHF point [23, 24, 28].

These MHF points were obtained from the experiment. On the other hand, the theoretical models of maximum liquid superheat equal to MHF point were reported.

Spiegler et al. [29] calculated maximum liquid superheat from the Van der Waals equation.

$$T_{\mathrm{MHF}} = \frac{27}{32} T_{crit} \tag{1.10}$$

where, T_{crit} is critical temperature.

Lienhard [30] developed the theoretical model of maximum superheat from thermodynamic theory.

$$\frac{T_{\mathrm{MS}} - T_{sat}}{T_{crit}} = 0.905 - \frac{T_{sat}}{T_{crit}} + 0.095 \left(\frac{T_{sat}}{T_{crit}} \right)^{8} \tag{1.11}$$

where, T_{MS} is maximum liquid superheat.

Berenson [31] expressed the MHF point based on Taylor-Helmholtz hydrodynamic instability as follow.

$$\Delta T_{\mathrm{MHF}} = 0.127 \frac{\rho_v \Delta h}{\lambda_v} \left\{ \frac{g(\rho_l - \rho_v)}{\rho_l + \rho_v} \right\}^{2/3} \left\{ \frac{\sigma}{g(\rho_l - \rho_v)} \right\}^{1/2} \left\{ \frac{\mu_v}{g(\rho_l - \rho_v)} \right\}^{1/3} \tag{1.12}$$

The second idea is that the CHF point is the trigger of sputtering. In the wet region, the main heat transfer mode is considered nucleate boiling. Since the nucleation site reaches a maximum at the CHF point, many bubbles are generated near the liquid film front. The bubbles disrupt the liquid film and peel off liquid film from the surface of the heat transfer plate. Thus, some researchers considered the sputtering phenomenon is dependent on nucleate boiling. J. J. Cabajo [32] considered wetting temperature is equal to CHF point and obtained the correlation from experimental results:

$$\Delta T_{\mathrm{CHF}} = a \Delta T_{sub} + b \tag{1.13}$$

with the following values a = 0.245, b = 29°C for stainless steel rod; a = 4.37, b = 30°C for a 60 mm copper sphere at the atmospheric pressure. And also, Howard [33] and Shires [34] measured wetting temperature (134 °C and 138°C, respectively) which is similar CHF temperature in pool boiling at the atmospheric pressure.

In summary, many correlations were suggested to estimate the quenching velocity and elucidate the quenching phenomenon based on the experiments and theories. These correlations were defined to match the calculated quenching velocity with the experimental value. A new quenching model should involve the background of the real quenching phenomenon to expand the application range.

1.2.2 Quenching phenomenon in nanofluids

A nanofluid is a liquid containing a colloidal dispersion of nanometer-sized solid particles. Three unique features of nanofluid were reported by Das et al. as follows [35].

1. Enhancement of thermal conductivity: the high thermal conductivity is confirmed over pure fluid. This is because nanometer-sized particles can increase the surface area related to heat transfer.

2. Stability: generally, a liquid containing micrometer-sized particles causes aggregation and precipitation due to the particle size, but nanofluid can maintain stable characteristics.

3. Viscosity: viscosity of nanofluid is similar to the base fluid. Thus, additional pressure drop for the cooling system does not need to consider.

These features can be useful to design a new cooling system.

Choi et al. [36] was the first to present the effectiveness of nanofluids for heat transfer systems. Since then, various researches about heat transfer of nanofluid were investigated. First, nanofluid was used to improve the thermal conductivity of fluid for single-phase heat transfer. To enhance the heat transfer in single-phase flow, the high thermal conductivity of the fluid is required. The characteristics of nanofluid match the demand. Lee et al. reported the thermal conductivity of nanofluid is higher than base fluid (Fig. 1-5) [1]. To predict the thermal conductivity of nanofluid, Maxwell model for suspension (Eq. (1.14)) and Hamilton-Crosser model (Eq. (1.15)) were used.

$$\frac{\lambda_{eff}}{\lambda_f} = 1 + \frac{3(\lambda_p/\lambda_f - 1)\phi}{(\lambda_p/\lambda_f + 2) - (\lambda_p/\lambda_f - 1)\phi} \tag{1.14}$$

$$\frac{\lambda_{eff}}{\lambda_f} = \frac{\lambda_p + (n-1)\lambda_f - (n-1)\phi(\lambda_f - \lambda_p)}{\lambda_p + (n-1)\lambda_f + \phi(\lambda_f - \lambda_p)} \tag{1.15}$$

where λ_{eff}, λ_f, λ_p, n, and ϕ depict effective thermal conductivity of suspension, thermal conductivity of fluid, thermal conductivity of particles, shape factor (for shpere = 3, for cylinder = 6), and volume fraction of particles. The prediction values of Hamilton-Crosser model agree with the experimental data in Fig. 1-5. But, the temperature dependence of thermal conductivity is not considered. Jang et al. proposed the model including the effect of the various parameters (temperature and particle size) by considering nanoconvection effect that origins from Brownian motion as follows [2].

$$\lambda_{eff} = \lambda_f(1-\phi) + \beta\lambda_p\phi + C_1\frac{d_f}{d_{nano}}\lambda_f Re^2_{d_{nano}} Pr\phi \tag{1.16}$$

where C_1 is a proportional constant ($= 1.8 \times 10^6$), β is a constant for considering the Kapita resistance per unit area ($= 0.01$). The prediction values agree with temperature dependence of thermal conductivity in Fig. 1-6.

Similarly, various studies have been conducted on pool boiling heat transfer in nanofluid as well [37–44]. Kim et al. showed that the nanofluid deteriorates the nucleate boiling heat transfer coefficient [45]. On the other hand, Wen and Ding reported that alumina nanofluid enhances the nucleate boiling heat transfer [46]. The different effect of nanofluid against boiling heat transfer was reported, but nanofluid certainly improves critical heat flux [37, 38, 44, 47].

The main mechanism of the improvement is considered that the nanoparticle layer, which is formed during nucleate boiling on the heat transfer surface, changes the characteristics of heat transfer surface such as contact angle and wicking performance [48]. Kwark et al. [3] conducted a boiling experiment in alumina nanofluid using copper heat transfer with a single nucleation site to clarify the mechanism of forming a nanoparticle layer. They observed a single circular nanoparticle layer on the heat

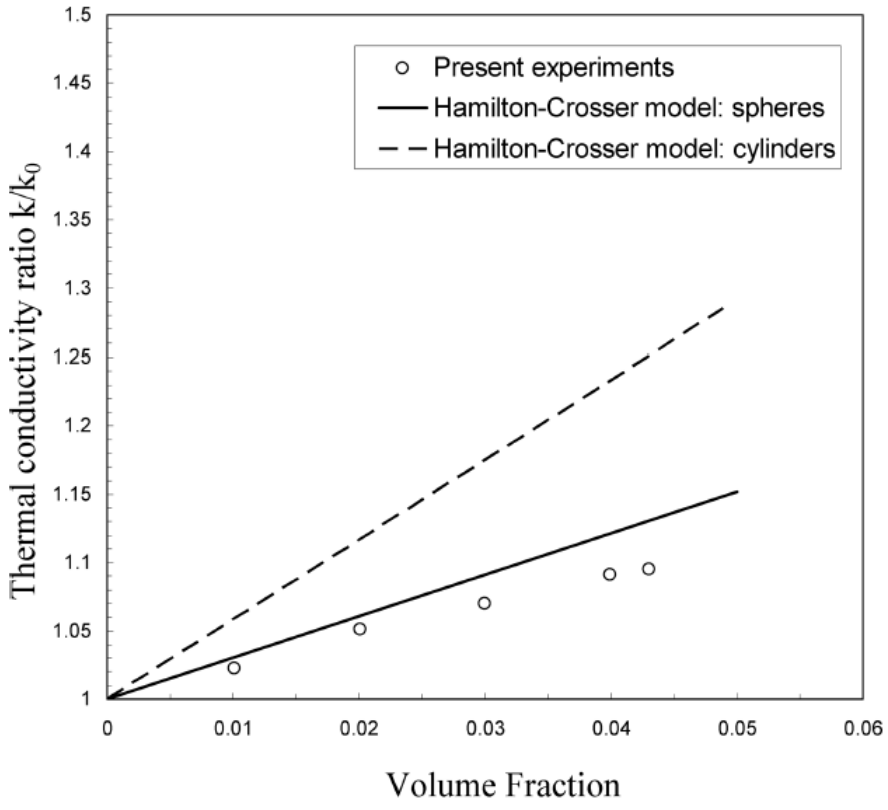

Figure 1-5: Thermal conductivity ratio against volume fraction in water based Al_2O_3 nanofluid [1]

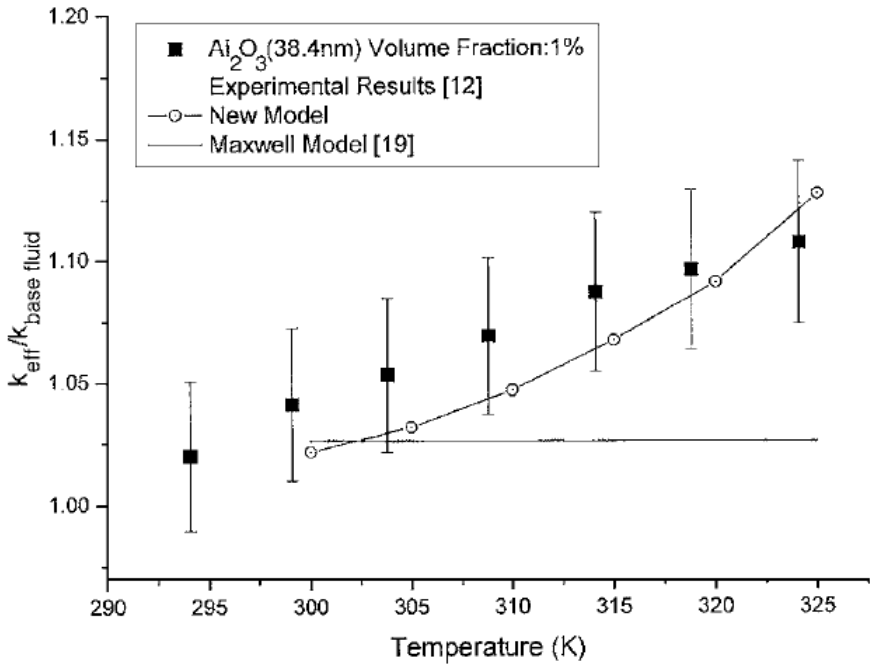

Figure 1-6: Temperature dependence of thermal conductivity of nanofluid with prediction values (Eqs. (1.14, 1.16)) [2]

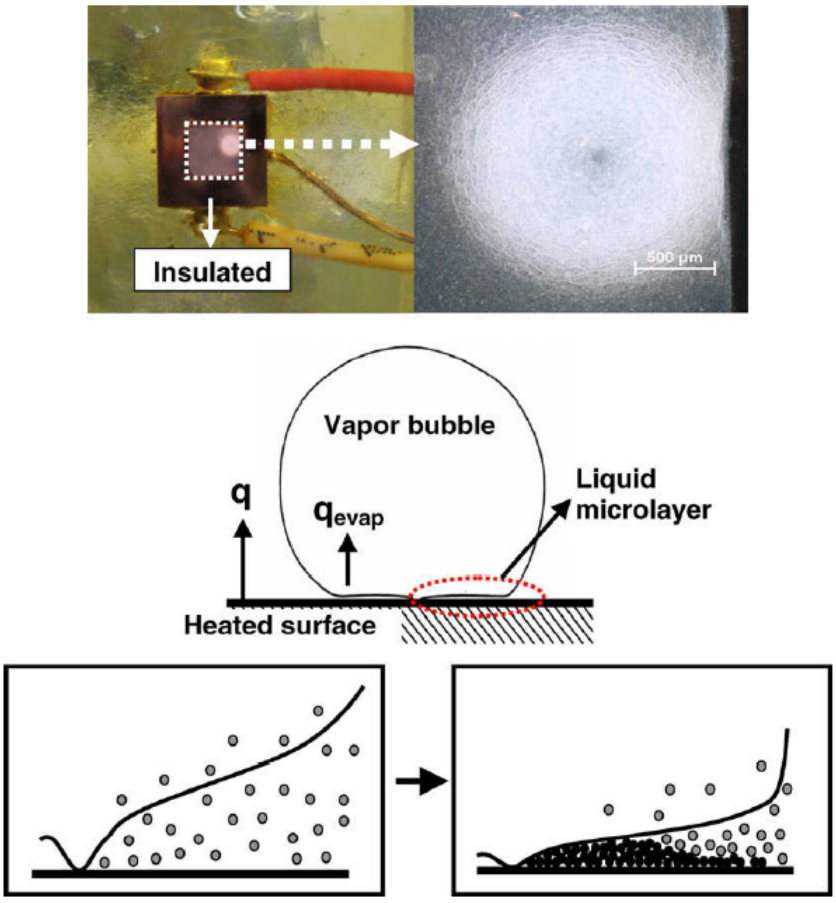

Figure 1-7: Image of the process of forming nanoparticle layer and the nanoparticle layer by single nucleation site [3]

transfer surface. Therefore, microlayer evaporation of boiling produces the nanoparticle layer on the heat transfer surface (Fig. 1-7).

Quenching phenomenon in nanofluid was also investigated [49–51]. As an application of nanofluid in quenching, Kim et al. [49] conducted experiments to obtain boiling curves when high-temperature stainless steel and zircaloy spheres and rodlets were immersed in water-based alumina, silica, and diamond nanofluids. The cooling time was much shorter in the nanofluid than in the pure water except for diamond nanofluid. Moreover, the nanofluid's minimum heat flux point was raised considerably due to the destabilization of vapor film by nanoparticle deposition formed on the surface during the quenching process. However, all nanoparticle deposition did not cause the rapid cooling phenomenon, and nanoparticle materials were also related.

Cloglu et al. [51] investigated quenching behavior in aqueous nanofluids (Al_2O_3, SiO_2, TiO_2, CuO) by high temperature brass rod. Their boiling curve suggested that SiO_2 and TiO_2 nanofluid enhance CHF, and film boiling condition has vanished with repetitive test after the first run. They also found that the nanoparticle layer formed during the repetitive test on the rod and has a porous structure. It is confirmed that the nanoparticle layer caused increasing surface roughness and decreasing contact angle.

That is, nanofluid improves cooling time due to the nanoparticle layer on the surface of high-temperature samples during the quenching process. Other researchers consider the enhancement technique for quenching by modifying the surface characteristics of high-temperature objects.

Kang et al. [52] explored the effects of surface properties on T_{MHF}. Saturated water was used as the test liquid and specimens of three different surface conditions called CWS (Completely Wettable Surface), RZS (Roughness Zirconium Surface), and BZS (Bare Zirconium Surface). It was reported that T_{MHF} was the highest for CWS due to liquid-spreading caused by its high capillary wicking performance.

Kikuchi et al. [9,53] and Chandratilleke et al. [54] investigated the influence of the surface coating on the cooling rate during quenching. If a low thermal conductivity layer covered the heat transfer surface, the contact surface temperature decreased even if the layer was thin. Because of this, Kikuchi et al. [9,53] developed a quenching model considering the change in the surface contact temperature due to surface coating.

If the nanoparticle layer has the same characteristics, the quenching mechanism in nanofluid can be explained in detail.

In summary, the heat transfer characteristics of nanofluid were explored in the case of single-phase, boiling, and quenching. While nanofluid shows the improvement of CHF and the deterioration and enhancement of boiling heat transfer, it is only known that the main cause is the nanoparticle layer, which is formed during boiling. Other enhancement techniques for the quenching phenomenon can help understand the unique quenching phenomenon in a nanofluid.

1.3 Objective of this work

This study has two goals. The first goal is to elucidate the quenching mechanism. Existing quenching models, not based on the quenching mechanism, can not estimate wetting velocity under various experimental conditions since the models included the parameters that reflect the specific experimental results. It is expected that the quenching model, based on the quenching mechanism, can predict exact wetting velocity under various experimental conditions (initial temperature, flow rate, material, etc.). While the precise quenching model is helpful for nuclear power plant safety, it is not enough for the demand of industry fields. Thus, the next goal is set. The second goal is to clarify the mechanism of the enhancement technique of quenching in a nanofluid. If the mechanism of the enhancement technique is clear, the quenching phenomenon can improve in many products. To achieve the objectives, each chapter sets an objective and shows the way of the research as follows.

Chapter 2 describes the experimental apparatus for and results from the study on a new quenching model based on the experimental data. While existing models postulated the HTC distribution and wetting temperature, the present study directly measures temperature distribution during the quenching phenomenon of falling liquid film cooling using a high-speed Infrared camera. Based on the experimental data, a new correlation is presented. Finally, it is confirmed whether quenching velocity calculated using a new experimental correlation agrees with experimental results.

Chapter 3 provides the experimental setup for and results from the study on the quenching phenomenon during falling liquid film cooling. To investigate the details of the quenching phenomenon, a silicon wafer that shows transparency against Infrared rays (IR) is used as a heat transfer wall. The quenching phenomenon is analyzed from synchronized images recorded by a high-speed IR camera and a high-speed camera near the quenching front. The details of the quenching phenomenon and mechanism are clarified by the synchronized images. Finally, a new quenching model is defined based on the actual quenching mechanism.

Chapter 4 indicates the experimental setup for and results from the study on

the quenching phenomenon in a nanofluid. A high-speed camera observes a unique quenching phenomenon. Through the various investigation of nanoparticle layers on high-temperature objects, the reason for the unique quenching phenomenon is clarified by the new model.

Chapter 5 introduces the application of nanofluid in steel industries, especially heat treatment. Observed unique quenching phenomenon in nanofluid is applied to heat treatment of Inconel 718. The effect of the nanofluid is confirmed from the material test.

Chapter 6 summarises this study with the major conclusions. Moreover, future work is recommended.

Chapter 2

Experimental correlation of heat transfer coefficient distribution during falling liquid film cooling

2.1 Introduction

This chapter describes a study of the falling liquid film cooling phenomenon along with a high-temperature copper plate. Heat transfer coefficient (HTC) distribution should be clarified in the flow direction to estimate the velocity of falling liquid film along a high-temperature wall. Especially, HTC distribution in the vicinity of the liquid film front is important to calculate the velocity. Therefore, this chapter determines the experimental correlation of HTC distribution near the liquid front as follows. First, the temperature distribution is measured by an Infrared (IR) camera during the quenching phenomenon. Second, HTC distribution is calculated, and a new correlation is made. Finally, it is confirmed that quenching velocity calculated by new correlation agrees with experimental data.

2.2 Experimental methods

2.2.1 Experimental apparatus

The test section is schematically shown in Fig. 2-1(a). A thin copper plate of 100 mm in width, 85 mm in height, and 0.1-0.5 mm in thickness was used as the heat transfer surface. One side of the plate was painted with a blackbody spray with an emissivity of 0.94 for the temperature measurement using a high speed infra-red camera; the thickness of the blackbody paint layer was measured 20±2 μm. To heat up the plate, each of the left and right edges of the copper plate was sandwiched by two stainless steel 304 square columns. Each column was 20 mm in width and depth and 110 mm in height and contained a 300 W cartridge heater. The distance between the two sets of square columns was 60 mm. It is noted that oxidization of the copper plate surface was unavoidable in the present experiment. Thus, it was fully oxidized prior to the experiment for consistency by keeping the plate temperature at 200 °C for 2 hours. The contact angle of the heat transfer surface was measured 80±7°. The whole picture of the experimental apparatus is depicted in Fig. 2-1(b). The test section was put on bricks of low thermal conductivity placed on a lifter to minimize the heat loss to the base materials. Distilled water was used as the test liquid. It was stored in a storage tank and provided to the test section using a pump via an ultrasonic flowmeter accurate to within ±5 %, the flow control valve, the solenoid valve, and the circular discharge nozzle of 1 mm in diameter. An immersion heater and a type-K thermocouple accurate to within ±2.5 K were installed in the storage tank to heat up the test liquid and to measure the liquid temperature, respectively. A flow control valve was equipped on the bypass line as well as the main line to adjust the liquid flow rate. As depicted in Fig. 2-1(b), the test liquid was provided to the vertical test section as a horizontal jet to form a falling liquid film on the surface where no blackbody-painting was done. The liquid temperature was measured using a type-K thermocouple accurate to within ±2.5 K before being discharged from the nozzle. The spatial distribution of the wall temperature was measured on the blackbody-painted surface using the high-speed infra-red camera (FLIR X6900sc MWIR). The

measurement area was 96 pixels in width and 100 pixels in height and the spatial resolution was 70±3 μm/pixel (field of view was hence 6.7 mm in width and 7.0 mm in height); the error of the temperature measurement was within ±1K (≤100 °C) or ±1% (>100 °C).

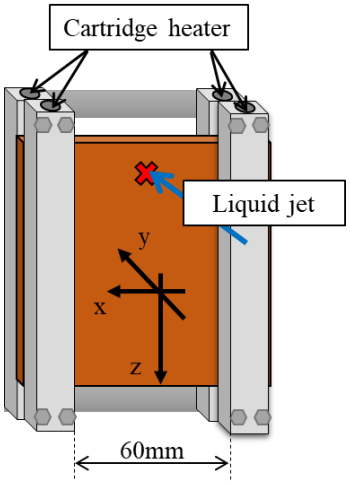

(a) Test section

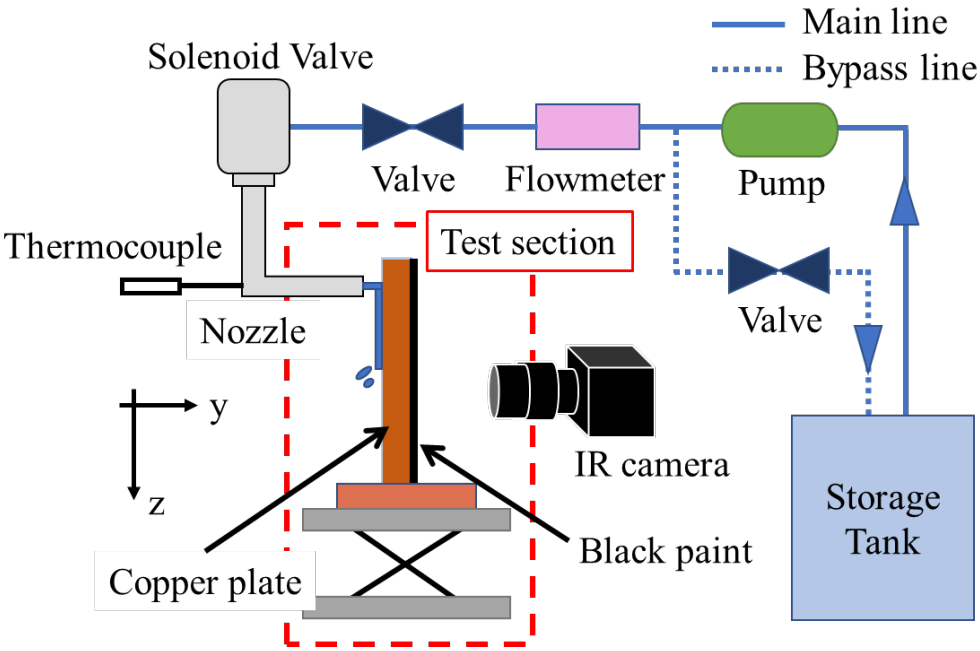

(b) Overall view

Figure 2-1: Schematic diagram of the experimental apparatus.

2.2.2 Experimental procedure

In the experiments, the test liquid in the storage tank was heated to the saturation temperature. Then, the circulation pump was activated and valve openings were controlled to adjust the liquid flow rate at desired value. The solenoid valve was then closed so that all the test liquid was returned to the storage tank via the bypass line. Next, the test section was set on the lifter. The impact point was 12.5 mm from the upper end of the copper plate and the distance between the nozzle and the plate was set to 10 mm. Then, electric power was applied to the four cartridge heaters embedded in the square columns to heat up the vertical copper plate to desired initial temperature. The plate temperature was monitored with the infra-red camera. The upper end of measurement window of the infra-red camera was located at 25 mm below the impact point. When steady state was established, the solenoid valve was actuated to supply the test liquid to the copper plate. The water temperature at the nozzle was measured 93±3 °C due to the heat loss at the flow line. Due to heat transfer to the liquid film, the wall temperature decreased rapidly. Transient of the wall temperature distribution was recorded using the high-speed infra-red camera every 0.5 ms (2000 frames/s). A typical instantaneous temperature profile is presented in Fig. 2-2. It can be seen that sharp temperature gradient greater than 25 K/mm is found around the wetting front.

2.2.3 Experimental condition

As shown in Table 2.1, the three quantities of the copper plate thickness δ, liquid film flow rate Γ, and initial wall temperature T_{w0} were used as the experimental parameters and five series of experiments were carried out. Since the wall temperature was measured from the backside of the plate, a thin plate is advantageous to decrease the measurement error associated with the temperature difference between the two sides of the copper plate. Thus, in the experimental series Nos. 1-4, fixing δ at the minimum value of 0.1mm, Γ and T_{w0} were changed within 0.08-0.32 kg/m·s and 270-360°C, respectively. These data were used as the base data to develop the correlations for the

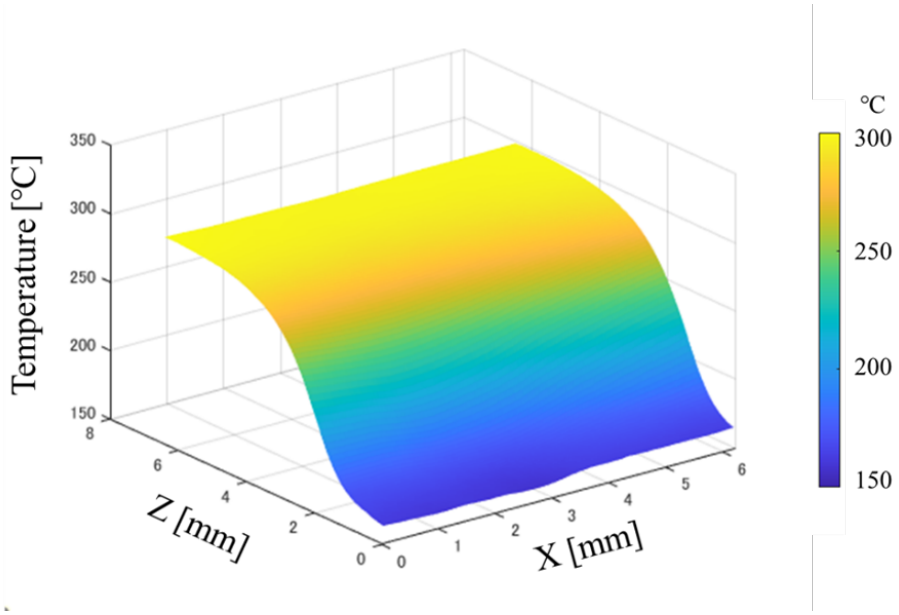

Figure 2-2: Instantaneous temperature distribution taken by the IR camera (T_{w0} = 300°C, Γ = 0.08 kg/m·s, δ = 0.1 mm)

wetting temperature and the spatial distribution of HTC. Then, in the experimental series No. 5, fixing the values of Γ and T_{w0} at 0.08 kg/m·s and 300°C, respectively, the value of δ was increased to 0.3 and 0.5mm to test the applicability of the developed correlations to different plate thicknesses. All the experiments were performed three times to confirm the reproducibility. It is noted that the film flow rate per unit width Γ was calculated from the total film flow rate G by

$$\Gamma = \frac{G}{L_{\text{wet}}} \tag{2.1}$$

where L_{wet} refers the width of wetted area by the liquid film. Although L_{wet} varied within 50±3 mm depending on the experimental condition, the mean value of 50 mm was used in calculating Γ for simplicity.

2.2.4 Calculation method of HTC distribution

Since the thin copper plates of high thermal conductivity were chosen as the heat transfer surface, it was assumed that the Biot number was sufficiently small and the effect of the temperature distribution in the direction perpendicular to the heat

Table 2.1: Experimental conditions

No.	δ [mm]	Γ [kg/m·s]	T_{w0} [°C]
1	0.1	0.08	270-360
2	0.1	0.16	270-360
3	0.1	0.24	270-360
4	0.1	0.32	270-360
5	0.3, 0.5	0.08	300

transfer surface was negligible (see appendix A for the calculation result of Biot number including the effect of blackbody paint layer). Under this assumption, the local values of the heat transfer coefficient h during the wetting process are calculated using the following two-dimension heat conduction equation.

$$h = \frac{\delta \left\{ \frac{\partial}{\partial x}\left(\lambda \frac{\partial T_{\text{wall}}}{\partial x}\right) + \frac{\partial}{\partial z}\left(\lambda \frac{\partial T_{\text{wall}}}{\partial z}\right) - \frac{\partial}{\partial t}\left(\rho c T_{\text{wall}}\right) \right\}}{T_{\text{wall}} - T_{\text{sat}}} \tag{2.2}$$

where t is the time, x and z are the spatial coordinates in the horizontal and downward directions along the heat transfer surface, respectively (see Fig. 2-1(a), ρ and c are the density and specific heat of copper, respectively, T_{wall} is the wall temperature, and T_{sat} is the saturation temperature. The thermal properties of copper and blackbody paint are presented in Table 2.2 [10, 55].

Table 2.2: Thermal properties of the materials of copper plate and black paint

	Density ρ [kg/m^3]	Thermal conductivity λ [W/m·K]	Specific heat c [J/kg·K]
Copper plate	-0.53T+9107 (373<T<773)	0.09T+361 (300<T<1000)	-0.068T+421 (300<T<1000)
Blackbody paint [55](*)	6500	540	18

* Blackbody paint consisted of copper oxide, manganese oxide and chromium oxide, but its properties were assumed equal to those of the main component (copper oxide).

It should be noted that the heat capacity per unit area is estimated about 370 J/m^{2}K for the 0.1 mm-thick copper plate and about 70 J/m^{2}K for the blackbody paint layer, respectively. The heat capacity of the blackbody paint layer is hence not

negligible, but its influence was not taken into consideration in the calculation of h as the first approximation. Validity of this simplification will be discussed later. In order to substitute the temperature data obtained using the infra-red camera, the partial differential terms in Eq. (2.2) were discretized based on the finite difference method. The central difference scheme was applied to the space-derivative terms and the Euler method was used for the time derivative term. The step sizes in time (Δt) and space (Δx and Δz) were same as the temporal and spatial resolutions of temperature measurement using the infra-red camera (Δt = 0.5 ms and Δx = Δz = 70 µm). Assuming that the wall temperature distribution moved downward at a constant wetting velocity V_{wet} without changing its profile, the smooth HTC profile was obtained by averaging instantaneous profiles calculated from 20 successive temperature distribution data. Spatial average in the lateral direction (x-direction) was done in the region where the wetting front line was fairly horizontal. The value of V_{wet} was determined from the displacement of the temperature distribution in the downward direction within 10 ms. A typical example of the resulting time and spatial averaged HTC profile is presented in Fig. 2-3 as a function of wall temperature. It can be seen that in this case, the value of HTC was maximum at the wall temperature of 215 °C. In this study, the peak value of HTC is denoted by h_{peak} and the wall temperature at which $h = h_{\mathrm{peak}}$ is defined as the wetting temperature T_{wet}. It can be seen that the value of HTC decreases gradually both in the dry region of high temperature and the wet region of low temperature. It is noted that several definitions were adopted so far for the wetting temperature or the wetting front temperature T_{wet}. For instance, Cabajo used the wall temperature at the critical heat flux (230 °C) [32] while Yamanouchi used the Leidenfrost temperature (250 °C) [18]. In this work, the wall temperature at which HTC reaches its peak is regarded as T_{wet} since this definition is technically advantageous to develop the correlations to express the HTC profile.

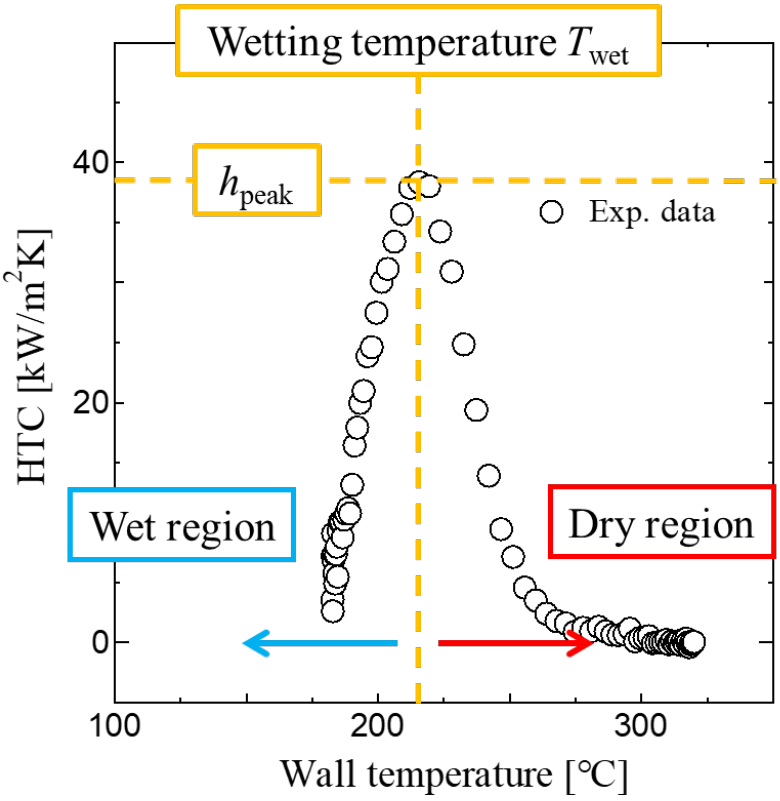

Figure 2-3: An example of averaged HTC profile plotted against wall temperature (T_{w0} = 330 °C, Γ = 0.24 kg/m·s, δ = 0.1 mm)

2.3 Results and discussion

2.3.1 Wetting velocity

Before developing the correlations for the wetting temperature and the HTC distribution, the measured wetting velocities are compared with an existing model. In Figs. 2-4(a) and (b), the experimental values of the wetting velocity V_{wet} are plotted against the initial wall temperature T_{w0} and the film flow rate Γ, respectively. As a simple method to estimate V_{wet}, Ohtake et al. [56] compared their experimental data of V_{wet} with the following equation developed by Yamanouchi [18].

$$V_{wet} = \frac{1}{\rho c}\sqrt{\frac{h_{wet}\lambda}{\delta}}\frac{T_{\mathrm{wet}} - T_l}{\sqrt{(T_{\mathrm{w0}} - T_{\mathrm{wet}})(T_{\mathrm{w0}} - T_l)}} \tag{2.3}$$

where subscript l denotes the liquid phase. The predictions of V_{wet} by the above correlation are also displayed in Fig. 2-4 for comparison. Here, the HTC in the wet region hwet and the wetting temperature T_{wet} contained in Eq. (2.3) were calculated using the following correlations by Yu et al. [6] and Berenson [31], respectively.

$$\sqrt{h_{\mathrm{wet}}}(T_{\mathrm{wet}} - T_l) = 4.52\times10^4\,\{1 + 0.036\Gamma(T_{\mathrm{sat}} - T_l)\}\times(1+1.216\log_{10}P_{ata})^{0.5}\Gamma^{(0.0765/P_{ata})} \tag{2.4}$$

$$\Delta T_{\mathrm{wet}} = 0.127\frac{\rho_v \Delta h}{\lambda_v}\left(\frac{g(\rho_l - \rho_v)}{\rho_l + \rho_v}\right)^{2/3}\left(\frac{\sigma}{g(\rho_l - \rho_v)}\right)^{1/2}\left(\frac{\mu_v}{g(\rho_l - \rho_v)}\right)^{1/3} \tag{2.5}$$

where subscript v denotes the vapor phase, P_{ata} is the pressure in ata, Δh is the latent heat of vaporization, g is gravitational acceleration, σ is surface tension, and μ is viscosity. Figures 2-4(a) and (b) indicate that the value of V_{wet} measured in the present study tended to decrease with an increase in T_{w0} and increase with an increase in Γ. These trends agree with the predictions by Eqs. (2.3) - (2.5). Although the experimental values of V_{wet} are generally smaller than the calculated ones, the discrepancy is within 55%. It may hence be said that considering great uncertainty

in predicting the wetting velocity [56], the present experimental data of V_{wet} are fairly consistent with the above correlations.

2.3.2 Correlations for the heat transfer coefficient distribution

To develop the method to express the HTC distribution in the profile presented in Fig. 2-3, the constitutive equations for h_{peak} and ΔT_{wet} ($= T_{wet} - T_{sat}$) are developed first. The dependences of h_{peak} on T_{w0} and Γ are displayed in Figs. 2-5(a) and (b) and those of ΔT_{wet} are in Figs. 2-6(a) and (b), respectively. It can be seen that an increase in T_{w0} caused a decrease in h_{peak} (Fig. 2-5(a)) and an increase in ΔT_{wet} (Fig. 2-6(a)) and that an increase in Γ caused increases of h_{peak} (Fig. 2-5(b)) and ΔT_{wet} (Fig. 2-6(b)) although the effects of Γ are not always obvious. To understand these parametric trends, the boiling curves showing the relation between the local heat flux q_{wall} and the local wall superheat ΔT_{wall} ($= T_{wall} - T_{sat}$) are displayed in Fig. 2-7; here, the influences of T_{w0} and Γ are explored in Figs. 2-7(a) and (b), respectively. The peak value of q_{wall} in each experimental condition that is referred to as the critical heat flux (CHF) is about within 3-6 MW/m^2. In pool boiling, the wall superheat at the peak heat transfer coefficient ΔT_{wet} is commonly lower than that at ΔT_{CHF} [57]. Figs. **????** and **??** show the dependences of ΔT_{CHF} and ΔT_{wet} on T_{w0} and Γ in the present experiments, respectively. It can be seen that although ΔT_{wet} is slightly lower than ΔT_{CHF} in most cases as expected, parametric trends of ΔT_{wet} are similar to those of ΔT_{CHF}. It is therefore suggested that the present results of h_{peak} and ΔT_{wet} may be compared with available knowledge on CHF. Katto and Ishii experimentally investigated the critical heat flux when a liquid film is supplied along a heated surface to show that the critical heat flux tends to increase with an increase in the liquid flow rate [58]. This is consistent with the present experimental results shown in Fig. 2-7 (b). Mozumder et al. [59] reported that in the quenching process of high-temperature solid surface with a liquid jet, the wall superheat at the maximum heat flux point ΔT_{CHF} increased with an increase in the initial wall temperature but was not influenced noticeably by the liquid flow rate. These trends are also consistent with the present experimental data shown in Figs. 2-7(a) and (b).

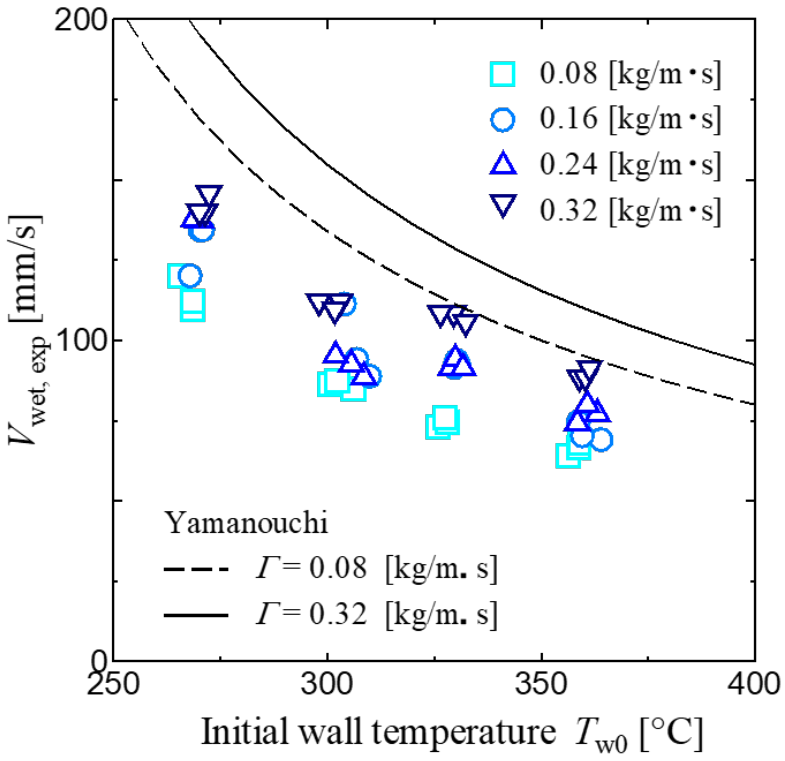

(a) Wetting velocity vs initial wall temperature

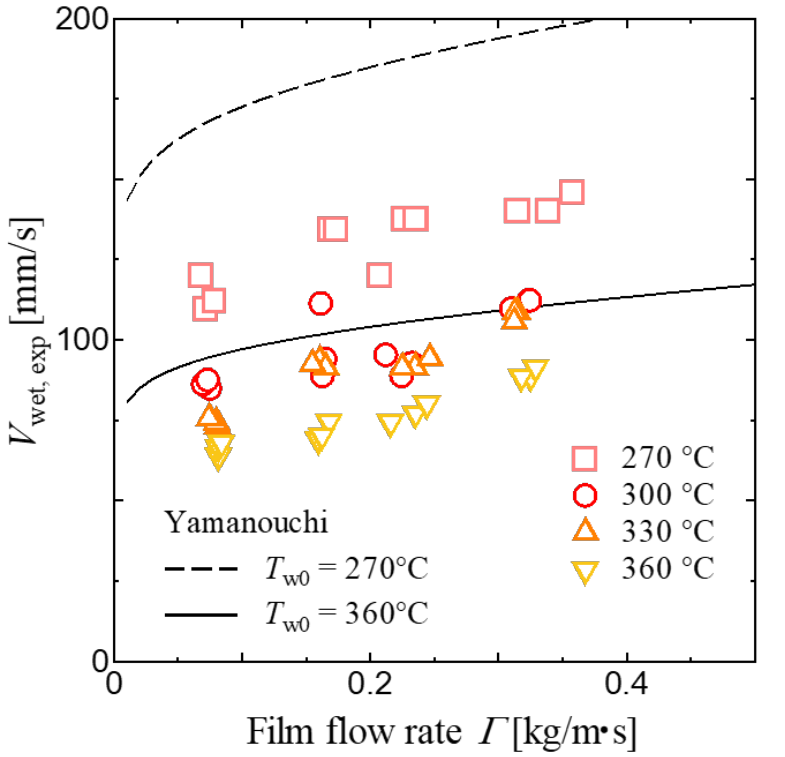

(b) Wetting velocity vs film flow rate

Figure 2-4: Comparisons of measured wetting velocity with Yamanouchi's equation

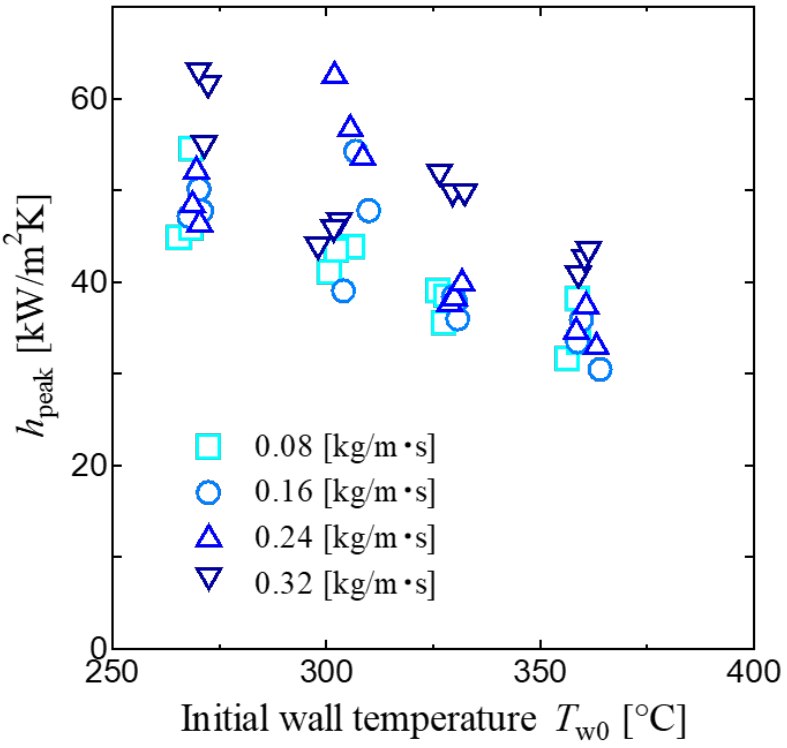

(a) h_{peak} vs initial wall temperature

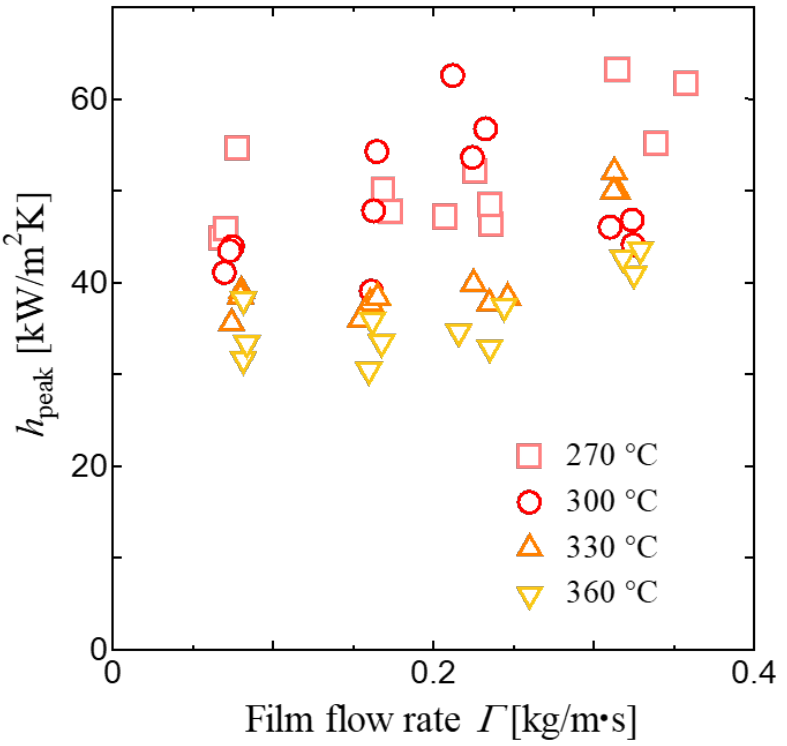

(b) h_{peak} vs film flow rate

Figure 2-5: Parametric trends of h_{peak}

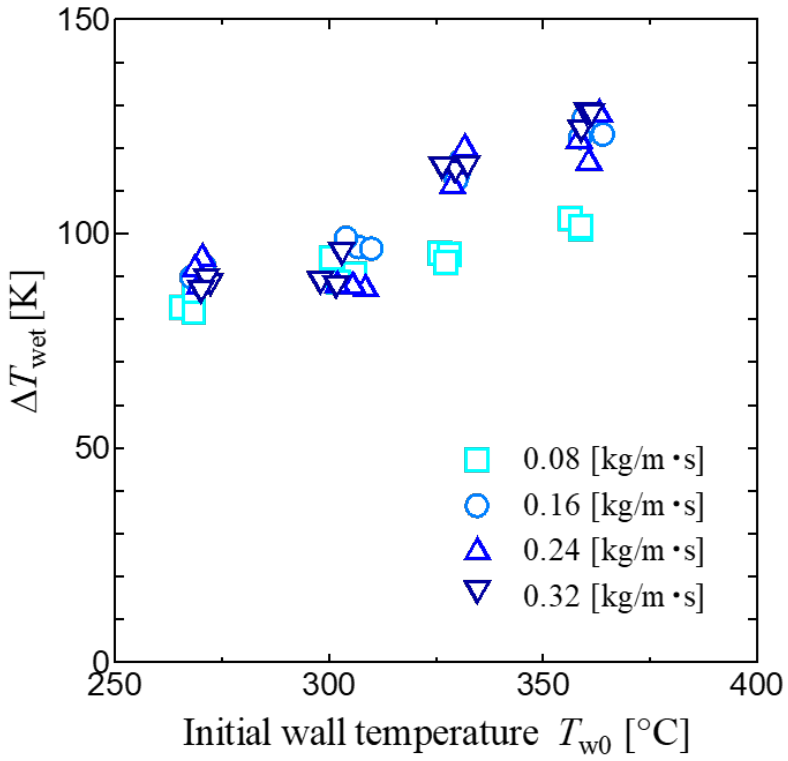

(a) ΔT_{wet} vs initial wall temperature

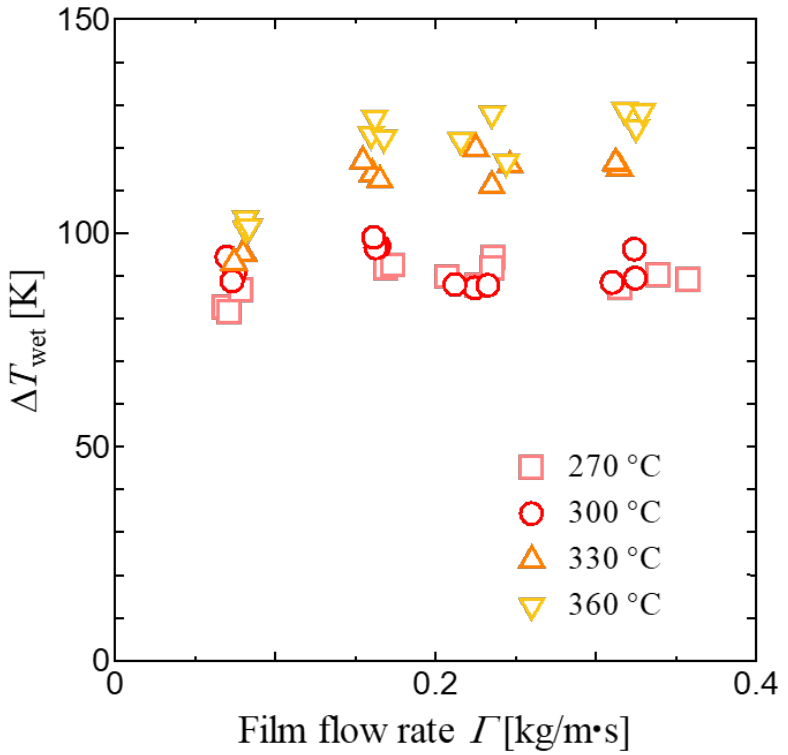

(b) ΔT_{wet} vs film flow rate

Figure 2-6: Parametric trends of ΔT_{wet}

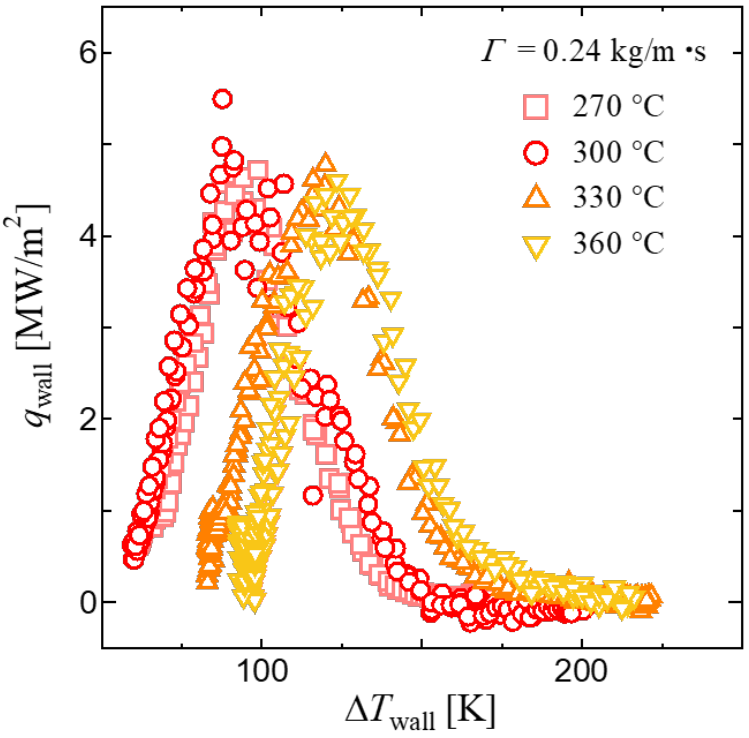

(a) Effect of initial wall temperature (Γ = 0.24 kg/m·s)

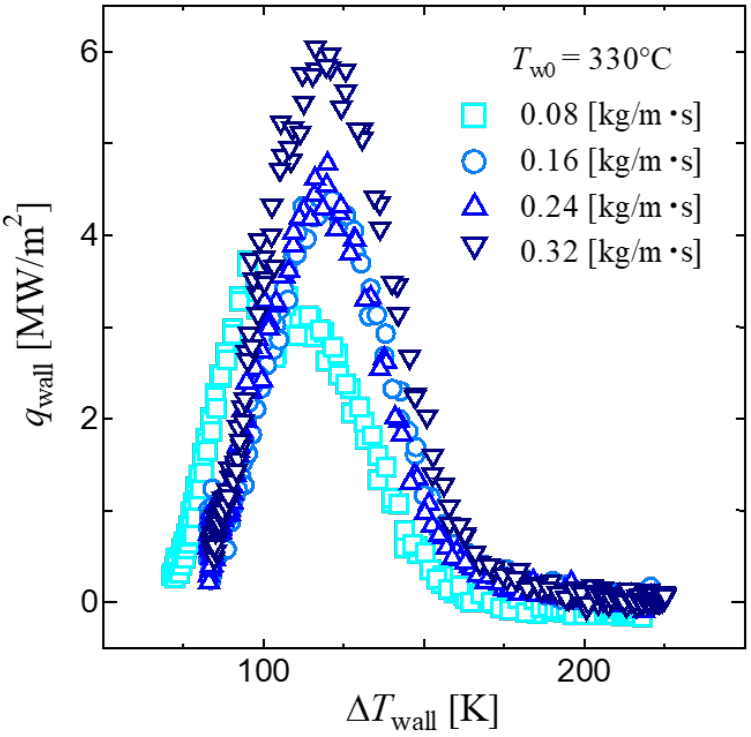

(b) Effect of film flow rate (T_{w0} = 330 °C)

Figure 2-7: Relation between wall heat flux and wall superheat (boiling curves)

To derive empirical correlations for h_{peak} and ΔT_{wet}, dimensionless forms of the heat transfer coefficient and wall superheat are defined by

$$Nu = \frac{hL_a}{\lambda_l} \tag{2.6}$$

$$\theta = \frac{\Delta T}{\Delta T_{\text{wet\_Berenson}}} \tag{2.7}$$

where $\Delta T_{\text{wet\_Berenson}}$ is the wall superheat at the wetting front calculated by the correlation by Berenson (Eq. (2.5)) and the Laplace capillary length L_a defined by the following equation is used as the characteristic length scale in Eq. (2.6) since main heat transfer mechanism in the vicinity of wetting front is considered the nucleate boiling.

$$L_a = \sqrt{\frac{\sigma}{g(\rho_l - \rho_v)}} \tag{2.8}$$

According to Katto and Ishii [58], the Weber number defined by the following equation expresses the effect of film flow rate.

$$We = \frac{\rho_l u_e^2 l_{\text{heat}}}{\sigma} \tag{2.9}$$

where l_{heat} is the length of the heat transfer surface for which the distance between the jet impact point and the center of the measurement window (28.5 mm) is used in the present work, and u_{e} is the liquid film velocity. Denoting the liquid film thickness by d_{film}, u_{e} and Γ satisfy

$$\Gamma = \rho_l u_e d_{\text{film}} \tag{2.10}$$

The following correlations by Nusselt [60] and Takahama and Kato [61] can be used to estimate d_{film} for laminar and turbulent liquid films, respectively.

$$d_{film} = \left(\frac{3}{4}\right)^{1/3} \left(\frac{\mu_l^2}{\rho_l^2 g}\right)^{1/3} Re_L^{1/3} \text{ (for } Re_L \leq 1600) \tag{2.11}$$

$$d_{film} = 0.473 \left(\frac{1}{4}\right)^{0.526} \left(\frac{\mu_l^2}{\rho_l^2 g}\right)^{1/3} Re_L^{0.526} \text{ (for } 1600 \leq Re_L \leq 8000) \tag{2.12}$$

where Re_L is the film Reynolds number ($=4\Gamma/\mu$). After many trials, the following dimensionless correlations were found satisfactory to fit the experimental data of h_{peak} and T_{wet} accumulated in this work as shown in Figs. 2-8(a) and (b), respectively.

$$Nu_{peak} = \frac{h_{peak} L_a}{k_l} = 180\ \theta_{w0}^{-0.82}\ We^{0.12} \tag{2.13}$$

$$\theta_{wet} = \frac{\Delta T_{wet}}{\Delta T_{wet\_Berenson}} = 0.4\ \theta_{w0}^{0.73}\ We^{0.079} \tag{2.14}$$

where $\theta_{w0} = \Delta T_{\text{w0}}$ / $\Delta T_{\text{wet\_Berenson}}$ and the Weber number defined by Eq. (2.9) were used to express the effects of the initial wall temperature and the film flow rate, respectively.

Since wall superheat is one of the most influential parameters in nucleate boiling heat transfer [62], it is assumed that the decreasing trends of HTC from its peak value in the wet and dry regions are expressed as the functions of the dimensionless wall superheat θ^* defined by

$$\theta^* = \frac{\theta}{\theta_{wet}} \tag{2.15}$$

In view of this, the values of Nu scaled by Nu_{peak} in the wet and dry regions are plotted against θ^* in Figs. 2-9 and 2-10, respectively. Here, the effect of initial wall temperature T_{w0} is explored in Figs. 2-9(a) and 2-10(a), and that of film flow rate Γ in Figs. 2-9(b) and 2-10(b). Figures 2-9(a) and (b) indicate that reduction of Nu in the wet region tended to become steeper with an increase in T_{w0} (Fig. 2-9(a)) and a decrease in Γ (Fig. 2-9(b)). On the other hand, Figs. 2-10(a) and (b) show that except for the lowest liquid film flow rate case ($\Gamma = 0.08$ kg/m $\cdot$ s in Fig. 2-10(b)), Nu/Nu_{peak} is expressed as a sole function of θ^* fairly well. The results presented in Figs. 2-9 and 2-10 suggest that the dimensionless wall superheat θ^* is an appropriate

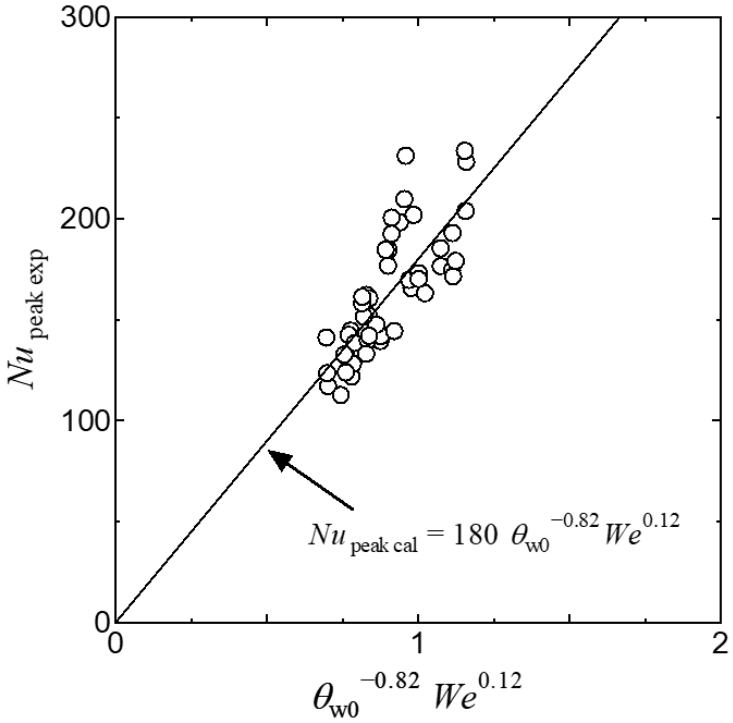

(a) Peak heat transfer coefficient

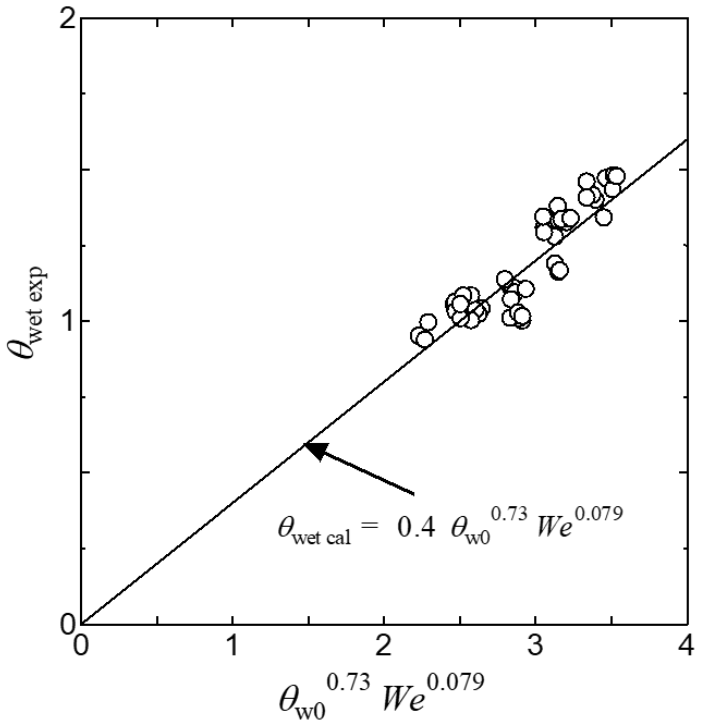

(b) Wetting temperature

Figure 2-8: Correlations for the peak heat transfer coefficient and the wetting temperature

parameter to express the decrease of h from its peak value both in the wet and dry regions since the values of $Nu/Nu_{\rm peak}$ are collapsed fairly well in these figures. Although the influences of $T_{\rm w0}$ and Γ are not negligible particularly in the wet region as shown in Figs. 2-9(a) and (b), the wall is already cooled substantially and the HTC profile in this region is not so influential to the wetting velocity. For this reason, as the first approximation, it is assumed that the profile of $Nu/Nu_{\rm peak}$ is expressed as a sole function of θ^*. All the experimental data of $Nu/Nu_{\rm peak}$ accumulated in this work are plotted against θ^* in Figs. 2-11(a) and (b). From the present experimental data, the following fitting curves are recommended for the wet and dry regions, respectively.

$$\frac{Nu}{Nu_{\rm peak}} = 2.9(\theta^* - 1) + 1 \quad \text{(wet region)} \tag{2.16}$$

$$\frac{Nu}{Nu_{\rm peak}} = 1.06\ exp\left[-\left\{\frac{(\theta^* - 0.91)}{0.37}\right\}^2\right](\theta^* - 1) + 1 \quad \text{(dry region)} \tag{2.17}$$

In the wet region sufficiently upstream of the peak HTC point, heat transfer from the wall is governed by single-phase convection of liquid. Wilke [63] reported that HTC of non-evaporating falling film is expressed using Re_L as

$$h^* = 2.27 Re_L^{-1/3} \text{ (for } Re_L \leq 600) \tag{2.18}$$

$$h^* = 3.23 \times 10^{-2} Re_L^{1/5} Pr^{0.344} \text{ (for } 600 < Re_L \leq 1600) \tag{2.19}$$

$$h^* = 1.02 \times 10^{-3} Re_L^{2/3} Pr^{0.344} \text{ (for } 1600 < Re_L \leq 3200) \tag{2.20}$$

$$h^* = 8.71 \times 10^{-3} Re_L^{2/5} Pr^{0.344} \text{ (for } Re_L > 3200) \tag{2.21}$$

The above equations are used to calculate the minimum value of HTC in the wet region. When the wall temperature is higher than the minimum heat flux temperature $T_{\rm MHF}$, the liquid film cannot touch the wall at all and the heat transfer from the wall to surrounding air is governed by natural convection. Hence, the reduction of wall temperature would be caused mainly by the heat conduction within solid since steep

temperature gradient is formed near the wetting front. The value of h is hence assumed zero when the wall temperature is higher than T_{MHF}. The value of T_{MHF} is estimated by the following correlation by Spiegler et al. [29].

$$T_{\mathrm{MHF}} = \frac{27}{32} T_{\mathrm{crit}} \tag{2.22}$$

where T_{crit} is the critical temperature of the coolant. The present method to estimate HTC distribution during wetting is described graphically in Fig. 2-12 in comparison with the experimental result for $T_{\mathrm{w0}} = 330°\mathrm{C}$, $\Gamma = 0.24$ kg/m·s and $\delta = 0.1$ mm.

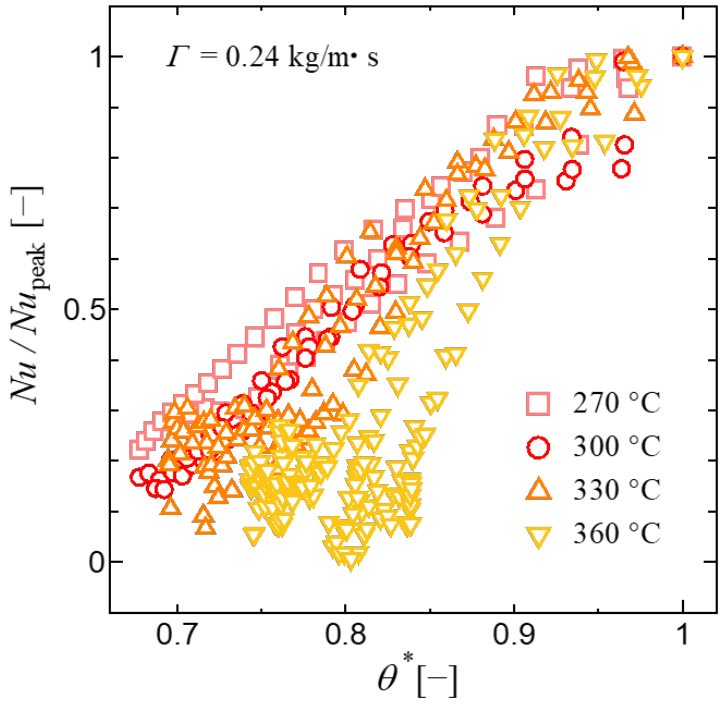

(a) Effect of initial wall temperature ($\Gamma = 0.24$ kg/m·s)

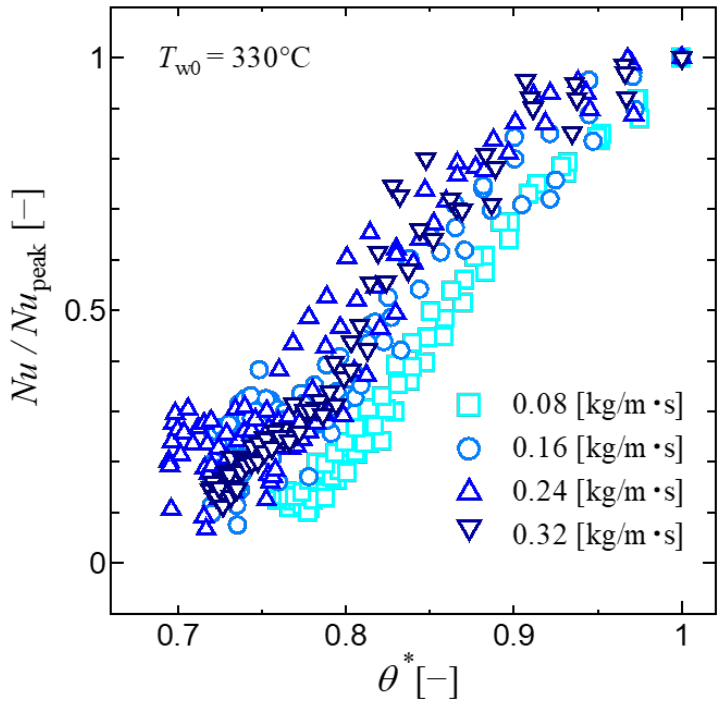

(b) Effect of film flow rate ($T_{w0} = 330$°C)

Figure 2-9: HTC distributions in the wet region

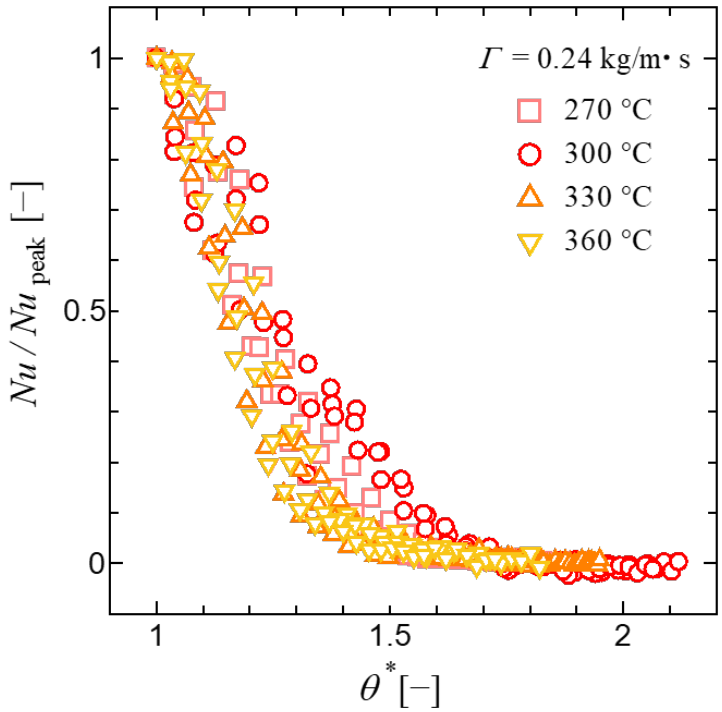

(a) Effect of initial wall temperature ($\Gamma = 0.24$ kg/m·s)

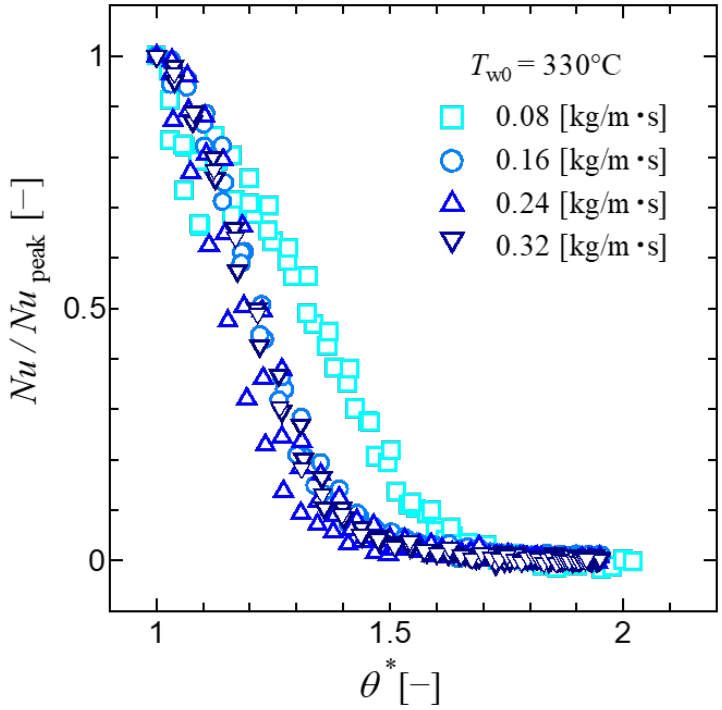

(b) Effect of film flow rate ($T_{w0} = 330$°C)

Figure 2-10: HTC distributions in the dry region

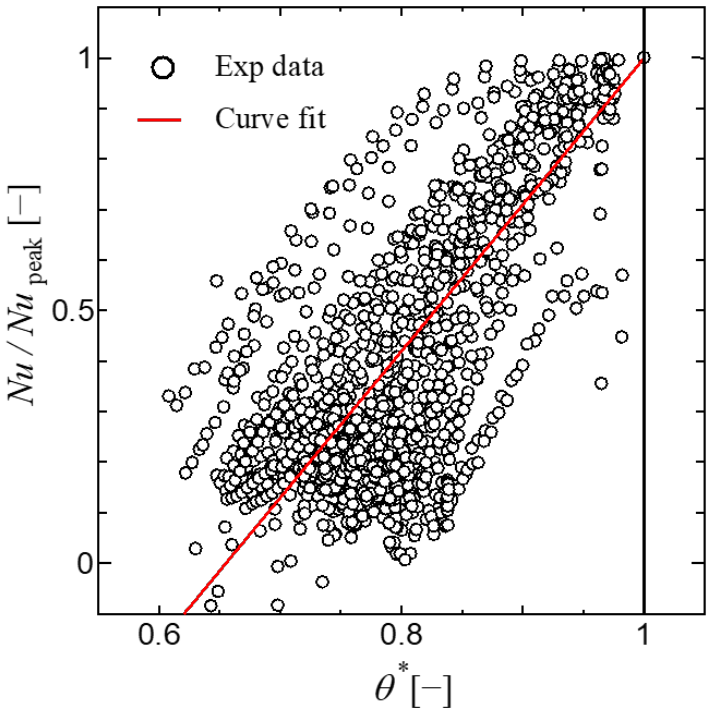

(a) Fitting in the wet region

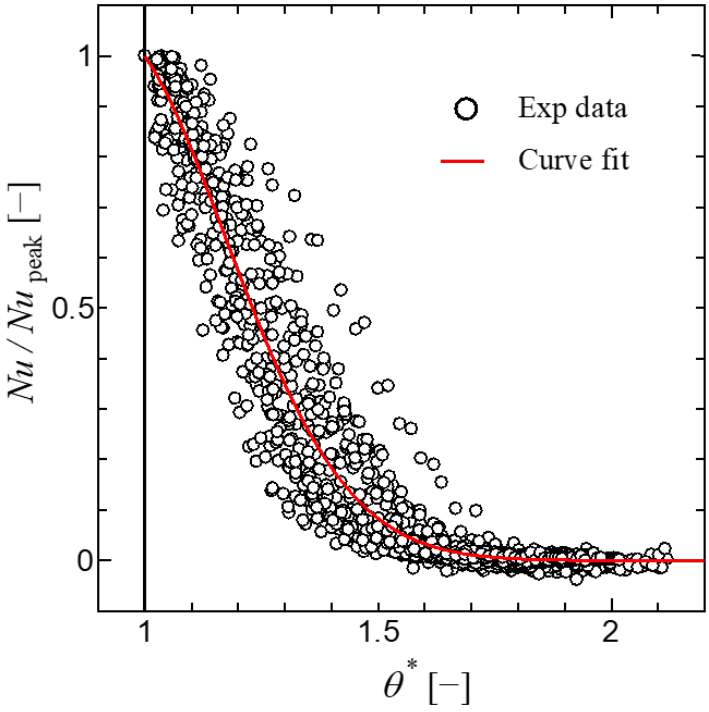

(b) Fitting in the dry region

Figure 2-11: Fitting of HTC distribution

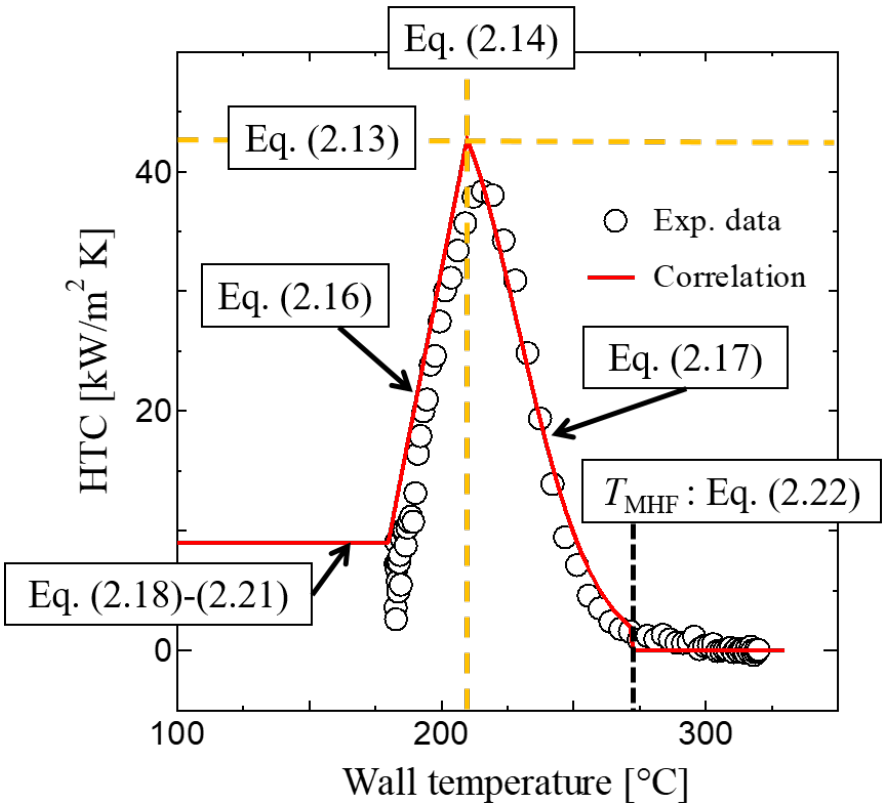

Figure 2-12: Graphical representation of the proposed correlation for the heat transfer coefficient distribution in comparison with experimental data (T_{w0} = 330°C, Γ = 0.24 kg/m·s, δ = 0.1 mm)

2.4 Calculation of wetting velocity

2.4.1 Comparisons of experimental and calculated wetting velocities

The main purpose of the correlations of the HTC profile and the wetting temperature is accurate prediction of the wetting velocity. Therefore, it is confirmed how the proposed correlations can reproduce the wetting velocities $V_{\mathrm{wet,exp}}$ measured in this work. The values of $V_{\mathrm{wet,exp}}$ is calculated using the following two-dimensional heat conduction equation.

$$\rho c \frac{\partial T}{\partial t} = \frac{\partial}{\partial y}\left(\lambda \frac{\partial T}{\partial y}\right) + \frac{\partial}{\partial z}\left(\lambda \frac{\partial T}{\partial z}\right) \tag{2.23}$$

where y is the spatial coordinate in the direction perpendicular to the heated surface. It is noted that the temperature distribution in the y-direction and the presence of the blackbody paint layer were neglected in developing the correlations but they were included in calculating the wetting velocity $V_{\mathrm{wet,cal}}$. The boundary conditions on both faces of the plate are

$$-\lambda \left(\frac{\partial T_{\mathrm{w}}}{\partial y}\right)_{y=0} = h(T_{\mathrm{w}} - T_{\mathrm{sat}}) \tag{2.24}$$

$$\left(\frac{\partial T_{\mathrm{w}}}{\partial y}\right)_{y=\delta+\delta_{BLACK}} = 0 \tag{2.25}$$

Equation (2.24) is the boundary condition for the surface on which the liquid film falls down (y = 0) and the distribution of h is given by the method described graphically in Fig. 2-12. On the blackbody paint layer surface (y = δ+δ_{black}), the adiabatic boundary condition is applied as shown in Eq. (2.25). In the initial condition, the following temperature distribution is assumed within the wall.

$$T = \begin{cases} T_{\mathrm{sat}} & (z \leq 0) \\ T_{\mathrm{w0}} & (z > 0) \end{cases} \tag{2.26}$$

To calculate the wetting velocity, Eq. (2.23) was discretized based on the finite difference method. The explicit Euler method is used for time integration and the central difference scheme is used for the space derivative terms. The mesh size was set to 20 μm in the y and z directions, respectively, and the time step was determined based on von Neumann's stability criterion [64]. It was confirmed that these values are sufficient to achieve mesh size independence of the numerical solutions. The thermal properties of wall materials used in the calculation are shown in Table 2.2. The wetting velocity was derived from the displacement of the maximum HTC point. Fig. 2-13 presents the calculated time variation of the maximum HTC point. It can be seen that the effect of initial condition disappears within 0.05 s and the wetting velocity becomes constant. Thus, the wetting velocity was determined from the displacement of the maximum HTC point within 0.05-0.5 s. The calculated wetting velocities $V_{\mathrm{wet,cal}}$ are compared with the experimental data $V_{\mathrm{wet,exp}}$ in Fig. 2-14. It can be seen that the proposed correlations can predict the present experimental data within the error range of ±20%. This indicates that several simplifications used to derive the correlations for the HTC profile are fairly acceptable.

2.4.2 Prediction of wetting velocity on thicker wall

The present correlations for the HTC distribution and the wetting temperature were developed using the experimental results for the plate of 0.1 mm in thickness to minimize the error associated with the temperature difference between the two faces of the plate. When the plate is thicker, the wetting velocity decreases due to an increase in the heat capacity of the plate [65]. The experimental data of the wetting velocity measured for the thicker plates of δ = 0.3 and 0.5 mm are used to test the applicability of the present correlations to different plate thicknesses. The measured and calculated wetting velocities are compared in Fig. 16. Although noticeable disagreement up to 30% (δ = 0.3 mm) remains, it can be seen that the proposed correlations reproduce the decreasing trend of V_{wet} with an increase in δ fairly well. The values of V_{wet} calculated by Yamanouchi's equation (2.3) combined with Eqs. (2.4) and (2.5) are also shown in Fig. 2-15 with the solid line. It can be confirmed

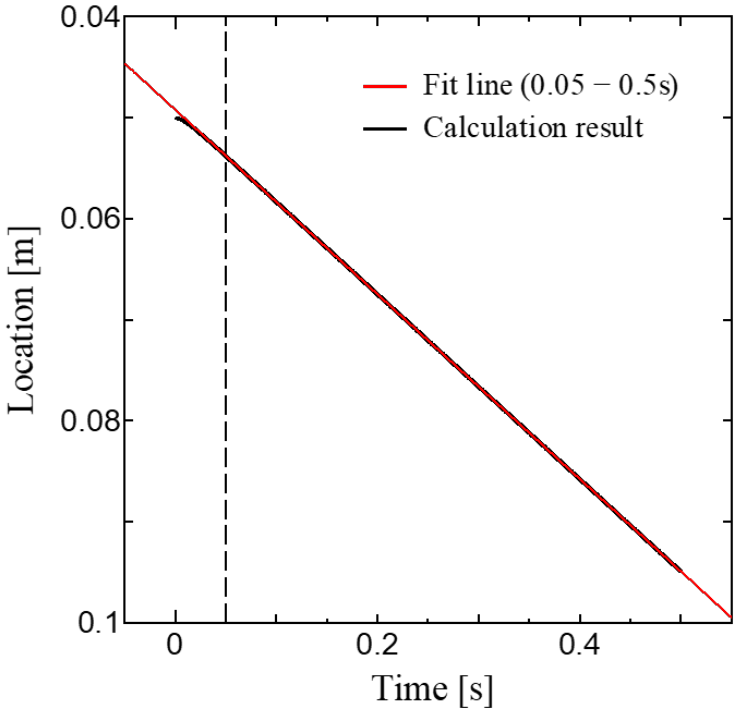

(a) Propagation of the wetting front

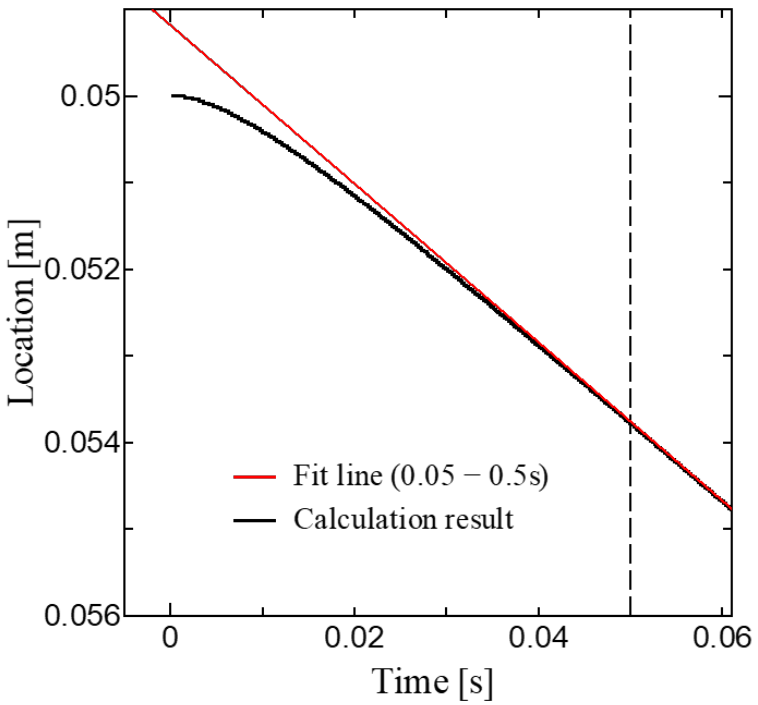

(b) Extended figure

Figure 2-13: Transient of calculated wetting front position (T_{w0} = 330 °C, Γ = 0.24 kg/m·s, δ = 0.1 mm)

that the decreasing trends of V_{wet} with δ in the present experiment and simulation agree with Yamanouchi's equation well.

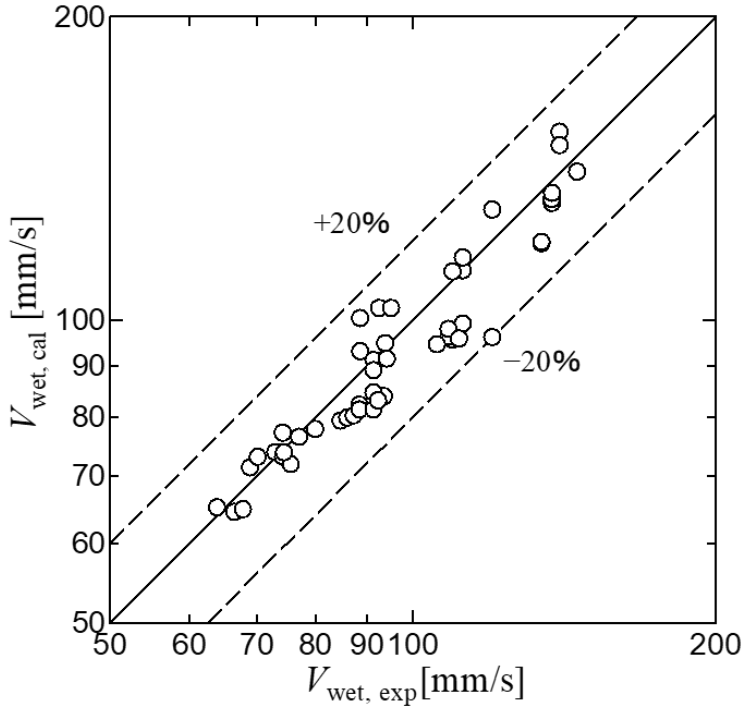

Figure 2-14: Comparison of the calculated wetting velocities with the experimental data

2.5 Conclusions

The present work measured the wall temperature distribution transients during falling liquid film cooling of a hot wall using a high-speed infrared camera. It was shown that the wetting temperature and the spatial distribution of HTC can be derived if the measured temperature distributions are substituted to the heat conduction equation. Using the experimental data accumulated in this work, simple dimensionless correlations were developed for the wetting temperature, the peak value of HTC, and the HTC profiles in the wet and dry regions. Under the experimental conditions tested in this work, the HTC reached its peak near the wetting front and decreased rapidly in upward and downward directions. The wetting temperature and the peak HTC value were correlated as the functions of the initial wall temperature and the liquid film flow

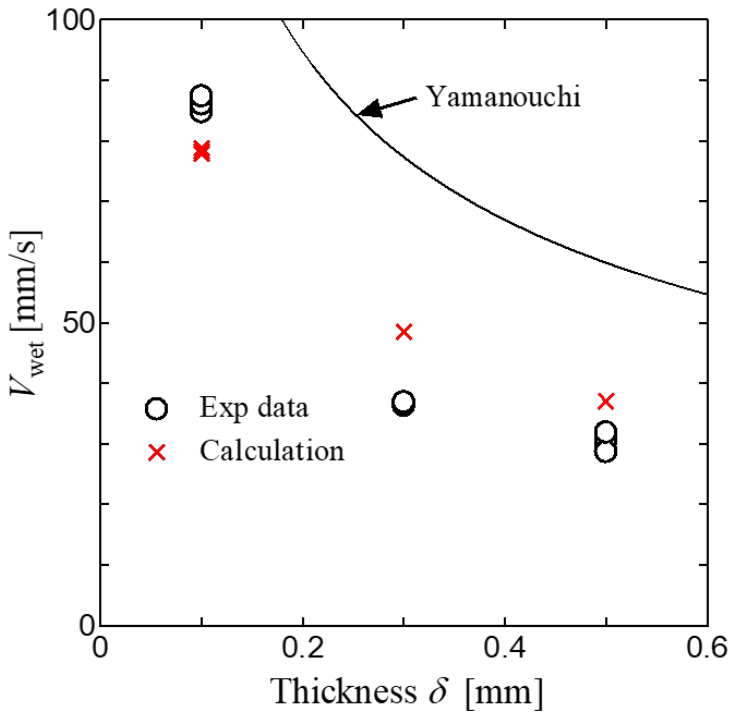

Figure 2-15: Variations of the experimental and calculated wetting velocities with wall thickness (T_{w0} = 300°C, Γ = 0.08 kg/m·s)

rate. The HTC profiles in the dry and wet regions were assumed the sole functions of the wall superheat. In addition, the region where no heat transfer to liquid exists due to high temperature was defined by the available model for the minimum heat flux temperature. It was confirmed that the wetting velocities measured in this work are reproduced by the proposed correlations satisfactorily well.

In comparison with the existing correlations, the proposed correlations developed in this work are advantageous in the viewpoint that they are directly based on the experimental data of the wetting temperature, the peak value of HTC, and the HTC profile. However, it is important to carry out similar experiments under extended conditions of initial wall superheat, liquid flow rate, and wall thickness in future studies. In addition, the effects of other parameters such as the liquid properties, liquid subcooling, wall material, and surface properties of the wall should also be explored.

Chapter 3

Phenomenological interpretation of heat flux distribution in the vicinity of quenching front

3.1 Introduction

In the previous chapter, the quenching phenomenon is expressed using the experimental correlation of HTC distribution. This chapter describes a study of the mechanism of the quenching phenomenon. To clarify the mechanism, the quenching phenomenon, which occurred on a silicon wafer that transmits Infrared rays (IR), is observed with synchronized a high-speed camera and a high-speed IR camera. Based on synchronized images, the main cooling mechanism is elucidated. Finally, new quenching model is defined from observed quenching phenomena as heat flux distribution.

3.2 Experimental

3.2.1 Experimental apparatus

The test section is schematically shown in Fig. 3-1. Silicon wafer (4inch in diameter, $\delta = 0.525$ mm) that sputtered Indium-Tin-Oxide (ITO) film and SiO_2 film was used

for heat transfer plate. Silicon wafers are transparent in mid-Infrared rays (IR) (3 to 5 µm), and the transmittance of the silicon wafer is a constant value (= 0.53) during the range of wavelength in Fig. 3-2. In this experiment, ITO film that was often used to shut out IR was sputtered on one side of the silicon wafer. Figure 3-3 shows the transmittance of ITO film against wavelength and that ITO film is opaque in the mid-IR spectrum. The thickness of ITO film was 0.16 µm that was thick enough to shut out IR and thin enough to neglect temperature gradient in the layer. Since wettability of ITO film was low (contact angle against water: $\theta \simeq 70^\circ$ [66]), SiO_2 film (= 0.52 µm) was sputtered on ITO film to improve wettability. Silicon wafer has two characteristic surfaces, mirror surface and satin surface in Fig. 3-4. In the preliminary test, wettability was investigated on the different base surfaces by using PG-X FIBRO systemAB. Figure 3-5 shows that sputtered ITO and SiO_2 film on the silicon wafer of mirror and satin surface. It is confirmed that the unevenness of surface color does not affect surface condition in Fig. 3-5(b). Wettability was measured before the quenching experiment in Table 3.1. As a result, sputtered SiO_2 film improved wettability, and the wettability of SiO_2 film on the satin surface was better than on mirror film. After the quenching experiment, wettability was confirmed in Table 3.2. Wettability of SiO_2 film on mirror surface deteriorated, on the satin surface, however, kept zero degrees contact angle after quenching experiment. Therefore, this study used a silicon wafer that sputtered ITO film and SiO_2 film on a satin surface as a heat transfer plate.

To heat the plate, each of the left and right edges of the silicon wafer was sandwiched by two stainless steel 304 square columns. Each column was 20 mm in width and depth and 110 mm in height and contained a 300 W cartridge heater. The distance between the two sets of square columns was 60 mm. The whole picture of the experimental apparatus is depicted in Fig. 3-1(a). The test section was put on bricks of low thermal conductivity placed on a lifter to minimize the heat loss to the base materials. Distilled water was used as the test liquid. It was stored in the storage tank and provided to the test section using the pump via the ultrasonic flow-meter accurate to within ±5%, the flow control valve, the solenoid valve, and the

circular discharge nozzle of 1 mm in diameter. An immersion heater and a type-K thermocouple accurate to within ±2.5 K were installed in the storage tank to heat the test liquid and to measure the liquid temperature, respectively. A flow control valve was equipped on the bypass line and the mainline to adjust the liquid flow rate. As depicted in Fig. 3-1(a), the test liquid was provided to the vertical test section as a horizontal jet to form a falling liquid film on the surface where sputtered ITO and SiO_2 film was done. The liquid temperature was measured using a type-K thermocouple accurate to within ±2.5 K before being discharged from the nozzle. The spatial distribution of the wall temperature was measured on ITO film through a silicon wafer from the backside using the high-speed infra-red camera (FLIR X6900sc MWIR). The measurement area was 96 pixels in width and 100 pixels in height, and the spatial resolution was 75±3 µm/pixel (field of view was hence 7.2 mm in width and 7.5 mm in height); the error of the temperature measurement was within ±1K (≤100 °C) or ±1% (>100 °C). Figure 3-1(b) shows the top view of the experimental apparatus. A high-speed camera (Photron fastcam mini UX50) recorded the liquid film condition and was not located in front of silicon wafer to avoid many droplets due to quenching. The high-speed camera and IR camera were synchronized with the same trigger. Frame per second of two cameras was set at 2000 fps. Table 3.3 summarized experimental condition in this experiment.

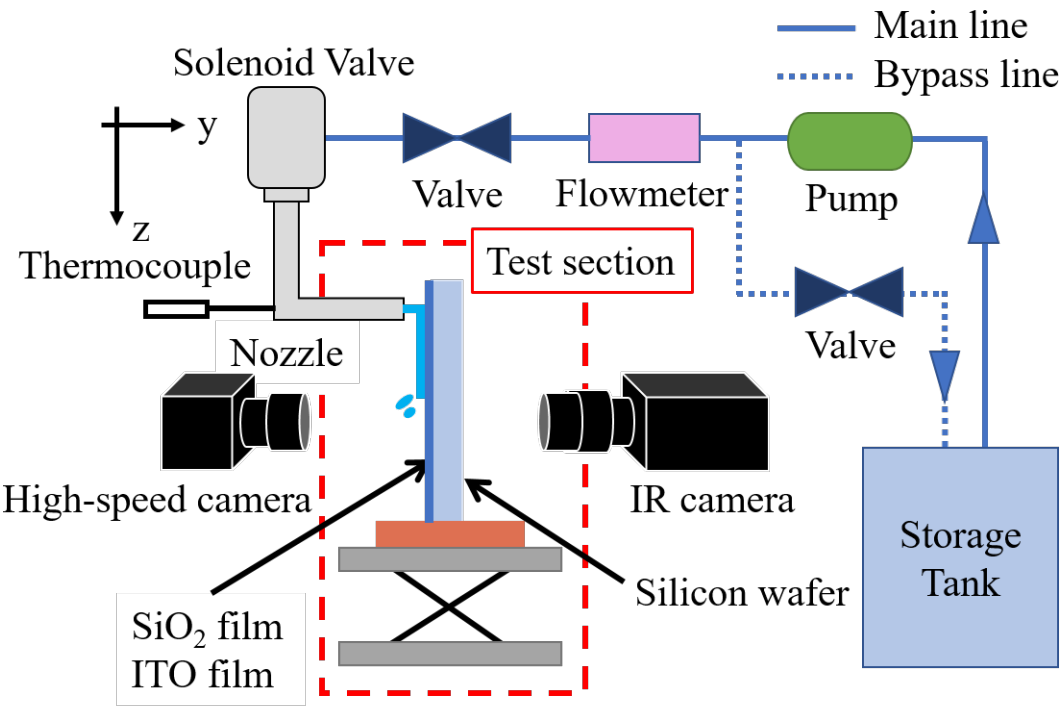

(a) Side view

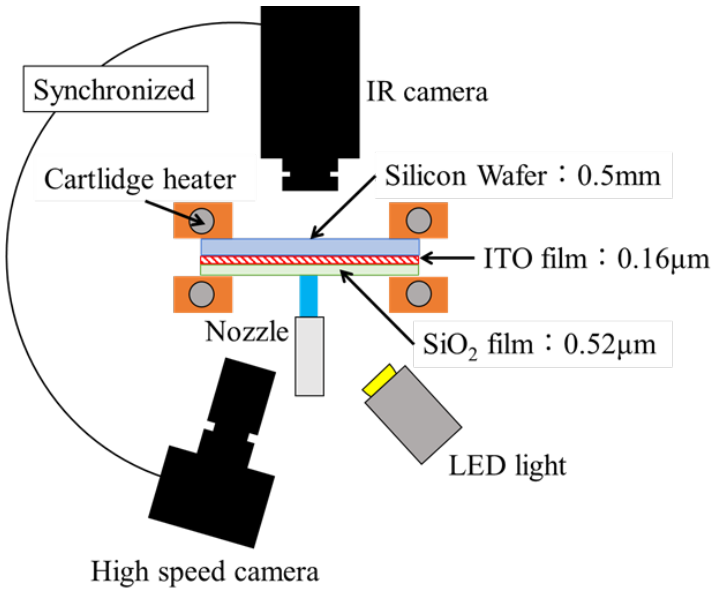

(b) Top view

Figure 3-1: Experimental apparatus

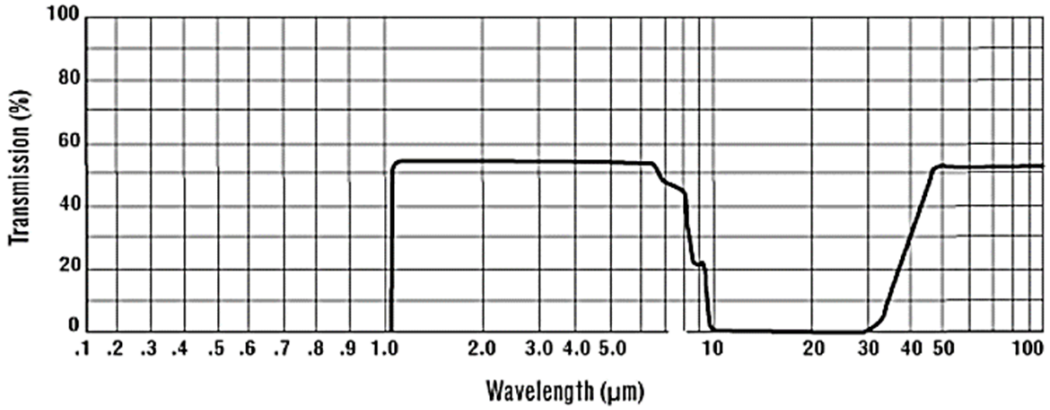

Figure 3-2: Wavelength dependence of transmittance in silicon wafers [4]

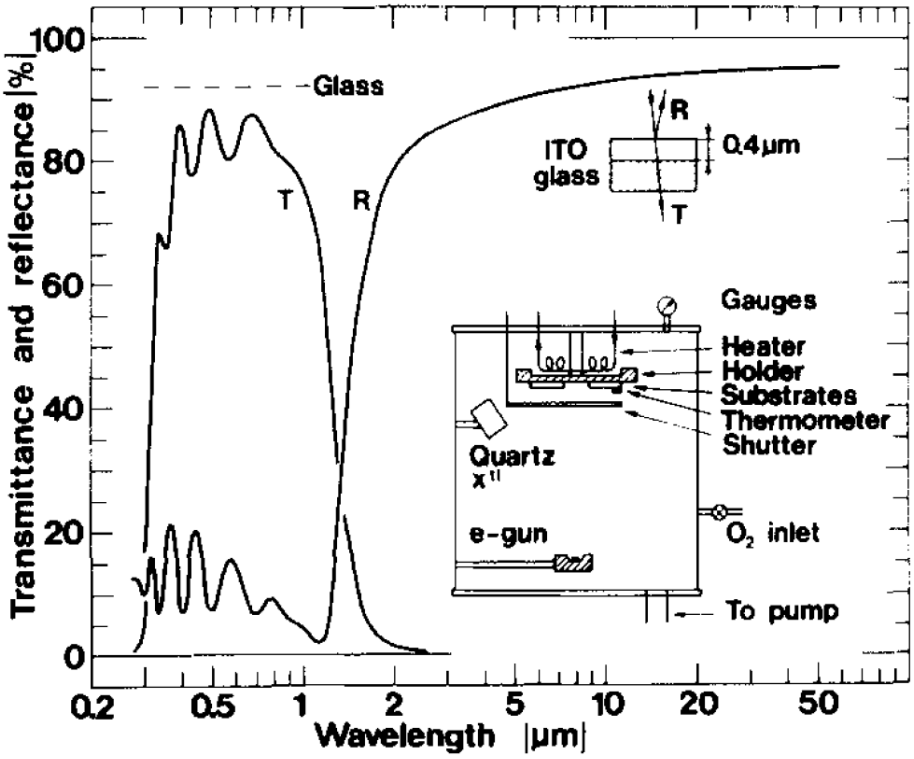

Figure 3-3: Wavelength dependence of transmittance in ITO film [5]

Table 3.1: Contact angle of silicon wafer before experiment [°]

No.	Mirror surface	Satin surface	SiO_2 film on mirror surface	SiO_2 film on satin surface
1	18.4	31.4	13.4	0
2	18.1	31	12.6	0
3	18.6	31.3	12.6	0
4	16.9	28.8	6.2	0
5	16.6	26.7	8.6	0
6	16.9	27.2	9	0
7	16.2	30.5	9.5	0
8	16.2	30.2	9.5	0
9	16.2	30.3	8.2	0
Ave.	17.1	29.7	9.9	0

Table 3.2: Contact angle of silicon wafer after experiment [°]

No.	SiO_2 film on mirror surface	SiO_2 film on satin surface
1	28.2	0
2	28.1	0
3	28.3	0
4	19.4	0
5	16.6	0
6	24.4	0
7	24.7	0
Ave.	24.6	0

Table 3.3: Experimental conditions

δ [mm]	Γ [kg/m·s]	T_{w0} [°C]
0.525	0.17-0.3	200-300

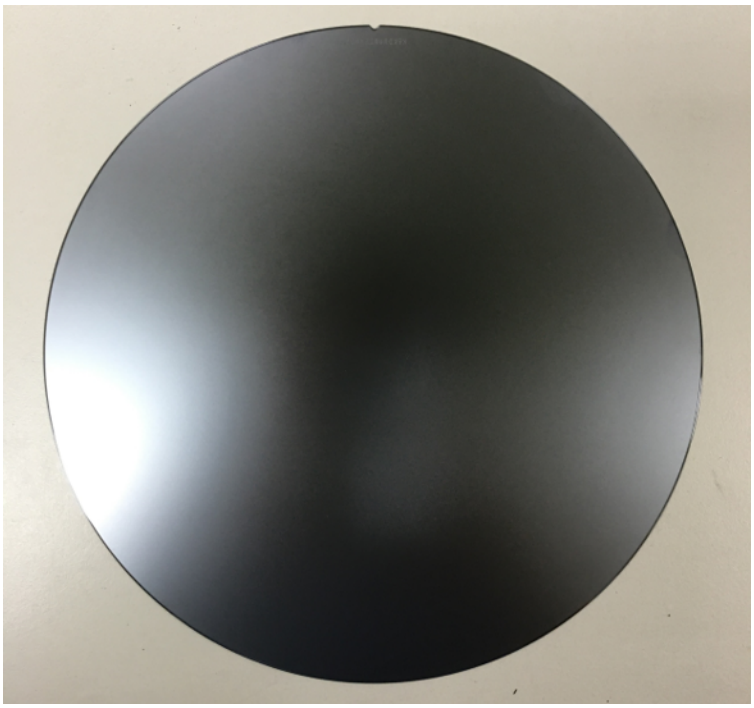

(a) Satin surface

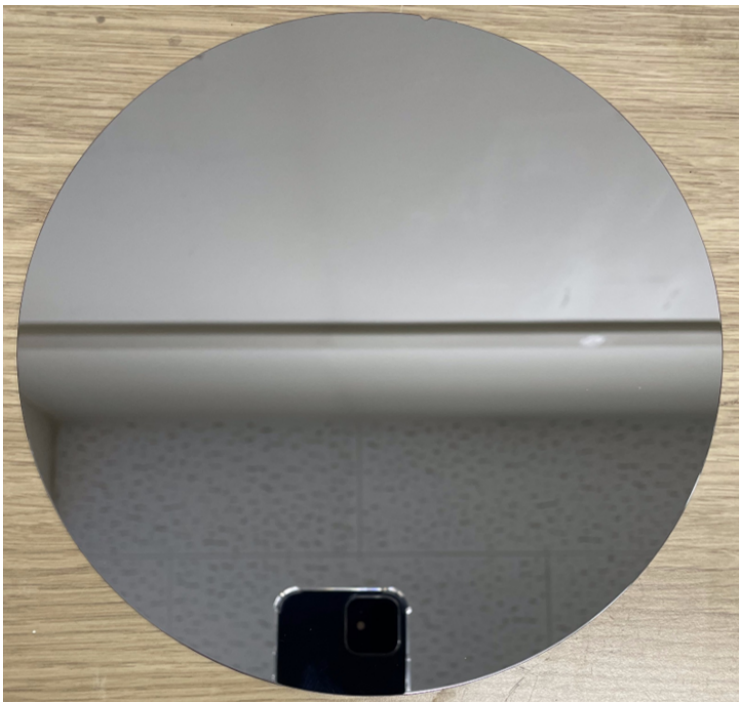

(b) Mirror surface

Figure 3-4: Silicon wafer

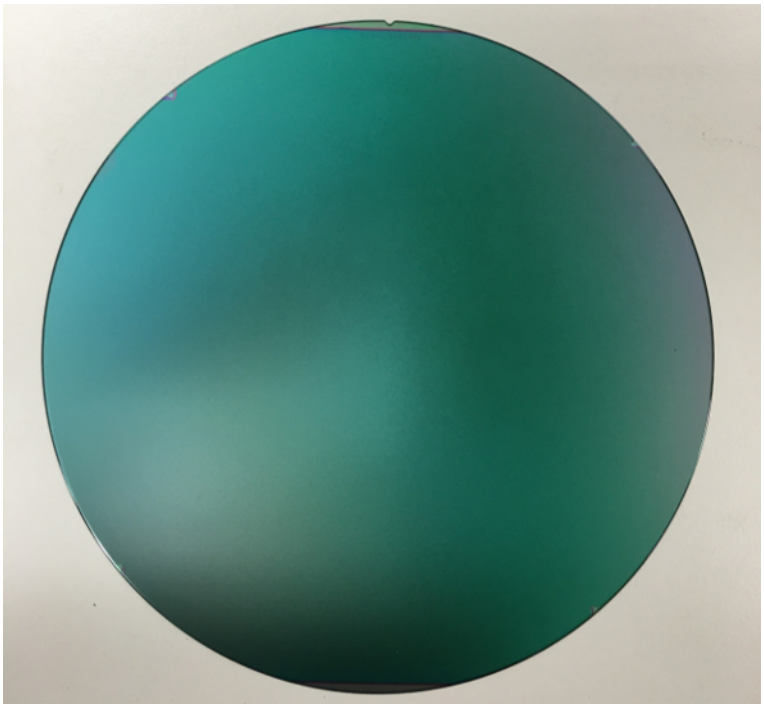

(a) Sputtered ITO and SiO_2 film on satin surface of silicon wafer

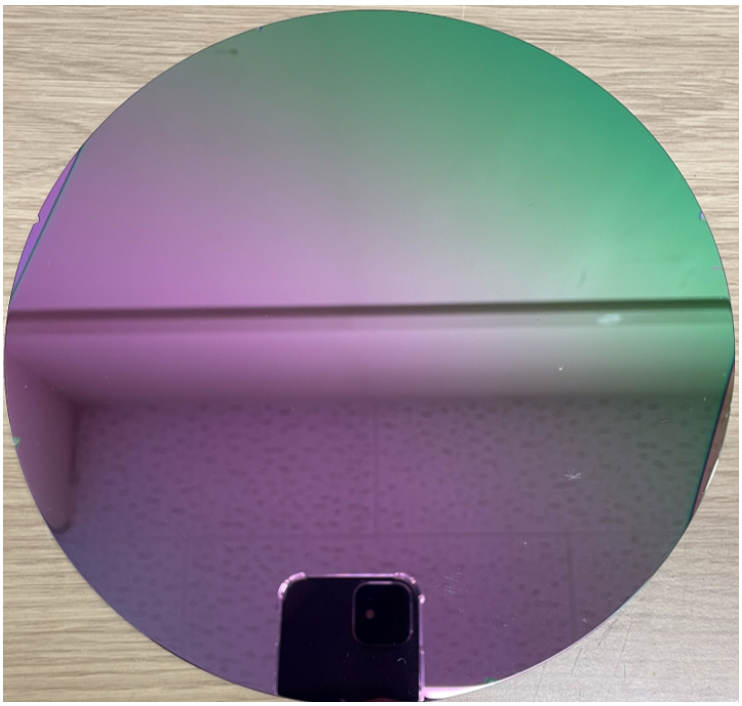

(b) Sputtered ITO and SiO_2 film on mirror surface of silicon wafer

Figure 3-5: Silicon wafer of heat transfer plate

3.2.2 Calculation method of wall heat flux distribution

Previous quenching models were expressed as the spatial distribution of HTC due to unknown temperature distribution. On the other hand, this study can know temperature distribution from experimental results. Heat flux distribution against wall temperature was calculated as the following method. First, the temperature distribution in silicon wafer in thickness was calculated by governing equation for heat transfer plate is shown in Eq. (3.1).

$$\rho c \frac{\partial T}{\partial t} = \frac{\partial}{\partial x}\left(\lambda \frac{\partial T}{\partial x}\right) + \frac{\partial}{\partial y}\left(\lambda \frac{\partial T}{\partial y}\right) + \frac{\partial}{\partial z}\left(\lambda \frac{\partial T}{\partial z}\right) \tag{3.1}$$

where ρ, c and λ is density, specific heat and thermal conductivity respectively.

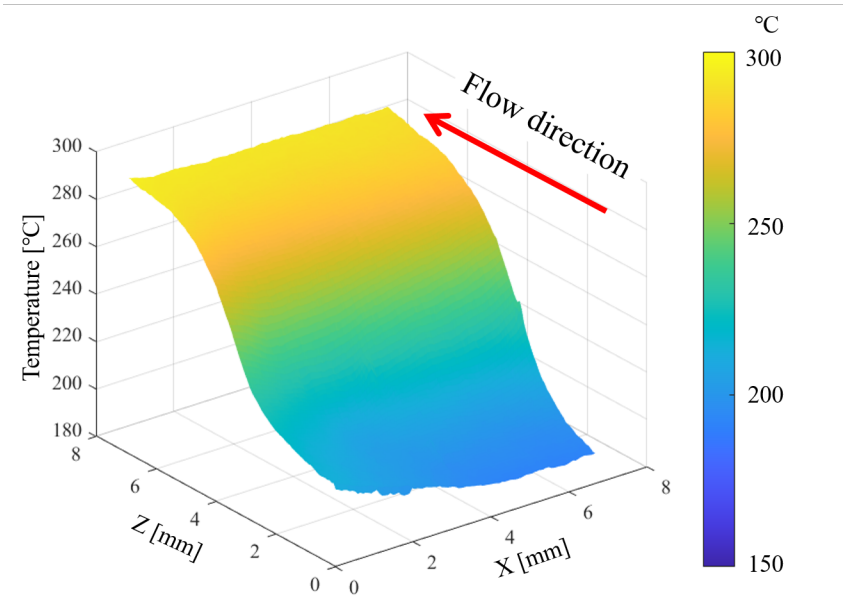

Figure 3-6: Temperature distribution during quenching

To calculate temperature distribution, partial differential terms in Eq. (3.1) were discretized based on the finite difference method. The central difference scheme was applied to the space-derivative terms, and the Euler method was used for the time derivative term. The space (Δx and Δz) was same as spatial resolutions of temperature measurement using the infra-red camera ($\Delta x = \Delta z = 75$ µm). The space in the

y-direction was set to 21 µm, where the effect of size on the calculation results is negligible. The step size in time (Δt) was determined based on von Neumann's stability criterion. The initial condition was set to the initial temperature of the experiments.

$$T_{\text{initial}} = T_{\text{w0}} \tag{3.2}$$

The boundary condition was set adiabatic in x and z direction and natural convection heat transfer coefficient (Eq. (3.3) [67]) and measured temperature (for example, Fig. 3-6) in y = δ = 0.525 mm and y = 0, respectively.

$$h_{\text{natural convection}} = 0.13\lambda_{air}\left\{\frac{g\beta_{air}(T_w - T_{air})}{\alpha\nu}\right\}^{1/3} \tag{3.3}$$

where g, β, and ν depict gravitational acceleration, thermal expansion coefficient, and kinematic viscosity. Based on the above calculation setting, repeating calculation during 0.5 ms (= 1/(2000 fps)). After that, the temperature distribution in the next time step from the experimental result was substituted to the boundary condition in y = 0.

Second, local heat flux was calculated by

$$q = -\lambda\frac{T_{(y=0)} - T_{(y=dy)}}{dy} \tag{3.4}$$

Finally, spatial average in the lateral direction (x-direction) was done in the region where the wetting front line was fairly horizontal, then, time-averaged by moving coordinate that moves by wetting velocity of the experimental results z-direction in 12.5 ms. The wetting velocity was determined from the downward displacement of the liquid film front observed in the high-speed camera image during 0.15 s. A typical example of the resulting time and spatial averaged heat flux distribution is presented in Fig. 3-7.

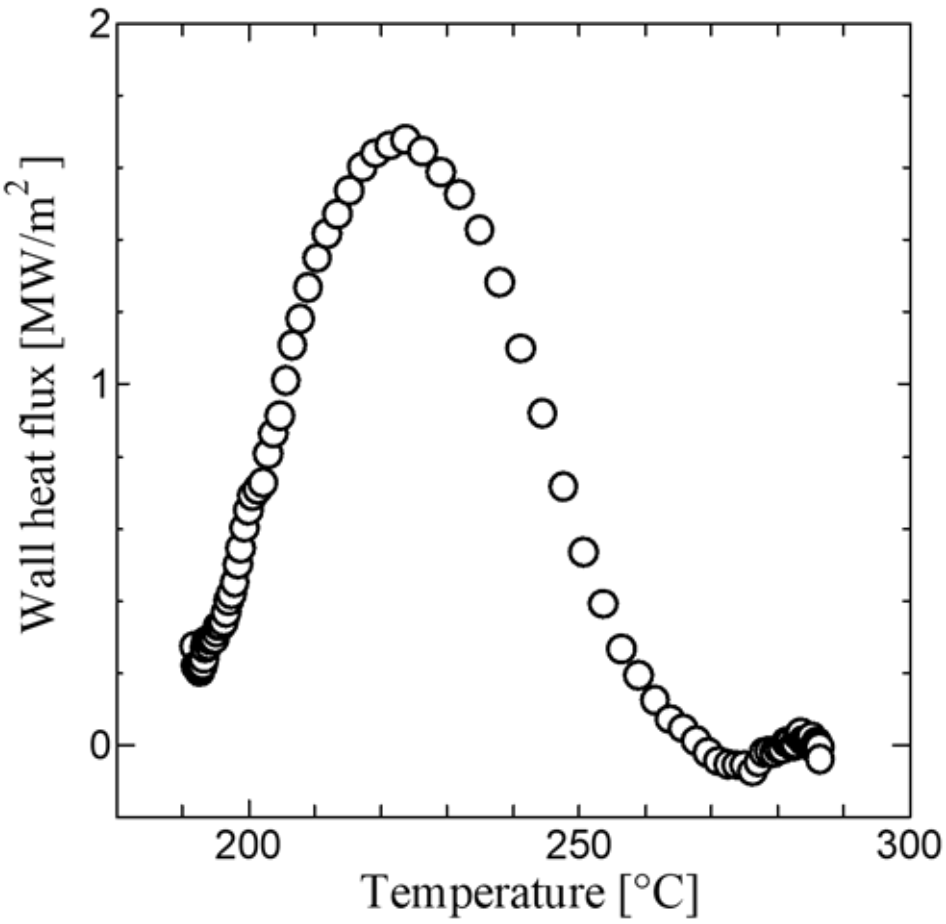

Figure 3-7: Heat flux distribution against wall temperature during quenching phenomenon

3.3 Result and discussion

3.3.1 Quenching phenomenon near the liquid film front

It is known that the quenching phenomenon shows high heat flux and occurs near the liquid film front during liquid film cooling. However, the details of the quenching phenomenon have not been observed. This section reveals the mechanism from synchronized high-speed image (liquid film condition), infrared image (temperature distribution), and calculated heat flux distribution. Fig. 3-8 shows the quenching phenomenon for 1.5 ms during liquid film cooling. The following discussion focuses on the area enclosed by the circle in Fig. 3-8. First, from comparison Fig. 3-8(a) with Fig. 3-8(b), nucleate boiling brought high heat flux. On the other hand, the place

where liquid film exists did not bring high heat flux. In fact, the heat flux of the edge of the liquid film was lower than nucleate boiling. Next time step, high heat flux area expanded like a ring as the bubble grew in Fig. 3-8(c). This phenomenon displayed the effect of thin liquid film under the bubble. Finally, the dry patch was formed after the bubble pushed back the liquid film upward in Fig. 3-8(d). The above results show that the mechanisms of high heat flux by quenching phenomenon are caused by nucleate boiling, and the dry patch is also formed by nucleate boiling. The series of quenching phenomenon was found as follows; liquid film comes to dry area (Fig. 3-8(a)), nucleate boiling occurs (Fig. 3-8(b),(c)), dry patch is formed (Fig. 3-8(d)), liquid film comes to dry area.

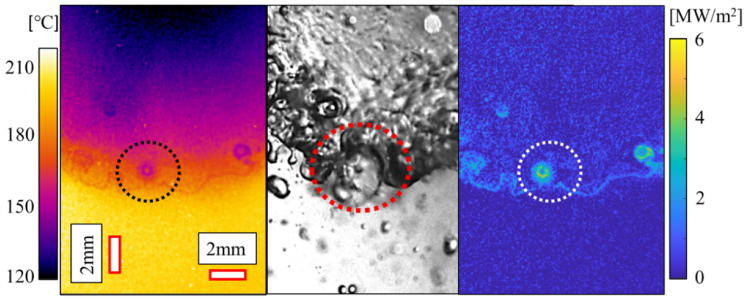

(a) t = 0 ms

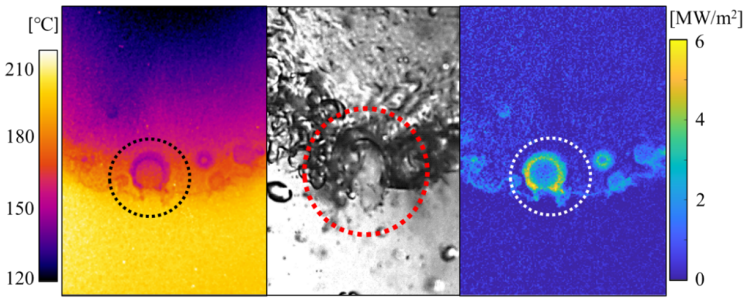

(b) t = 0.5 ms

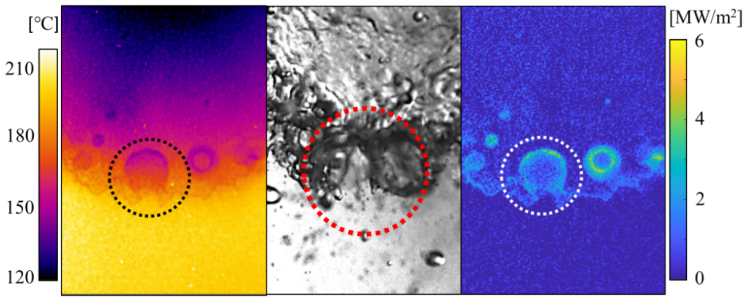

(c) t = 1.0 ms

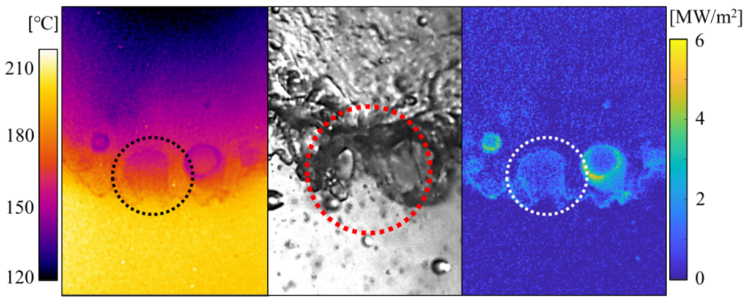

(d) t = 1.5 ms

Figure 3-8: Series of synchronized images during quenching phenomenon near liquid film front

3.3.2 Relationship between heat flux distribution and liquid film condition

Existing research defined a quenching model consisting of four critical parts: HTC peak value, quenching temperature, and HTC distribution in the dry and wet regions. It is reported that HTC distribution in the dry region is most important to estimate quenching velocity. Thus, previous research suggested various HTC distribution curves in the dry region. Yamanouchi's model [18] configured HTC in the dry region is equal to zero because there is no liquid film. Sun's model [24] implements a sputtering region between the wet region and dry region. The model applied a constant HTC value in the sputtering region. Dua's model [23], and Sahu's model [68] considered the effect of precursory cooling. So, their HTC distribution curve in the dry region was depicted as an exponentially decaying curve. This section confirms the phenomenon in the sputtering region to define new quenching model. First, in this study, the sputtering region is represented from CHF to the lower heat flux point than film boiling heat flux. Bromley [27] reported the equation of film boiling heat flux as follows.

$$q_{Bromley} = 0.943 \left\{ \frac{g\rho_{\mathrm{v}}(\rho_{\mathrm{l}} - \rho_{\mathrm{v}})\lambda_{\mathrm{v}}^{3} L_{lv}^{'}}{\mu_{\mathrm{v}} \Delta T_{\mathrm{wall}} l} \right\}^{1/4} \Delta T_{\mathrm{wall}} \tag{3.5}$$

$$\frac{L_{lv}^{'}}{L_{lv}} = 1 + \frac{c_{\mathrm{v}} \Delta T_{\mathrm{wall}}}{2 L_{lv}} \tag{3.6}$$

where $L_{lv}^{'}$ is modified latent heat, L_{lv} is latent heat.

The phenomenon in the sputtering region shows in Fig. 3-9. Blue line shows Bromley's film boiling heat flux. Red line shows the CHF. Thus, the sputtering region is the region that is sandwiched by red and blue line. It is confirmed that continuous liquid film does not exist in the sputtering region due to the nucleate boiling. On the other hand, wet region, the upstream of CHF point, has continuous liquid film, and dry region, the downward of the sputtering region, has no liquid film due to peeling off the liquid film in sputtering region.

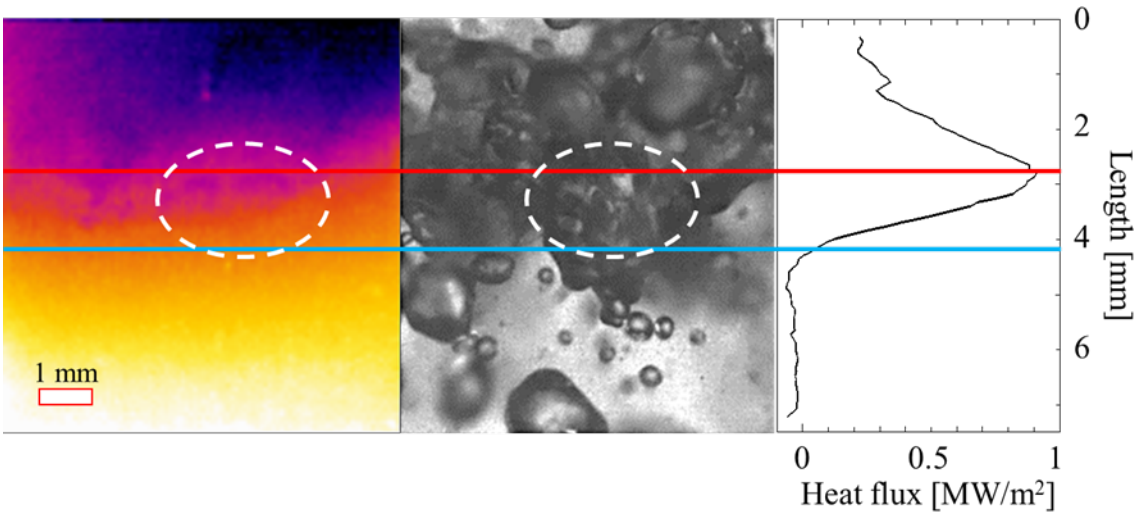

Figure 3-9: The phenomenon in sputtering region during liquid film cooling (High speed camera image, Temperature distribution, and Heat flux distribution from left)

3.3.3 The length of sputtering region

While HTC in the dry and sputtering region has a strong effect on wetting velocity, researchers defined various HTC distributions and the length for the dry and sputtering region [23, 28, 68]. Sun et al. [24] predicted the length in the dry region between incipient boiling temperature and wetting temperature analytically, 5 mm for water at atmospheric condition. Elias and Yadigaroglu [17] estimated that the length in the dry region is 1.6 mm at a low quenching velocity and 2.5 mm at high velocity from the experimental condition of Duffey and Porthouse. These prediction values were uncertain because the values were based on the quenching model that was made to match the calculated quenching velocity with the experimental one.

This study measured the length of the sputtering region from the heat flux distribution directly. The length of the sputtering region was defined between CHF and heat flux, which is below calculated heat flux from Bromley's correlation (C=0.943) [27] in Fig. 3-10. Since nucleate boiling plays an important role in heat transfer in the sputtering region, the relationship between bubble occurrence and the location of the liquid film front was confirmed. Fig 3-11 shows the inertial force of bubble occurrence advances the liquid film front. Thus, it is considered that bubble size by

nucleate boiling is related to the length of the sputtering region. The bubble size was measured from infrared camera images in Fig. 3-12. As the bubble sizes were compared with the length of the sputtering region in Fig. 3-13, the size was almost the same except for $T_{w0} = 200$ °C. Since 200 °C is a temperature low enough for the liquid film to contact the wall, the length of the dry region is bigger than bubble sizes in Fig. 3-13(a). When the initial wall temperature is high enough, the temperature does not affect the relationship between the bubble size and the length of the dry region in Fig. 3-13(a). Moreover, liquid film flow rate did not show any effect against the relationship (Fig. 3-13(b)).

In summary, the inertial force of bubble occurrence promotes the progress of the liquid film front to an uncontactable area due to high temperature. Based on the observation results, the length of the sputtering region and the bubble sizes by nucleate boiling were measured. The comparison results suggested the length of sputtering region is a constant value related to the bubble size.

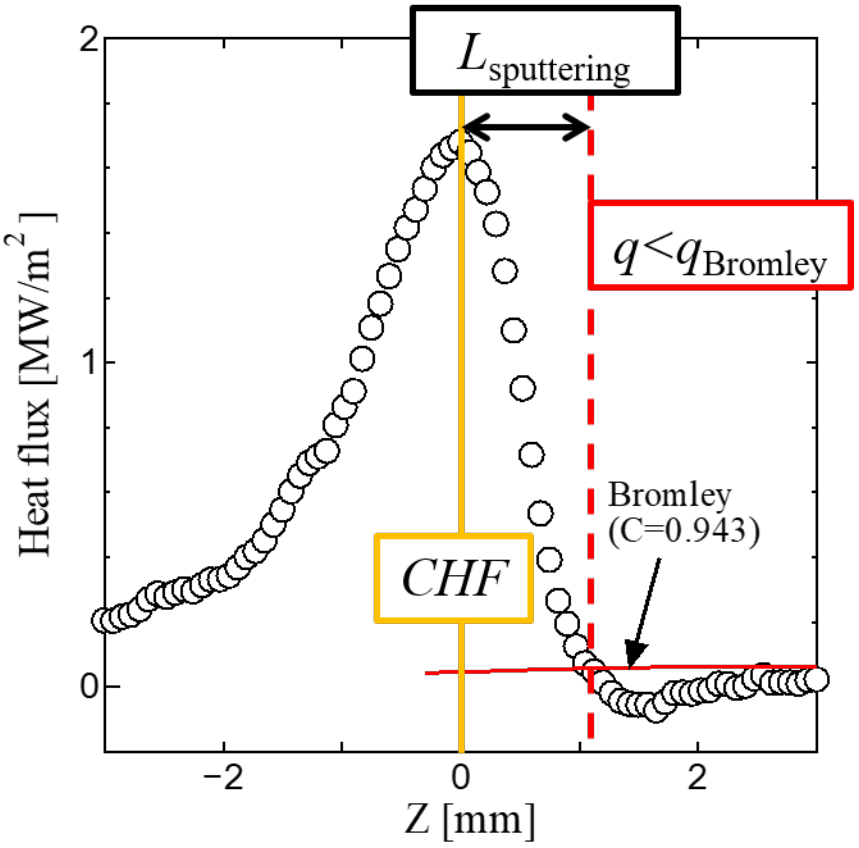

Figure 3-10: The length of sputtering region in heat flux spatial distribution (T_{w0} = 300 °C, Γ = 0.3 kg/m·s)

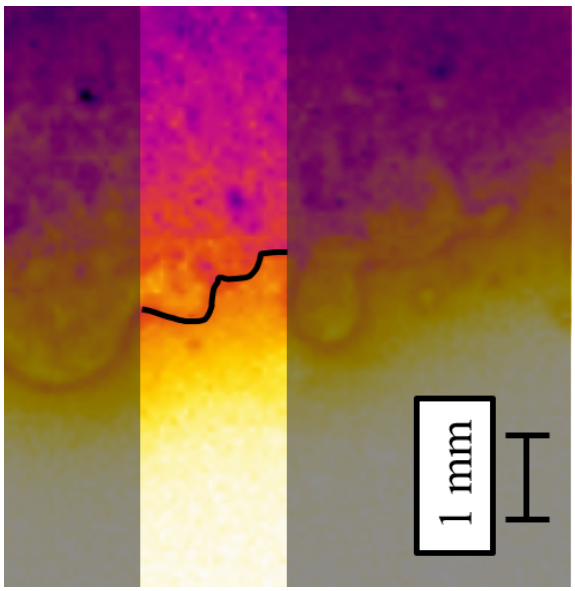

(a) t = 0 ms

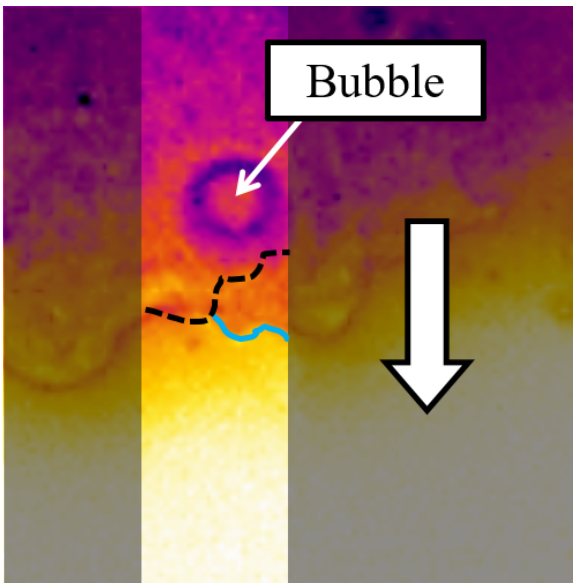

(b) t = 0.5 ms

Figure 3-11: Bubble occurrence causes the advancement of liquid film front

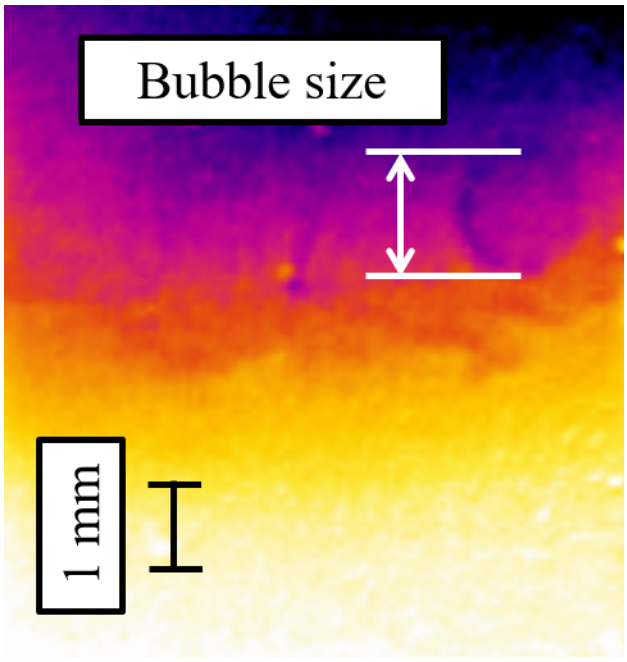

Figure 3-12: Example of bubble size near liquid film front(T_{w0} = 250 °C, Γ = 0.17 kg/m·s)

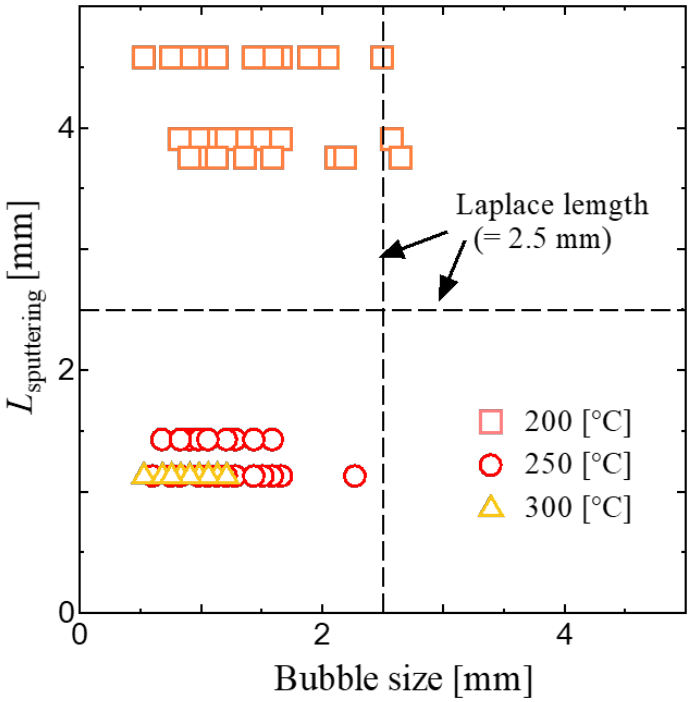

(a) Initial temperature effect (Γ = 0.3 kg/m·s)

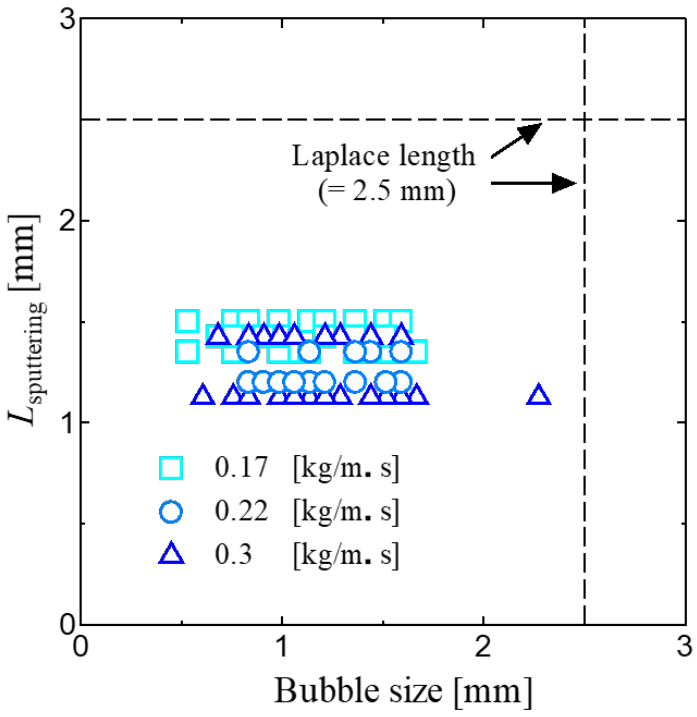

(b) Film flow rate effect (T_{w0} = 250 °C)

Figure 3-13: The length of sputtering region vs bubble size

3.3.4 Parameter effect against critical parameters

To define new quenching model, two critical parameters (CHF and T_{CHF}) should be determined from experimental results. It is noted that following correlations were made based on the experimental results without 200 °C. This is because the case of $T_{\mathrm{w0}} = 200°\mathrm{C}$ includes the effect of hydrodynamic phenomenon from the longer length of sputtering region than other cases. First, CHF correlation is determined from the experimental results. Monde et al. [69] reported that CHF is expressed as five dimensionless numbers from fluid dynamics theory as follows.

$$\frac{q_{BO}}{\rho_v \Delta h u_e} = C \left(\frac{\rho_l}{\rho_v}\right)^{n_1} \left(\frac{\mu_v}{\mu_l}\right)^{n_2} \left(\frac{\sigma}{\rho_l u_e^2 l_{heat}}\right)^{n_3} \left(\frac{\mu}{\rho_l u_e l_{heat}}\right)^{n_4} \left(\frac{g(\rho_l - \rho_v) l_{heat})}{\rho_l u_e^2}\right)^{n_5} \tag{3.7}$$

Third dimensionless number is related to surface tension (reciprocal of Weber number). Fourth dimensionless number is related to viscous force (reciprocal of Reynolds number). Firth dimensionless number is related to gravity. In pool boiling, velocity of liquid film, viscous force and the heated surface length can be neglected. Monde et al. confirmed that Eq. (3.7) can lead to pool boiling correlation (Kutateladze and Zuber equation). In present study, gravity force and viscous force can be neglected. Therefore, Eq. (3.7) can be changed as follows,

$$\frac{q_{BO}}{\rho_v \Delta h u_e} = C \left(\frac{\rho_l}{\rho_v}\right)^{n_1} \left(\frac{\sigma}{\rho_l u_e^2 l_{heat}}\right)^{n_3} \tag{3.8}$$

Based on the results of this study, two coefficients (C and n_3) is determined in Fig. 3-14 and n_2 is set 0.867 which is same as Katto et al [58].

Next, the correlation of temperature of CHF is defined from experimental results. Monde et al. [70] suggested temperature of CHF is fixed by the balance between the capacity of solid and liquid. Moreover, Tsukamoto et al. [71] proposed that quenching temperature is related to contact temperature. Contact temperature is defined from the contact of a semi-infinite object is called the contact temperature and is shown following equation.

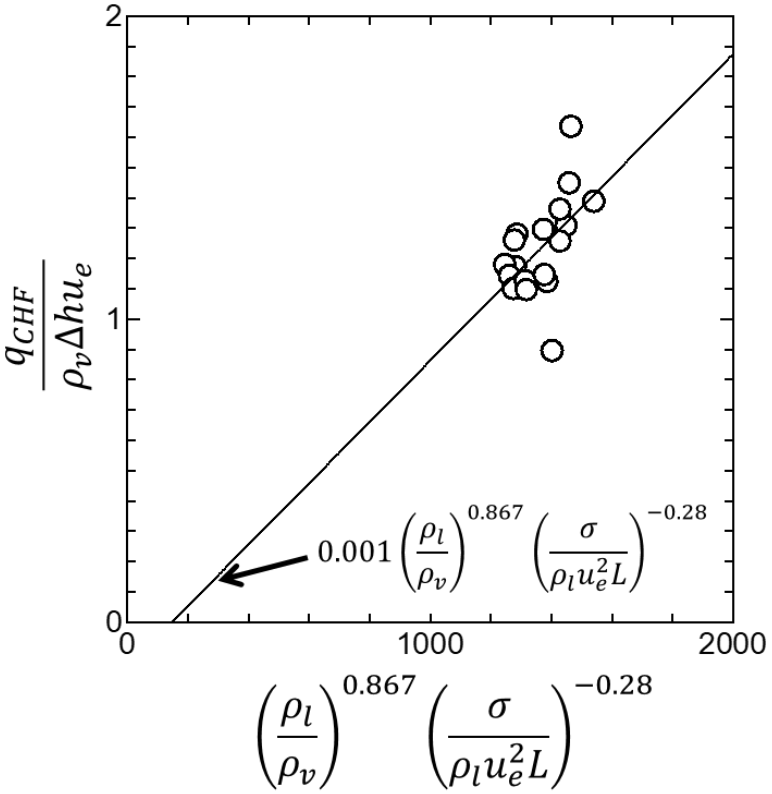

Figure 3-14: CHF correlation from Monde's dimensionless equation

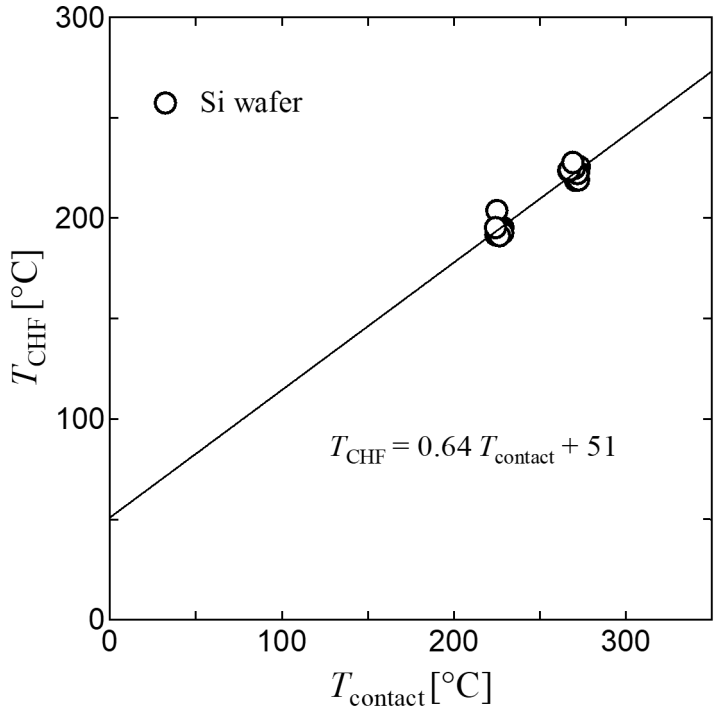

Figure 3-15: Comparison between temperature of CHF and contact temperature

$$T_{contact} = \frac{\sqrt{\rho_l c_l \lambda_l} T_l + \sqrt{\rho_w c_w \lambda_w} T_w}{\sqrt{\rho_l c_l \lambda_l} + \sqrt{\rho_w c_w \lambda_w}} \tag{3.9}$$

where, subscripts l and w is liquid and wall. Therefore, in this study, it is considered that temperature of CHF is related to contact temperature. Fig. 3-15 shows the comparison of temperature of CHF and contact temperature. From the experimental results, the correlation of temperature of CHF is defined by using contact temperature as follows.

$$T_{\mathrm{CHF}} = 0.64 \times T_{contact} + 51 \tag{3.10}$$

3.4 New quenching model

Two critical parameters (CHF and temperature of CHF) and heat flux distribution should be determined for a new quenching model. Two critical parameters were set up in the previous chapter. As HTC distribution in wet region does not have significant effect against wetting velocity, HTC distribution in wet region is set constant value ($= q_{\mathrm{CHF}}/T_{\mathrm{CHF}}$). In addition, HTC is equal to zero in the dry region due to no liquid film. According to the previous research, the value of heat transfer in the sputtering region plays a significant role in wetting velocity. Based on the experimental results, nucleate boiling dominates the heat transfer in the sputtering region, and the length of the sputtering region can be expressed by bubble size. Therefore, the length of the sputtering region is expressed by using Laplace length which is used as the bubble size in various boiling heat transfer correlations as follows.

$$L_{\mathrm{sputtering}} = 0.543 \times L_a \tag{3.11}$$

where, L_{a} is Laplace length. From Eq. (3.11), heat flux distribution in sputtering region is determined as linear function. Fig. 3-16 summarized new quenching model with an experimental result.

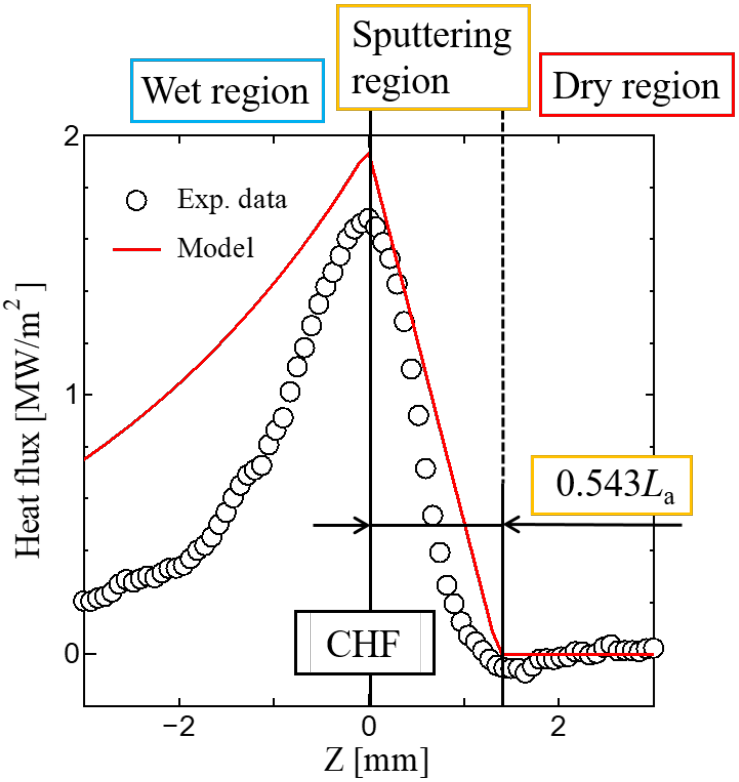

Figure 3-16: New quenching model ($T_{w0} = 300$ °C, $\Gamma = 0.28$kg/m · s)

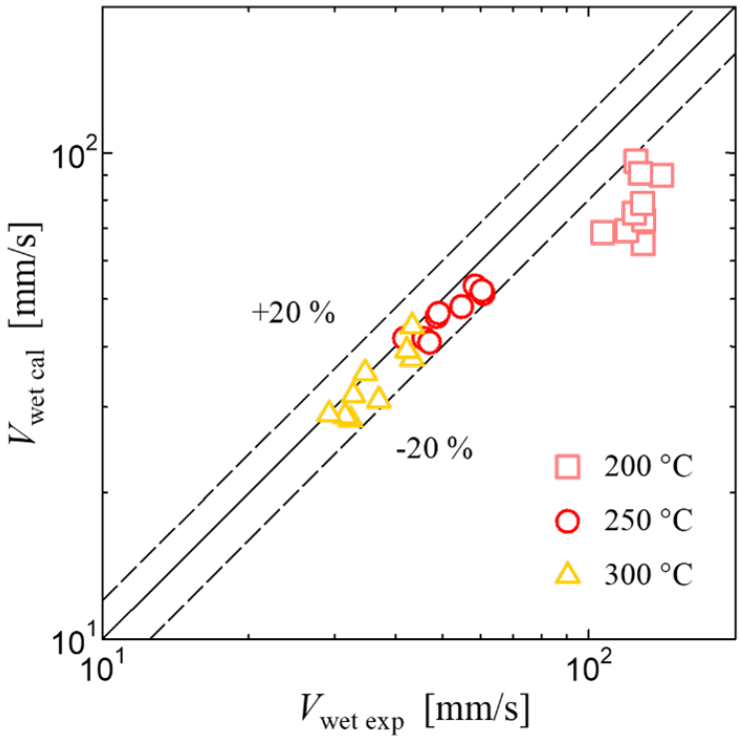

Figure 3-17: Validation for new quenching model with current experimental results of wetting velocity

3.4.1 Validation of new quenching model with current experiment results

The new quenching model is validated by comparing experimental wetting velocity and calculated one. To calculate wetting velocity, based on the finite difference method, time and spatial derivative term in Eq. (2.23) was discretized by the explicit Euler method and the central difference scheme, respectively. The boundary conditions on the surfaces in the y-direction were natural convection heat transfer (Eq. (3.3)) at y = 0 and calculated heat flux by a new quenching model at y = δ. In z-direction, the insulation condition was set. The following temperature distribution was postulated within the wall for the initial condition. The upper half in the z-direction was the coolant's saturation temperature, and the lower half was the initial wall temperature determined by experimental conditions. The time step was designated based on von Newman's stability criterion [64], and the mesh size was set to 105 μm in the y and z directions. The wall length in z-direction was set as 10.5 cm in this calculation. It was confirmed that these values are sufficient to achieve mesh size independence of the numerical solutions. Wetting velocity is calculated from the critical heat flux point's displacement in the same way as Sec. 2.4.2. Fig. 3-17 shows the comparison between the calculated and experimental ones. The new quenching model predicted experimental wetting velocity by ±20% error except for T_{w0} = 200 °C. Since low initial wall temperature is allowed the liquid-solid contact, the experimental wetting velocity includes the hydrodynamic effect. As a result, the calculated wetting velocity is slower than the experimental results in T_{w0} = 200 °C.

3.4.2 Validation of new quenching model with previous experiment results

Yu et al. [6] measured wetting velocity from falling liquid film cooling experiment. The experimental condition is summarized in Table 3.4. Under the conditions of Table 3.4, the two-dimensional heat conduction equation of cylindrical coordinates

system (Eq. (3.12)) is solved with the following boundary conditions.

$$\rho c \frac{\partial T}{\partial t} = \frac{1}{r}\frac{\partial}{\partial r}\left(\lambda r \frac{\partial T}{\partial r}\right) + \frac{\partial}{\partial z}\left(\lambda \frac{\partial T}{\partial z}\right) \tag{3.12}$$

Insulation condition is applied to the inside of the tube surface and the upper and lower end of the tube in the z-direction. The new quenching model estimates the heat transfer value on the surface of liquid film flowing. Eq. (3.12) was discretized by the explicit Euler method and the central difference scheme, respectively. The time step was designated based on von Newman's stability criterion [64], and the mesh size was set to 71 µm in the r and z directions. The tube length in z-direction was set as 10 cm in this calculation. The upper half in the z-direction was the coolant's saturation temperature, and the lower half was the initial wall temperature determined by experimental conditions. Wetting velocity is calculated from the displacement of the critical heat flux point in the same way of Sec.2.4.2. In addition, to evaluate the performance of the new quenching model, Yamanouchi [18] and Dua & Tien [23] model is also used to calculate wetting velocity. These models have known the analytical solutions by using the dimensionless number as follows.

$$Pe_{Yamanouchi} = \sqrt{\frac{Bi}{\theta_1(1+\theta_1)}} \tag{3.13}$$

$$\frac{0.01 Pe_{Dua-Tien}}{1 - 0.01 Pe_{Dua-Tien}} = \frac{0.01\left(\dfrac{Z^2-1}{2Bi}\right)\left(Y - \dfrac{A_1}{Y}\right)}{\left(\dfrac{Z^2-1}{2Bi}\right) - 0.01\left(Y - \dfrac{A_1}{Y}\right)} \tag{3.14}$$

$$Y = \frac{1}{2}\left(\frac{Bi}{Na\delta\theta_1} + \sqrt{\left(\frac{Bi}{Na\delta\theta_1}\right)^2 + \frac{4Bi}{\theta_0}}\right) \tag{3.15}$$

$$\begin{aligned} Z^3 + \left(\frac{\sqrt{2}Bi}{Na\delta} - \frac{\sqrt{2}+\theta_0}{\sqrt{2}(1-\theta_0)}\right)Z^2 + \left(\left(\frac{N-1}{N}\right)(\sqrt{2}-1)\frac{Bi}{a\delta} - 1\right)Z \\ + \left[\left(\frac{N-1}{N}\right)\frac{Bi}{a\delta} + \left(\frac{1}{1-\theta_0}\right)\left(\frac{\theta_0}{\sqrt{2}} + 1 - \frac{(2-\theta_0)Bi}{\sqrt{2}a\delta}\right)\right] = 0 \end{aligned} \tag{3.16}$$

where Pe is Peclet number, Bi is Biot number, θ_0 is dimensionless quenching temperature, θ_1 is dimensionless temperature, A_1 is dimensionless quantity ($= 3Bi/(Bi+3)$), N is constant value ($= 1 + 16/\Gamma$) and a is constant value ($= 0.05\text{cm}^{-1}$).

Figure 3-18 compared experimental wetting velocity with calculated under three different quenching models. While our model assesses experimental one in ± 30 %, the other two quenching models describe great uncertainty because it does not reflect the actual quenching phenomenon and includes experimental coefficient for a specific experiment. Therefore, our model is the most accurate quenching model under saturated water and atmosphere condition.

Table 3.4: Experimental condition by Yu et al. [6]

Wall material	Stainless steel
Shape of heated area	Tube (O.D. 15.9 mm, wall thickness δ 0.71 mm)
Coolant	Water
Initial wall temperature	200-650 °C
Coolant flow rate	20 g/s
Temperature of coolant	Saturated
Pressure	1.0 bar

3.5 Conclusions

The present study measured the transient wall temperature distribution by quenching phenomenon directly using a high-speed infrared camera and liquid film condition using a high-speed camera. Synchronized images elucidated the details of the quenching phenomenon. It was shown that nucleate boiling is the main heat transfer mechanism of falling liquid film cooling. In fact, a high heat flux was measured around the bubbles was originated by nucleate boiling. The heat transfer mechanism in the sputtering region was observed from comparing the synchronized images and heat flux distribution in the z-direction. The stable liquid film did not exist in the sputtering region, and the dry and wet conditions were repeated due to the nucleate boiling. Since nucleate boiling deeply involved the heat transfer phenomenon in the sputtering region, it was confirmed the relationship between the bubble size and the length of

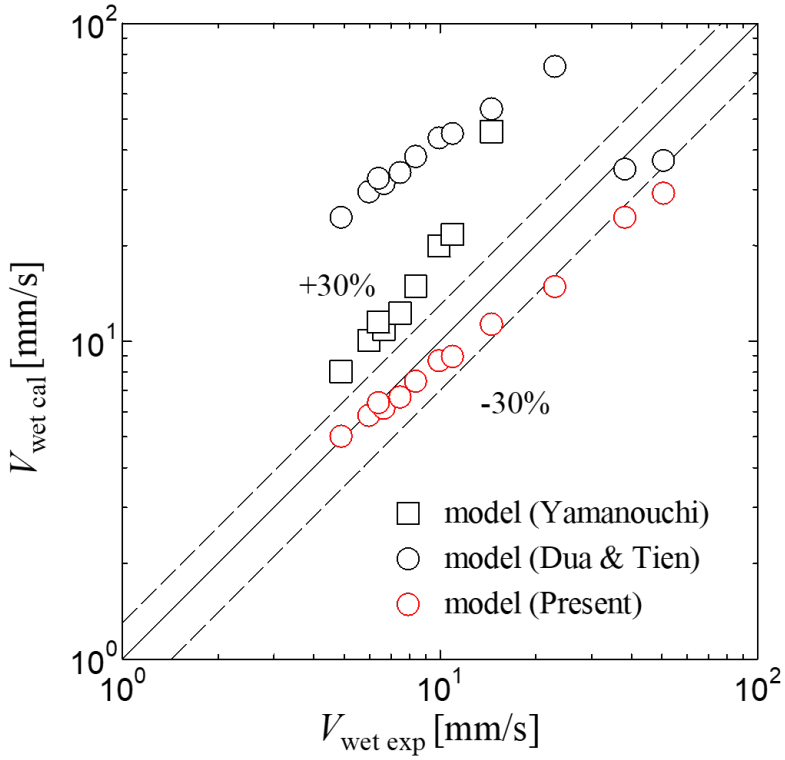

Figure 3-18: Validation for new quenching model with previous experimental results of wetting velocity

the sputtering region. As a result, the length of the sputtering region was found to be equal to the bubble sizes. The correlation of CHF and the temperature of CHF is defined from experimental results. Finally, a new quenching model is designated based on the length of the sputtering region and two correlations. Our model predicted the wetting velocity of this study in ± 20 %. Furthermore, while calculated wetting velocity by existing models shows great uncertainty against the wetting velocity of previous research, new model can estimate it in ± 30 %.

Chapter 4

The Mechanism of Nanofluid Quenching

4.1 Introduction

This chapter describes a study of the rapid cooling phenomenon in a nanofluid. Nanofluid is a liquid that contains colloidal dispersion of nanometer-sized solid particles. It is known that rapid cooling is realized when a high-temperature specimen is applied to immersion cooling in a nanofluid. However, the mechanism has not been revealed. In this chapter, the mechanism is clarified through the following process. First, a unique quenching phenomenon is observed from the quenching experiment in a nanofluid. Second, the mechanism is investigated from possible factors (surface roughness, wickability and property of nanoparticles, and so on). Third, based on the existing enhancement technique for the quenching phenomenon, the model that explains the unique quenching phenomenon in nanofluid is proposed.

4.2 Experimental descriptions

4.2.1 Nanofluid

To avoid the contamination of nanofluid, this study prepared nanofluid by oneself. Water-based nanofluids were used as the test liquids. Alumina (Al_2O_3, Aeroxide Alu C), Silica (SiO_2, Aeroxide 90G), and Titanium-dioxide (TiO_2, Aeroxide TiO_2 P25; mixture of 80% anatase and 20% rutile) were selected as the nanoparticle materials. To prepare the nanofluid, 400 mg of nanoparticles were weighed using an electronic balance accurate to within ± 0.07 mg (HR-202i, A&D Co., Ltd.). The weighed nanoparticles were then excited in 200 ml of distilled water using an ultrasonic bath (QR-003, Kaijo Co., Ltd.) at 430 kHz for 3 hours to achieve uniform dispersion (Nakamura et al. [72]). Then, distilled water was added to make the total liquid volume 1 liter. Hence, the mass concentration of the nanoparticles was calculated at 0.4 kg/m^3. Figure 4-1 depicts the appearance of the three nanofluids. The TiO_2 nanofluid was white in color while Al_2O_3 and SiO_2 nanofluids were transparent. The primary particle size reported by the manufacturer was 13 nm for Al_2O_3, 20 nm for SiO_2, and 21 nm for TiO_2, but the mean particle size in the nanofluids measured using the particle analyzer (Otsuka Electronics, FPAR-1000) was 108 nm for Al_2O_3, 234 nm for SiO_2, and 107 nm for TiO_2, suggesting that the nanoparticles formed clusters in the nanofluids. From the mass concentration and the particle size, the number density of primary particles was calculated 8.9×10^{19} m^{-3} for Al_2O_3, 3.7×10^{19} m^{-3} for SiO_2, and 1.8×10^{19} m^{-3} for TiO_2, respectively.

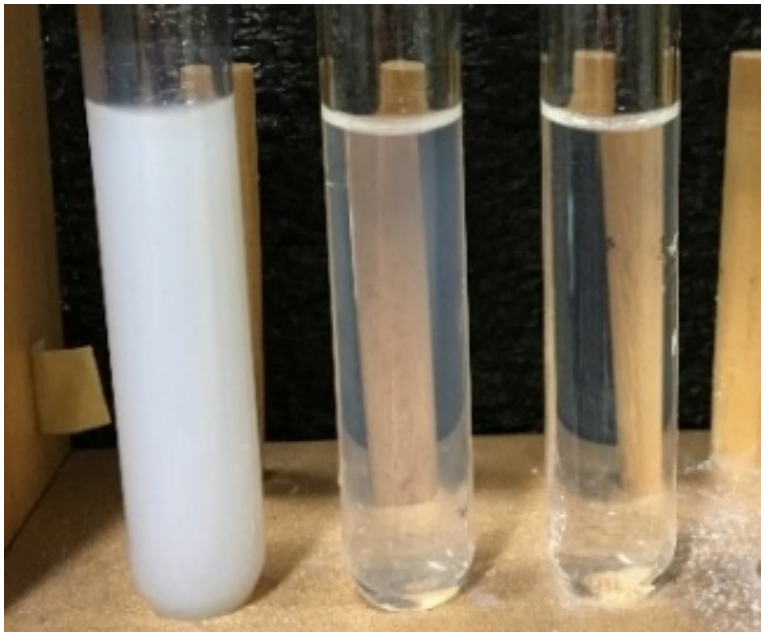

Figure 4-1: Photo of nanofluids used in the present experiments (titanium dioxide, alumina, and silica from the left side).

4.2.2 Experimental objects

Figure 4-2 shows the geometries of the Inconel 718 and SUS304 rodlets used as the specimens in this work. Inconel 718 rodlet was 16 mm in diameter and 30 mm in length and the SUS304 rodlet was 15 mm in diameter and 30 mm in length. Important properties of Inconel 718 and SUS304 are presented in Table 4.1. To measure the temperature transient during quenching, two type-K thermocouples (1.6 mm in outer diameter and 0.5s in time constant) were placed in the rodlets as delineated in Fig. 4-2. One was placed at the center as the typical position to understand the temperature transient qualitatively and the other was placed near the wall to reduce the error in the inverse analysis. The measurement uncertainty of the thermocouples was 2.5 K for the temperature range of T $<$ 333°C and 0.75% for T $>$ 333°C. After inserting the thermocouple into the hole, the area surrounding the hole was hit with a sharp-tip tool to fix the thermocouple in the hole. Before the experiment, the rodlet surface was polished using metal polishing paste and then cleaned using acetone and distilled water.

Table 4.1: Properties of test piece materials [7] [8]

	Density ρ [kg/m^3]	Thermal conductivity λ [W/m · K]	Specific heat c [J/kg · K]	Thermal diffusivity α [mm^2/s]
Inconel718				
25°C	8190	8.9	435	2.5
1000°C	7806	26.7	620	5.52
Ave.	7998	17.8	527.5	4.22
SUS304				
25°C	7920	16	490	4.12
1000°C	7500	28	630	5.9
Ave.	7710	22	560	5.1

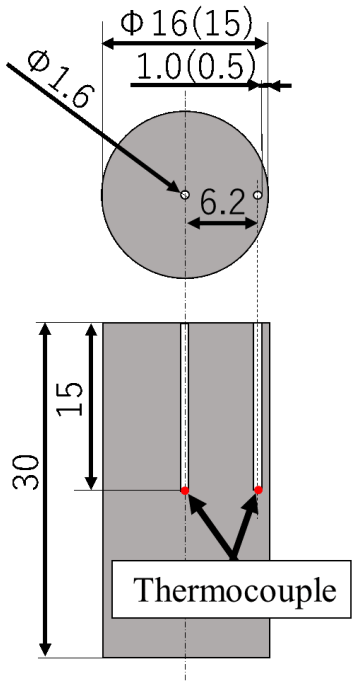

Figure 4-2: Geometries of the Inconel 718 specimen (values in parentheses are for the SUS304 specimen) [unit: mm]

4.2.3 Experimental apparatus and procedure

The experiment set up is shown schematically in Fig. 4-3. The experimental steps are described as follows.

1. A glass cylindrical beaker (133 mm in diameter and 185 mm in height) containing 1 liter of test liquid was put on a hot plate to heat the liquid to 80±1 °C.

2. The rodlet was heated to 1000±2 °C in an electronic furnace.

3. The rodlet was immersed in the test liquid to cool the rodlet to the liquid temperature. The process of phase change around the rodlet was recorded using a high-speed camera (FASTCAM mini UX50, Photron Co., Ltd.). The initial temperature difference between the center and periphery thermocouples was within 1K. The rodlet was held vertically in the pool manually; the inclination of the rodlet from the vertical was estimated within 3°.

4. The experimental steps 2 and 3 were repeated five times.

The temperature data measured using the thermocouples were recorded every 0.1s during the experiment. In the observation using the high-speed camera, the spatial resolution was set to 100 µm/pixel, the frame rate was 500 frames/s, and the shutter speed was 200 µs.

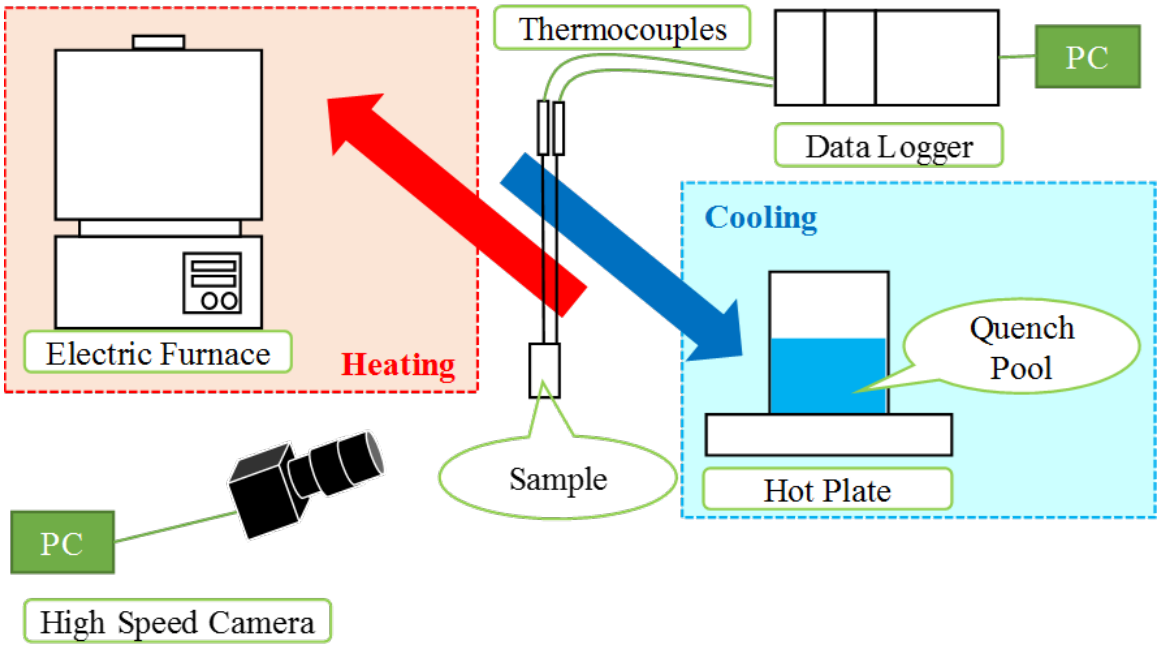

Figure 4-3: Experimental apparatus and procedure

4.2.4 Calculation methods of wall superheat and wall heat flux

An inverse heat conduction problem was solved to deduce the time variations of the wall superheat and the wall heat flux during quenching. The governing equation was the following one-dimensional heat conduction equation in cylindrical coordinates.

$$\frac{1}{\alpha}\frac{\partial T}{\partial t} = \frac{1}{r}\frac{\partial}{\partial r}\left(r\frac{\partial T}{\partial r}\right) \tag{4.1}$$

where t is the time, r is the spatial coordinate in the radial direction, T is the temperature, and α is the thermal diffusivity of the rodlet. The thermal properties of the test piece materials were assumed constant at the average values in Table 4.1 in the calculation. The difference of the calculated minimum heat flux temperature was within 5 K even when the properties at 25 and 1000 °C were used. The above equation was solved using the Laplace transformation technique (Monde et al. [73,74] Woodfield et al. [75,76]). The initial and boundary conditions are expressed by

$$T|_{t=0} = T_0 \tag{4.2}$$

$$T|_{r=r_1} = T_1(t) = T_0 + \sum_{k=0}^{N_k} \frac{P_{k,1}t^{(k/2)}}{\Gamma((k/2)+1)} \tag{4.3}$$

$$T|_{r=r_2} = T_2(t) = T_0 + \sum_{k=0}^{N_k} \frac{P_{k,2}t^{(k/2)}}{\Gamma((k/2)+1)} \tag{4.4}$$

where T_0 is the initial rodlet temperature, r_1 and r_2 are the thermocouple positions in the radial direction, Γ is the gamma function, and N_k is the number of terms of polynomial approximation. The value of N_k was set to 5 and the values of the coefficients $P_{k,1}$ and $P_{k,2}$ were determined by approximating the temperature histories measured at the two thermocouple positions using the least squares method [75]. The uncertainties in the calculated boiling curves were estimated from the uncertainties of the measured temperature values and radial positions of the thermocouples ($\pm$ 0.4 mm) by changing these values in the inverse analysis. As a result, the uncertainties due to temperature value were estimated less than $\pm$ 8 K for the wall superheat

and ± 0.6% for the wall heat flux. Those due to the thermocouple position were estimated less than ± 10 K for the wall superheat and ± 20% for the wall heat flux. Adding these values, the uncertainties in the calculated boiling curves were estimated less than ± 18 K for the wall superheat and 21% for the wall heat flux. Another important factor that induces uncertainty in the calculated boiling curves is the elimination of multidimensional effect in the inverse analysis. As discussed later, quenching first occurred at the bottom of the rodlet in distilled water and in the first run in nanofluid. In consequence, heat transfer in the vertical direction might have a noticeable influence on the calculated boiling curves in these cases. Therefore, in the following sections, only qualitative discussion is possible when comparing the boiling curves for these cases with those for the other cases.

4.3 Result and discussion

4.3.1 Qualitative descriptions of the results of quenching experiment

Figure 4-4 shows the experimental results for the Inconel 718 rodlet immersed in the distilled water. Figure 4-4(a) presents the temperature transients measured at the center (r = 0 mm) and the periphery (r = 6.2 mm) of the rodlet, and Fig. 4-4(b) the boiling curves calculated by the inverse analysis; here, ΔT_{wall} in Fig. 4-4(b) refers the wall superheat. It is noted that the boiling curves for $\Delta T_{\text{wall}} < 800$ K are shown in Fig. 4-4(b) since the accurate calculation is not possible immediately after immersion of the rodlet. The boiling curves are compared with the following correlations for nucleate boiling heat transfer Eq. (4.5) by Rohsenow [25] ($C_{sf} = 0.014$), critical heat flux Eq. (4.7) by Zuber [77], minimum heat flux point Eq. (4.8) by Dhir and Purohit [78], and film boiling heat transfer Eq. (4.9) by Bromley [27].

$$h_{nucleate} = \frac{\lambda_l}{L_a} \frac{Pr^{-0.7}}{C_{sf}} \left(\frac{qL_a}{\rho_v v_l \Delta h} \right)^{0.67} \left(\frac{\rho_v}{\rho_l} \right)^{0.67} \tag{4.5}$$

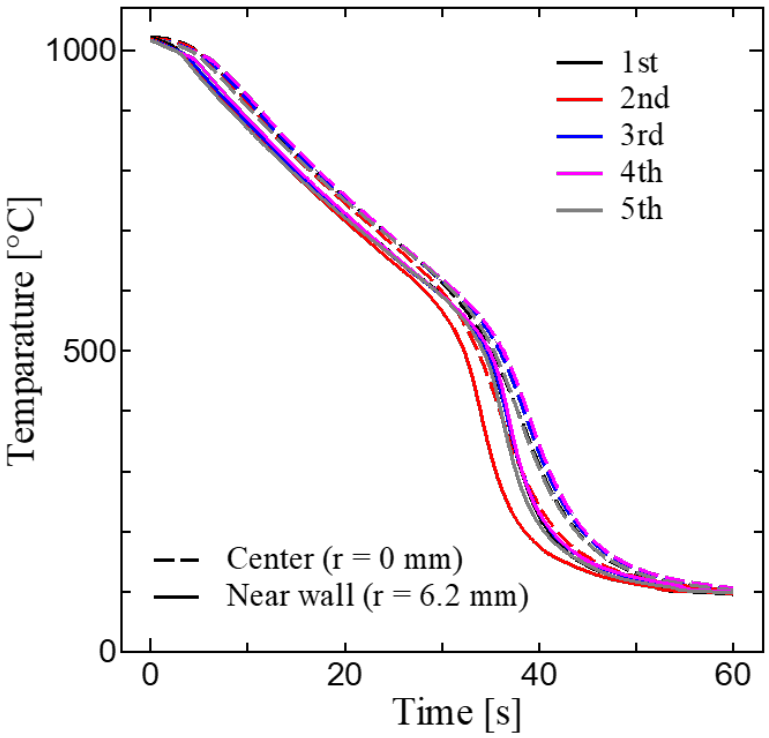

(a) Cooling curves

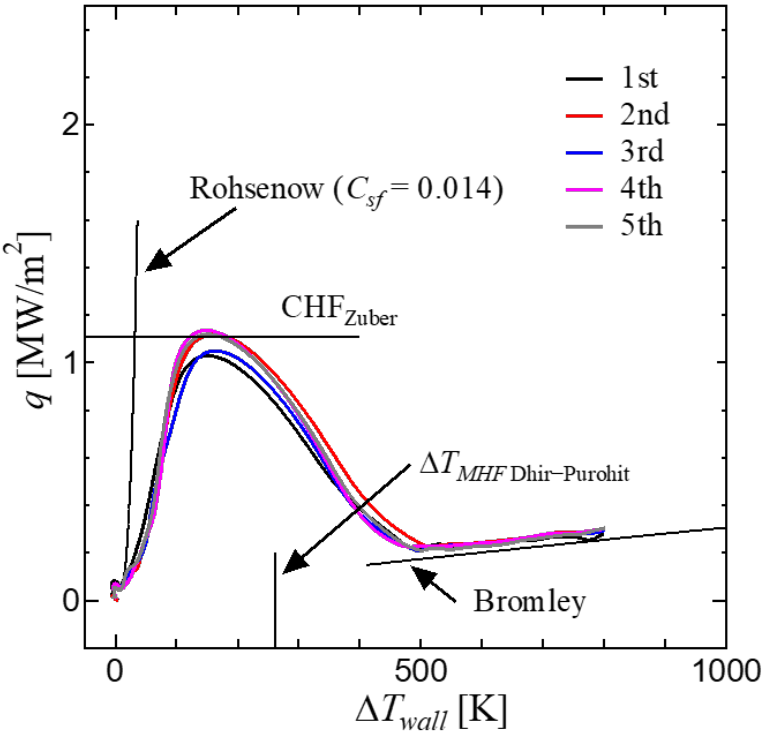

(b) Boiling curves

Figure 4-4: Quenching characteristics of high-temperature test piece in distilled water

$$L_a = \sqrt{\frac{\sigma}{g(\rho_l - \rho_v)}} \tag{4.6}$$

$$q_{\mathrm{CHF}} = 0.131\rho_v \Delta h \left\{ \frac{\sigma g(\rho_l - \rho_v)}{\rho_v^2} \right\}^{1/4} \tag{4.7}$$

$$\Delta T_{\mathrm{MHF}} = 101 + 8\Delta T_{sub} \tag{4.8}$$

$$h_{film} = 0.943 \left\{ \frac{g\rho_v(\rho_l - \rho_v)\lambda_v^3(\Delta h + \frac{c_v \Delta T_{\mathrm{wall}}}{2})}{\mu_v \Delta T_{sat} l} \right\}^{1/4} \tag{4.9}$$

where the subscripts l and v denote liquid and vapor phases, respectively, q is the heat flux, L_a is the Laplace length, Pr is Prandtl number, C_{sf} is an empirical constant determined by the combination of liquid and heat transfer surface, v is kinematic viscosity, ΔT_{wall} is subcooling, μ is viscosity, l is the height of the thermocouple position from the bottom of test piece, σ is the surface tension, and g is the gravitational acceleration. The film boiling heat transfer coefficient and CHF agree with Bromley's and Zuber's correlations fairly well, respectively. However, noticeable discrepancy with the previous correlations is seen for the experimental values of ΔT_{MHF} and nucleate boiling heat transfer coefficient. These would be attributed to the one-dimensional approximation adopted in the inverse analysis. Four snapshots during quenching are displayed in Figs. 4-5(a) - (d). In Fig. 4-5(e), the blue curve denotes the wall temperature history and the gray line shows the heat flux history in the second run calculated by the inverse analysis. As shown in Fig. 5(a), the rodlet was first covered by the vapor film. The vapor film then disappeared gradually from the bottom of the rodlet (Figs. 4-5(b) - (d)). The lower edge of the vapor film reached the center of the rodlet at about 30s (Fig. 4-5(c)). At this moment, the cooling rate is nearly highest value as can be seen in Fig. 4-5(e). The maximum heat flux was measured when the vapor film disappeared at the thermocouple elevation (Figs. 4-5(d) and (e)). Figures 4-4(a) and 4-4(b) also indicate that the temperature transient did not change noticeably even if the quenching experiment was repeated.

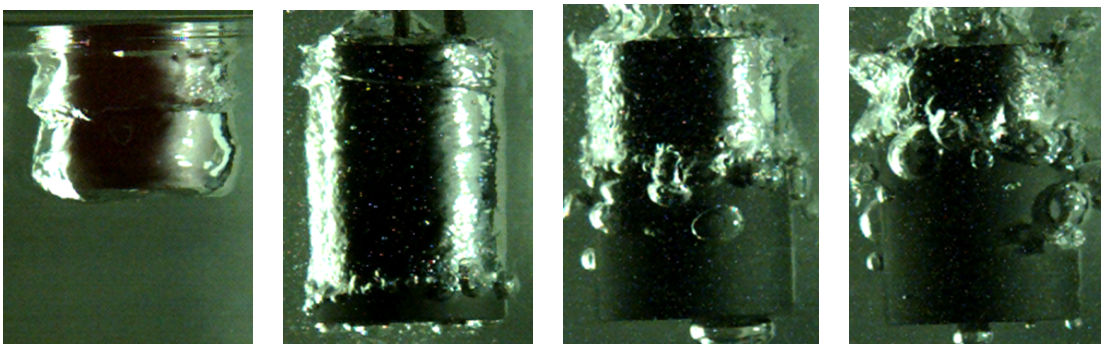

(a) t = 0s (b) t = 23.8s (MHF) (c) t = 31.1s (Transition) (d) t = 32.6s (CHF)

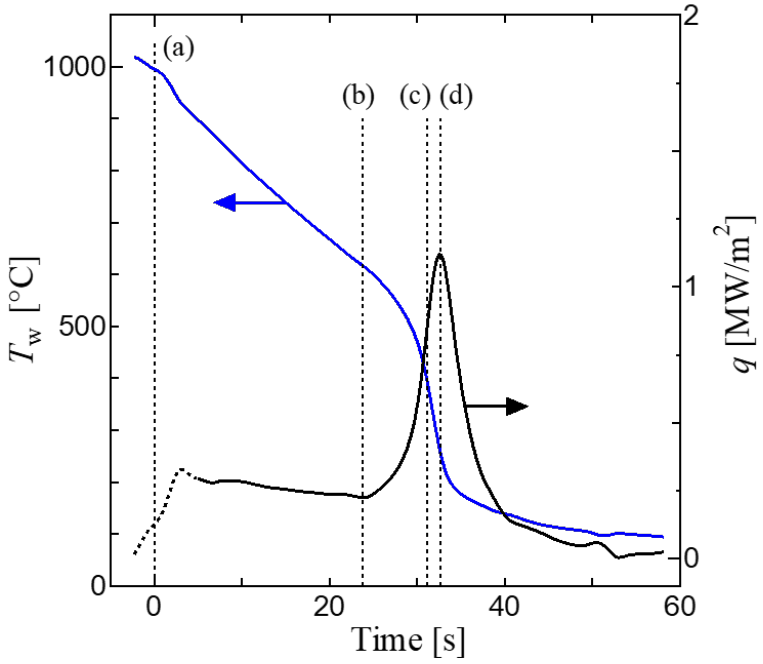

(e) Wall temperature and heat flux history

Figure 4-5: Boiling phenomenon during quenching of high-temperature rodlet in distilled water (second run)

The results of temperature measurement and visualization for the Inconel 718 rodlet immersed in the silica nanofluid are presented in Figs. 4-6 and 4-7, respectively. Figures 4-6(a) and 4-6(b) indicate that the cooling characteristics in the first run were similar to those in the distilled water, but the cooling performance was improved asymptotically in the subsequent runs. In particular, the wall superheat at the minimum heat flux point ΔT_{MHF} ($= T_{\mathrm{MHF}} - T_{sat}$) where the cooling acceleration starts is about 600 K in the first run and rose drastically to 800-900 K in the subsequent runs (the calculation method of ΔT_{MHF} is described in the appendix B). It is also interesting to note that in Fig. 4-6(b), two clear peaks are seen in the boiling curves in the subsequent runs. The visualization results in the second run are depicted in Fig. 4-7(a) - (f) and the calculated transients of the wall temperature and heat flux are presented in Fig. 4-7(g). Figures 4-7(a) and (b) indicate that the whole surface of the rodlet was first covered by the vapor film as in distilled water but then covered by many small bubbles (Figs. 4-7(c) and 4-7(d)). This distinct boiling mode causes the first peak in the right of the boiling curve and the drastic increase of ΔT_{MHF}. The lower edge of the vapor film then moved upward (Figs. 4-7(e) and 4-7(f)) as observed in the distilled water. The second peak in the left of the boiling curve in 4-6(b) can hence be attributed to the collapse of the vapor film as in the case of distilled water.

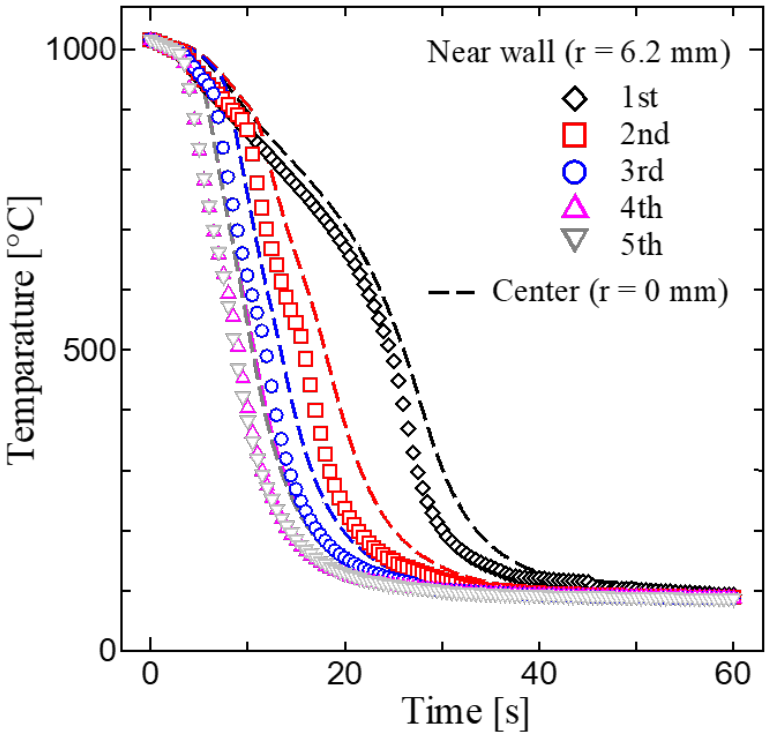

(a) Cooling curves

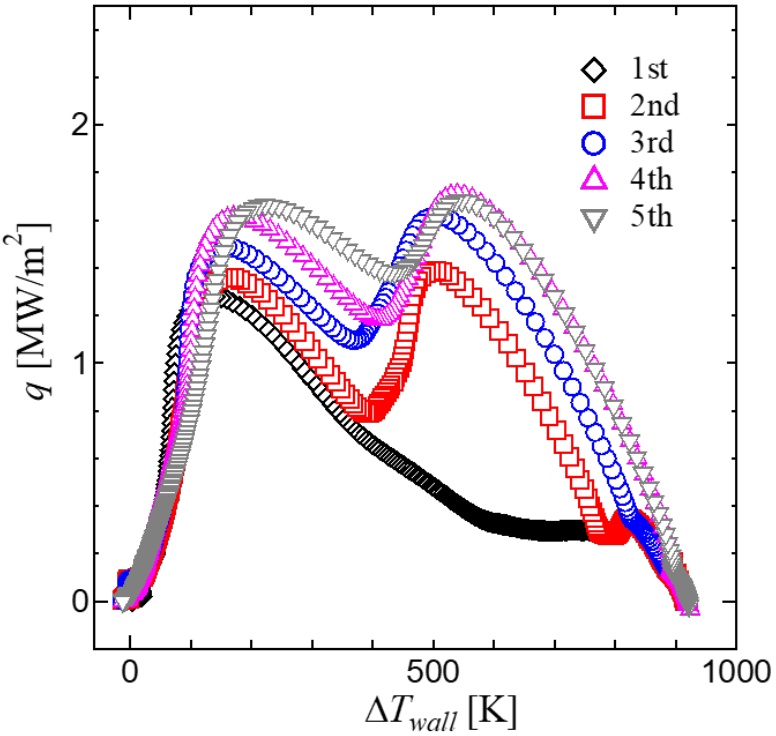

(b) Boiling curves

Figure 4-6: Quenching characteristics of high-temperature test piece in silica nanofluid ($0.4 \mathrm{kg}/m^3$)

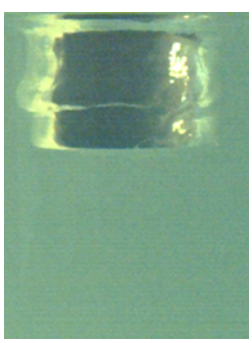

(a) t = 0 s

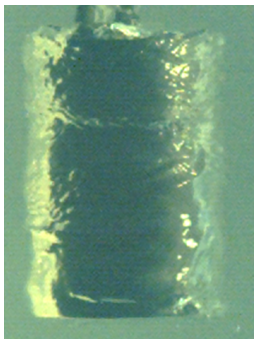

(b) t = 6.3 s (1st MHF*)

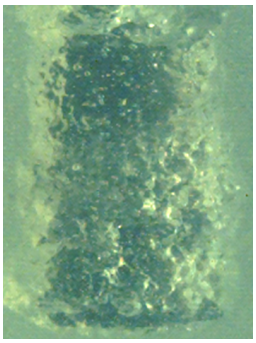

(c) t = 8.3 s (Transition)

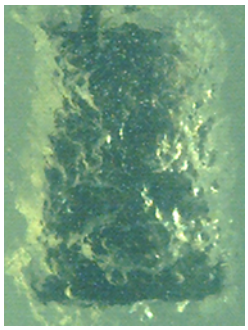

(d) t = 9.5 s (1st heat flux peak)

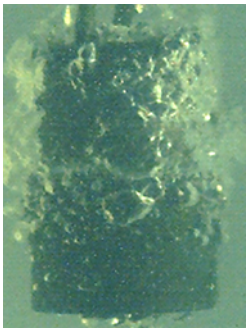

(e) t = 12.6 s (2nd MHF*)

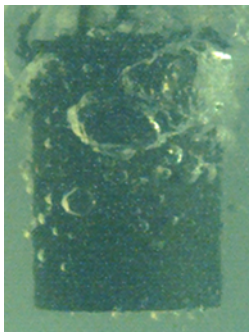

(f) t = 15.1 s (2nd heat flux peak (=CHF))

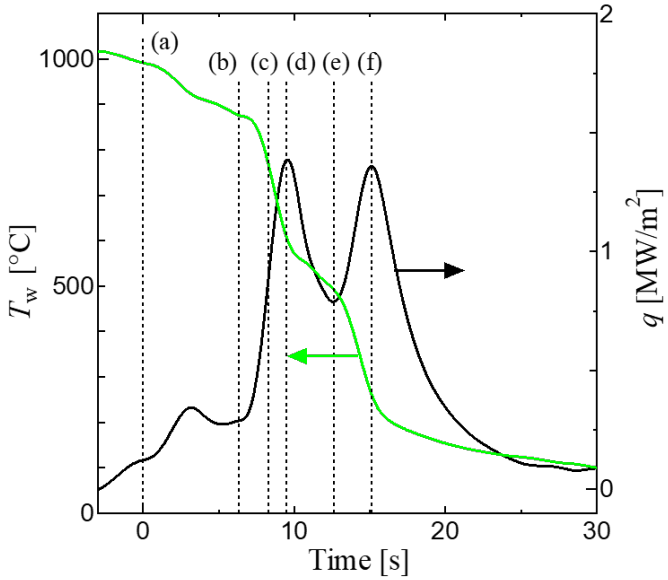

(g) Wall temperature and heat flux history

Figure 4-7: Boiling phenomenon during quenching of high-temperature rodlet in silica nanofluid (second run). (*)1st MHF indicates the ordinary MHF corresponding to boiling transition from film boiling to transition boiling.

The cooling curves measured for the Inconel 718 rodlet immersed in Al_2O_3 and TiO_2 nanofluids are presented in Figs. 4-8(a) and (b), respectively. The cooling time became shorter with repeating the experimental run gradually as in the case of SiO2 nanofluid. Figures 4-8(c) and 4-8(d) show the calculated boiling curves. The boiling curves for the Al_2O_3 nanofluid are similar to those for the SiO_2 nanofluid. However, in the TiO_2 nanofluid, reduction of ΔT_{MHF} was less significant and the boiling curves are similar to those for the distilled water. The photos of specimen taken after the fifth run are presented in Fig. 4-9. The rodlet surface was kept clean even after the experiments for the distilled water (Fig. 4-9(a)), while the nanoparticle layer was formed in the experiments using the nanofluids (Figs. 4-9(b) - (d)). The acceleration of cooling might hence be attributed to the modification of the surface properties caused by the nanoparticle deposition. Since the deposition of nanoparticles occurs during nucleate boiling (Saeid and Borca-Tasciuc [79]; Kwark et al. [3]), it is considered that even in the experiments in nanofluid, the nanoparticle layer was not present on the surface until the wall superheat decreased sufficiently in the first run. This is consistent with the fact that no significant improvement of the cooling rate was observed in the first run in Figs. 4-6 and 4-8. It is noted that the nanoparticle layer was yellow in color in Fig. 4-9(d). This would indicate that chemical reaction of titanium-dioxide with Inconel 718 occurred during quenching to produce titanium-yellow in the TiO_2 nanofluid.

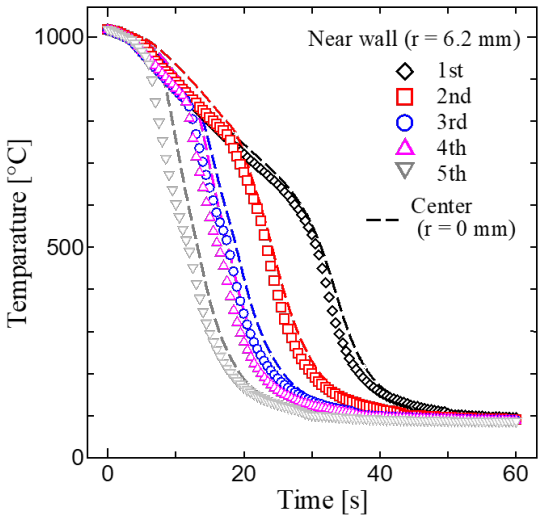

(a) Cooling curves in alumina nanofluid

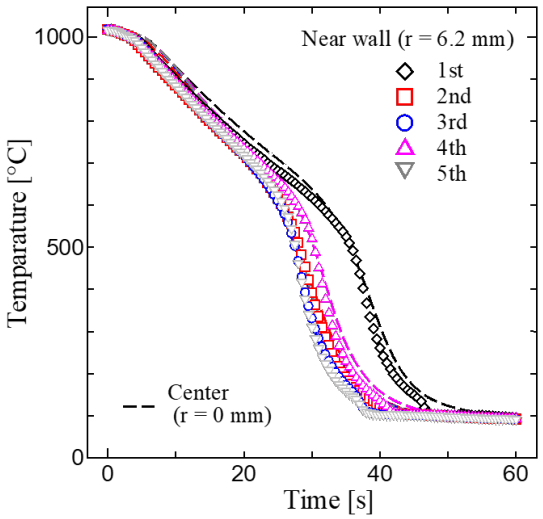

(b) Cooling curves in titanium dioxide nanofluid

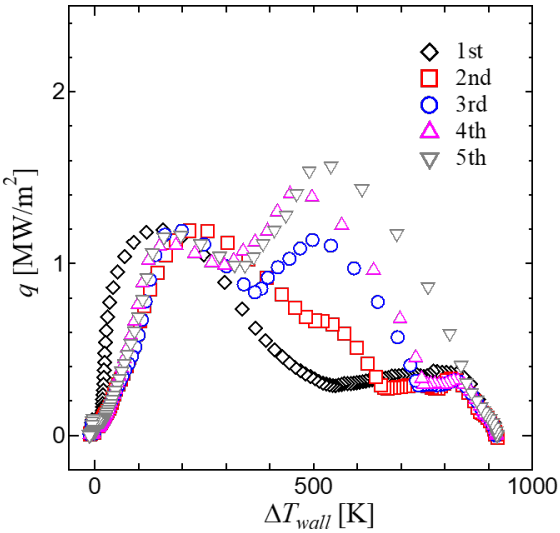

(c) Boiling curvesin alumina nanofluid

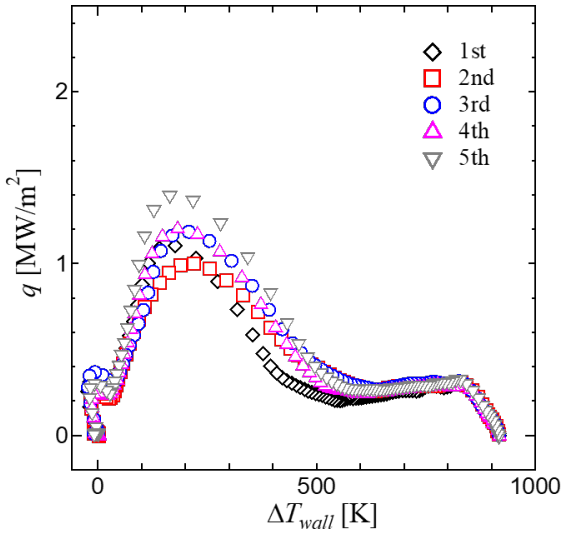

(d) Boiling curves in titanium dioxide nanofluid

Figure 4-8: Cooling and boiling curves in different nanofluids.

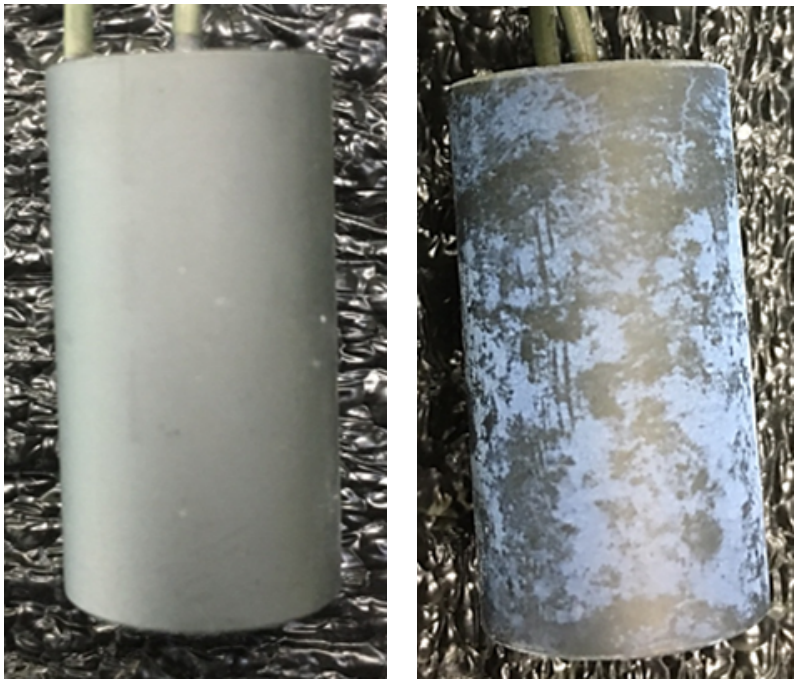

(a) Distilled water (b) Silica nanofluid

(c) Alumina nanofluid (d) Titanium dioxide nanofluid

Figure 4-9: Photos of the test piece taken after the 5th run

4.3.2 Effects of surface properties on T_{MHF}

The cooling and boiling curves in Figs. 4-4, 4-6 and 4-8 indicate that the improvement of cooling rate in nanofluids is mainly attributed to the increase of T_{MHF}. Thus, the mechanism to cause the rise of T_{MHF} is explored in the followings. Kim et al. [80] indicated that the surface roughness promotes solid-liquid contact at high temperature to increase T_{MHF} during quenching. Thus, the average surface roughness Sa was measured using a 3D laser scanning confocal microscope and the relation of Sa and ΔT_{MHF} are presented in Fig. 4-10; here, the symbols and error bars show the average and the range of measurements of Sa at eight locations, respectively. It can be seen that in comparison with the Inconel 718 surface after quenching in water, the values of Sa after quenching in nanofluids are greater. In addition, the value of Sa tends to increase with repeating the experimental runs. It is also seen that ΔT_{MHF} tends to increase with an increase in Sa. To confirm the dependency of ΔT_{MHF} on Sa, the same experiment was done using two SUS304 rodlets: one was the normal rodlet without surface treatment and the other was polished with sandpaper to roughen its surface. The results for these two rodlets are also presented in Fig. 4-10. In the quenching experiment immersing the roughened SUS304 rodlet in water, the surface roughness was largest (Sa = 7.7 μm) but the minimum heat flux temperature was maintained low (ΔT_{MHF} = 524K). This indicates that the surface roughness may have noticeable influence on ΔT_{MHF} but the increase of ΔT_{MHF} measured in this work cannot be attributed solely to the surface roughness. Kang et al. [52] explored the effects of surface wettability on ΔT_{MHF} experimentally to conclude that ΔT_{MHF} is higher for the surface of low contact angle. Thus, to test the effect of surface wettability, the contact angle of the rodlet surface was measured using a contact angle goniometer (PG-X, Fibro System AB). The relation between ΔT_{MHF} and the contact angle is presented in Fig. 4-11.

The value of contact angle was 75±10° in the experiments using distilled water. However, after quenching in nanofluids, the contact angle was measured at zero since droplets were absorbed in the nanoparticle layer formed on the surface. This wet-

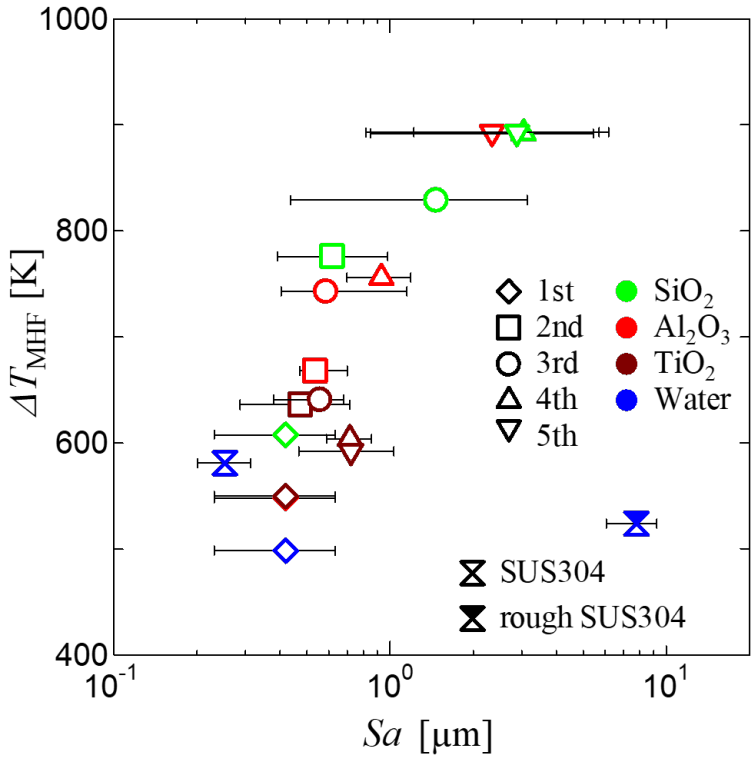

Figure 4-10: Effect of surface roughness Sa on ΔT_{MHF}

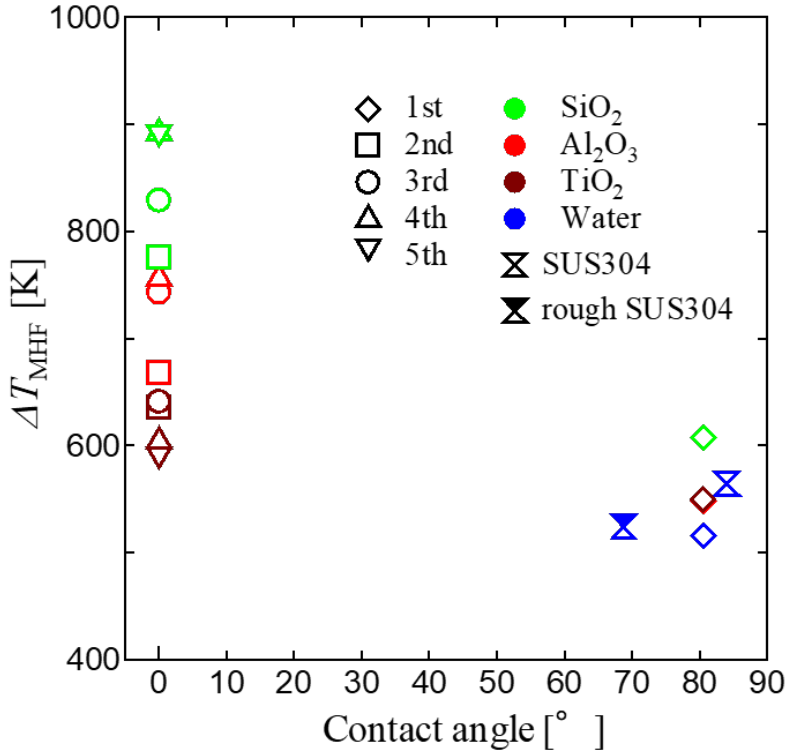

Figure 4-11: Effect of wettability on enhancement of ΔT_{MHF}

ting condition is called spreading wetting. Thus, increasing trend of ΔT_{MHF} with a decrease in contact angle is seen in Fig. 4-11, but it is not possible to express the dependence of ΔT_{MHF} on the properties of nanoparticle layer as a function of contact angle.

Rahman et al. [81] used the wickability that expresses capillary wicking performance of the heat transfer surface to correlate the critical heat flux in pool boiling. The surface wickability Wi was quantified using the liquid volume wicked into the surface per unit time. In this work, by reference to Rahman et al. [81], Wi was determined as follows.

1. The tip of distilled water kept in a capillary tube of 1.04 mm in inner diameter was touched with the surface.

2. The water was absorbed in the nanoparticle layer by wicking action. The liquid volume wicked per unit time was determined from the change in the water level in the capillary tube.

3. From the volumetric flux of the wicked liquid $\dot{V}_0''$, the wickability Wi was calculated by

$$Wi = \frac{\dot{V}_0'' \rho_l}{\rho_g^{1/2} \sigma g (\rho_l - \rho_g)^{1/4}} \tag{4.10}$$

$$\dot{V}_0'' = \frac{1}{A_w} \left(\frac{dV}{dt} \right)_{t=0} \tag{4.11}$$

where the subscript g denotes gas phases, respectively, $(dV/dt)_{t=0}$ is the initial volume flow rate, A_w is the crosssectional area of the capillary tube. Li et al. [82] reported that the transitional heat flux during quenching is enhanced with an increase in the modified Weber number that is equivalent to the square of Wi. Based on this result, they discussed that the wicking performance of the surface influenced the vapor film behavior and transitional heat flux in their experiments. It is therefore probable that the surface wickability affected the value of ΔT_{MHF} in the present experiments. In view of this, the relation of Wi and ΔT_{MHF} is explored in Fig. 4-12; here, the symbols

and error bars show the average and the range of twelve-times measurements of Wi, respectively. It can be seen that in the SiO_2 and Al_2O_3 nanofluids, the value of Wi is fairly constant but ΔT_{MHF} tends to increase with repeating the experiment. In the TiO_2 nanofluid, Wi increases with the experimental run but the value of ΔT_{MHF} is fairly constant. It seems that surface wickability is not the main cause of the heat transfer enhancement measured in this work.

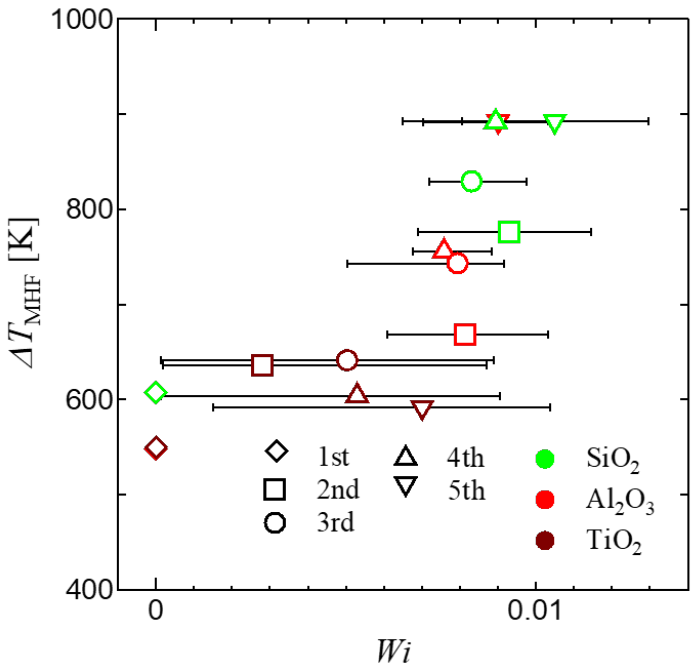

Figure 4-12: Effect of wickability on enhancement of ΔT_{MHF}

4.3.3 Effects of the low-thermal-conductivity layer on the heat transfer surface

The investigation in the previous section suggests that in contrast to the previous studies, the heat transfer enhancement for the nanoparticle-deposited surfaces observed in the present experiments may not mainly be attributed to the modification of surface properties such as roughness, wettability and wickability. It is generally accepted that in film boiling, a high temperature surface is covered totally by a

vapor film (Incropera et al., [83]. Bradfield [84], Yao and Henry [85] and Kikuchi et al. [86] however indicated that instantaneous liquid-solid contact occurs even in the film boiling. Kikuchi et al. [9, 53] further discussed the possibility that the low-thermal-conductivity layer formed on the heat transfer surface causes early collapse of a vapor film during quenching. They developed an intermittent liquid-solid contact model to describe the rise of ΔT_{MHF} for the specimens coated with the low-thermal-conductivity layer. The model postulates that the liquid-solid contact process during film boiling can be divided into three periods: dry, conduction, and evaporation periods. The wall temperature transient during each of the three periods is calculated using the one-dimensional heat conduction equation in cylindrical coordinates Eq. (4.1). The boundary condition on the layer surface is different in each period as shown below.

1. Dry period (t $<$ 0)

   Before the occurrence of instantaneous liquid-solid contact, cooling mechanism of the high temperature specimen is pure film boiling. Denoting the film boiling heat transfer coefficient by h_{fb}, the boundary conditions are given by

   (at r = 0)

   $$\frac{\partial T}{\partial r} = 0 \tag{4.12}$$

   (at r = R)

   $$\lambda_{sp} \frac{\partial T}{\partial r}\bigg|_{sp} = \lambda_{layer} \frac{\partial T}{\partial r}\bigg|_{layer} \tag{4.13}$$

   $$T_{sp} = T_{layer} \tag{4.14}$$

   (at r = R + δ)

   $$-\lambda_{layer} \frac{\partial T}{\partial r} = h_{fb}(T - T_{sat}) \tag{4.15}$$

   where R is the radius of cylindrical specimen, δ is the layer thickness, T_{sat} is the saturation temperature, and the subscripts sp and layer denote the specimen and layer, respectively.

2. Conduction period (0 $\leq$ t $<$ τ_c)

It is supposed that the coolant touches the surface of high-temperature specimen but phase change does not occur during the conduction period. The heat transfer mechanism within this period is heat conduction and the boundary condition on the layer surface is replaced by

(at r = R + δ)

$$T - T_{sat} = \frac{T_{sp} - T_{sat}}{\left(1 + \frac{h_{fb}\delta}{\lambda_{layer}}\right)\left(1 + \sqrt{\frac{\rho_l c_l \lambda_l}{\rho_{layer} c_{layer} \lambda_{layer}}}\right)} \tag{4.16}$$

where the subscript l denotes the coolant.

3. Evaporation period ($\tau_c \leq$ t $\leq \tau_c + \tau_e$) Evaporation commences at t = τ_c and continues for the period of τ_e. The boundary condition on the layer surface is hence given by

(at r = R + δ)

$$-\lambda_{layer}\frac{\partial T}{\partial r} = q_e \tag{4.17}$$

where q_e denotes the evaporation heat flux.

The heat conduction equation (Eq. (4.1)) is discretized based on the finite-difference method to calculate the temperature transient using fully-implicit scheme for time integration. It is supposed that if the superheat of the layer surface becomes lower than the critical value ΔT_{iso}, the film boiling is finished and the transition boiling begins. The values of h_{fb}, ΔT_{iso}, q_e, τ_e and τ_c recommended by Kikuchi et al. [9] are listed in Table 4.2. In our quenching experiments using nanofluids, the rodlets were covered with the layer of nanoparticles. The average nanoparticle layer thickness was within 2 - 12 µm as presented in Fig. 4-13. Since the thermal conductivities of nanoparticle materials were lower than that of Inconel 718, the situation is similar to that supposed by Kikuchi et al. [9,53]. Thus, it is also probable that the improvement of ΔT_{MHF} measured in this work can be described using Kikuchi et al.'s model. It should however be noted that evaluation of the nanoparticle layer properties is not simple since it has porous structure. The method to estimate the properties of the

nanoparticle layer used in this work is described as follows. First, the nanoparticle layer density ρ_{nl} is calculated simply from its mass and volume by

$$\rho_{nl} = \frac{m}{\pi L \{(R + \delta_{ave})^2 - R^2\}} \tag{4.18}$$

where m is the total mass of nanoparticle layer, δ_{ave} is the average nanoparticle layer thickness, and L is the length of the rodlet. Using ρ_{nl}, porosity of the nanoparticle layer ε is determined by

$$\varepsilon = \frac{\rho_n - \rho_{nl}}{\rho_n} \tag{4.19}$$

where the subscript n denotes the nanoparticle material. It was assumed that the pore of the nanoparticle layer was filled with water vapor during film boiling before ΔT_{MHF} is reached. The effective specific heat of the nanoparticle layer c_{layer} is hence estimated as a function of ε as

$$A = \frac{\varepsilon \rho_v}{\varepsilon \rho_v + (1 - \varepsilon)\rho_n} \tag{4.20}$$

$$c_{nl} = A c_v + (1 - A) c_n \tag{4.21}$$

where the subscript v denotes the water vapor. Finally, the effective thermal conductivity of the nanoparticle layer λ_{nl} is calculated by

$$\lambda_{nl} = \varepsilon \lambda_v + (1 - \varepsilon)\lambda_n \tag{4.22}$$

To calculate the value of ρ_{nl} for each nanoparticle material by Eq. (4.18), δ_{ave} was measured using the laser microscope after four-times quenching; then, the nanoparticle layer was removed from the rodlet with a spatula to measure m using the electronic balance. The thermal properties of SiO_2, Al_2O_3 and water vapor are presented in Table 4.3; here, the thermal properties of nanoparticle materials and water vapor were referred to Refs. (JSME [10], Lemmon et al. [11]), respectively. As for TiO_2, it was changed to titanium yellow whose thermal properties are unknown during the experiment. Thus, the properties of TiO_2 are not included in Table 4.2 and its experimental

results are not used in the following analyses. The calculated thermal properties of the nanoparticle layers are presented in Table 4.4. It can be confirmed that the estimated thermal conductivities of the nanoparticle layers are much lower than that of the rodlet material.

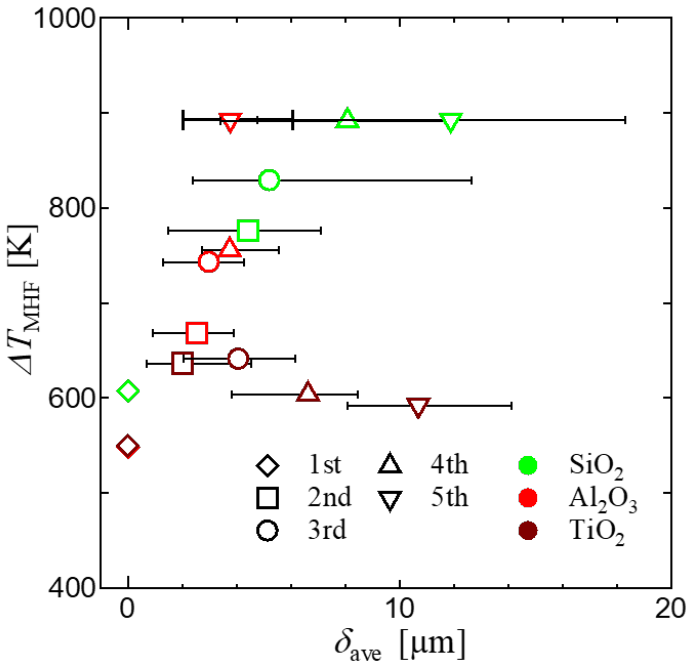

Figure 4-13: Effect of average nanoparticle layer thickness on enhancement of ΔT_{MHF}

Table 4.2: Parameters used in the Kikuchi model [9]

Parameter	
h_{fb} [W/m^2 · K]	280
ΔT_{iso} [K]	130
q_e [W/m^2]	1.5×10^6
τ_e [ms]	50
τ_c [ms]	10

The temperature transients at the nanoparticle layer surface calculated using

Table 4.3: Properties of the nanoparticle layer materials [10] and water vapor [11]

	Density ρ [kg/m^3]	Thermal conductivity λ [W/m · K]	Specific heat c [J/kg · K]	Weight m [mg]	Porosity ε [-]
SiO_2	2580	3.06	1225	0.75	0.983
Al_2O_3	3926	13	1181	0.47	0.978
Vapor (water) at 550 °C	0.26	0.072	2168	-	-

Kikuchi et al.'s model is displayed in Fig. 4-14, where the initial temperature was set to 1000 °C as in the experiments. Since the formation of nanoparticle layer occurs during nucleate boiling, it is supposed that the nanoparticle layer was not present on the rodlet surface when ΔT_{MHF} was reached in the first experimental run. Thus, Kikuchi et al.'s model was applied to the subsequent runs. It can be seen in Fig. 4-14 that the calculated surface temperatures fell far below the critical temperature T_{iso} (= 230°C) as soon as liquid-solid contact occurs. This implies that the value of T_{MHF} is estimated higher than 1000°C. In addition, the calculated temperature transient is hardly influenced by the number of experimental runs for each nanofluid. These are not consistent with the present experimental results.

Table 4.4: Estimated properties of the nanoparticle layers

	Density ρ_{nl} [kg/m^3]	Thermal conductivity λ_{nl} [W/m · K]	Specific heat c_{nl} [J/kg · K]
SiO_2	41.8	0.12	1483
Al_2O_3	82.6	0.34	1306

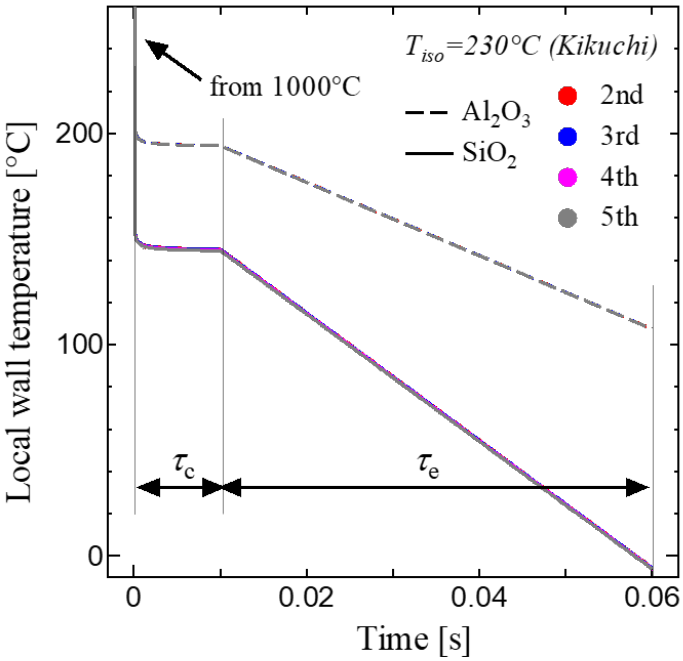

Figure 4-14: Temperature transients calculated using Kikuchi et al.'s model

4.3.4 Proposal of a new model for T_{MHF}

Since the existing models were not satisfactory to explain the values of T_{MHF} measured in this work, it was tried to develop a new model for quenching of the specimen covered with a thin nanoparticle layer. The new model calculates the temperature histories within the specimen, nanoparticle layer, and the coolant after the nanoparticle layer instantaneously contacts with the coolant. The one-dimensional heat conduction equation in cylindrical coordinates Eq. (4.1) is used as a governing equation. To derive the temperature transients, Eq. (4.1) was discretized based on the finite difference method. The central difference scheme was applied to the space-derivative term and the explicit Euler method was used for time integration. The mesh size was set to 0.1 µm and the time step was set so as to satisfy von Neumann's stability condition [64]. It was confirmed that mesh-size dependency of the numerical results was sufficiently small. The initial temperature was set to 1000 °C in the specimen and the nanoparticle layer and 100 °C in water. At the outside boundaries of the regions of specimen and water, the constant temperature conditions of 1000 °C and 100 °C were applied, respectively. As a typical example, Fig. 4-15 displays the temperature

transient at the nanoparticle layer surface calculated for the second run in the silica nanofluid. Here, the nanoparticle layer thickness measured after the first run was used in the simulation assuming that the nanoparticle layer was mainly formed during nucleate boiling in the previous runs. It can be seen that the surface temperature falls rapidly from 1000 °C to 149 °C after the contact. This value is far below the minimum heat flux temperature of 361 °C that is estimated using the widely accepted correlation by Dhir and Purohit [78]. However, by virtue of the heat supplied from the high-temperature specimen, the surface temperature recovers to 361 °C within a short time period of 0.23 ms. Thus, solid-liquid contact would be permitted only for τ_c = 0.23 ms in this case. It is considered that to achieve vapor film collapse, solid-liquid contact should be maintained for sufficiently long time for nucleate boiling to occur. Otherwise, local instantaneous solid-liquid contact disappears and the nanoparticle layer surface is covered with the vapor film again. The contact time is dependent on the thermal properties and thickness of the nanoparticle layer. Figure 4-16 presents the relation between the contact duration τ_c and ΔT_{MHF}, indicating that ΔT_{MHF} tends to increase with an increase in τ_c as expected. However, the trend seems different between the silica and alumina nanofluids. In particular, in the fifth run in the alumina nanofluid, the calculated contact duration is short but the value of ΔT_{MHF} is very high. One of the possible reasons for the different trend is the difference in the porous structure of the nanoparticle layer formed in the silica and alumina nanofluids. The effect of porous structure on the effective thermal properties of the nanoparticle layer and the quenching characteristics should hence be investigated in future studies.

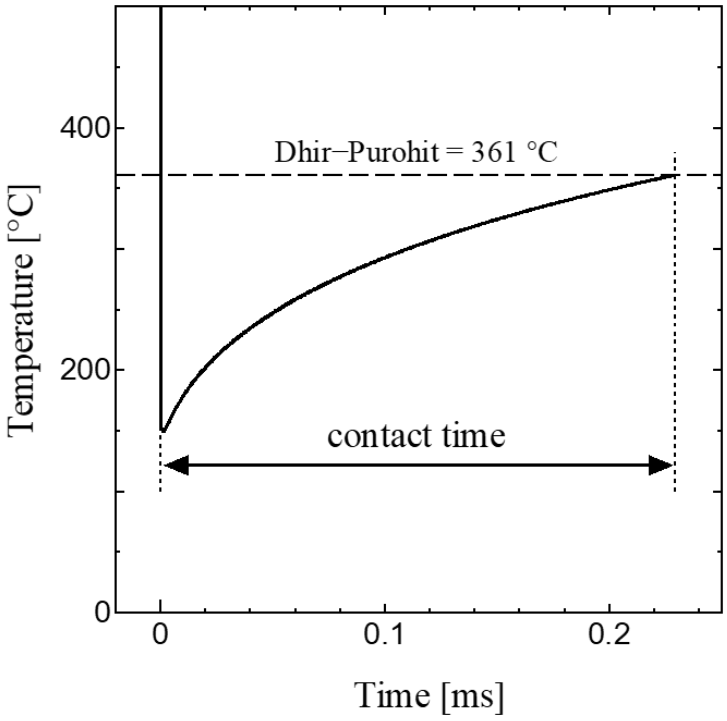

Figure 4-15: Temperature history after liquid-solid contact on the silica nanoparticle surface from 1000 °C

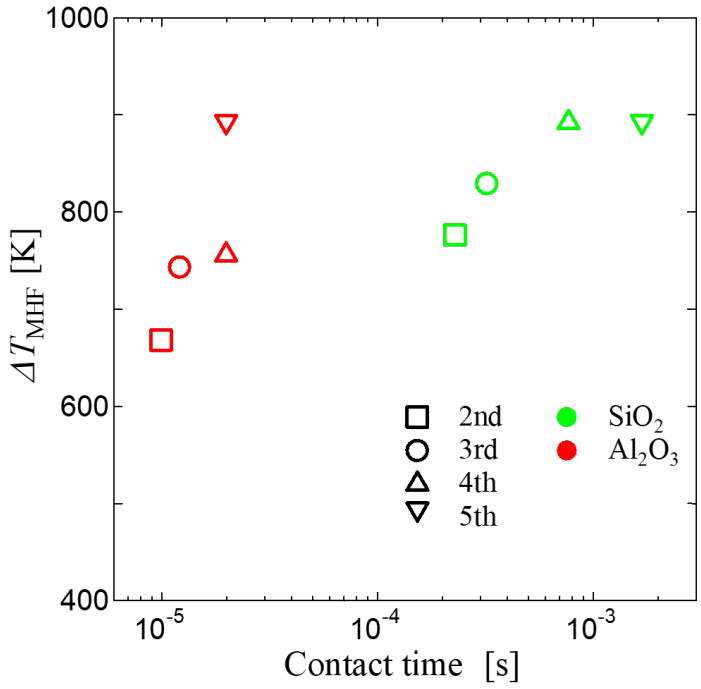

Figure 4-16: Effect of contact time on enhancement of ΔT_{MHF}

4.3.5 Conclusions

The minimum heat flux temperature during quenching in nanofluid was studied experimentally using Al_2O_3, SiO_2 and TiO_2 as the nanoparticle materials dispersed in the base liquid. Main conclusions of this work are summarized as follows.

1. The minimum heat flux temperature rises in nanofluid due to formation of nanoparticle layer on the heat transfer surface during nucleate boiling. The rate of the heat transfer enhancement depends on nanoparticle layer's material and thickness.

2. No simple dependency of the minimum heat flux temperature enhancement on the surface parameters of the nanoparticle layer (roughness, wettability and wickability) was found. It was also not possible to explain the rise of the minimum heat flux temperature solely from the reduction of the contact temperature caused by the nanoparticle layer of low thermal conductivity

3. A new model that describes the rise of the minimum heat flux temperature from the contact duration of the nanoparticle layer with the coolant was proposed. The model succeeded to explain the rise of the minimum heat flux temperature with an increase in the nanoparticle layer thickness. It should however be noted that the rise of the minimum heat flux temperature was not expressed as a single function of the contact duration if the nanoparticle material was different. It was discussed that the porous structure of the nanoparticle layer would be dependent on the nanoparticle material and might have influences on the effective thermal properties of the nanoparticle layer and the process of quenching.

Chapter 5

Evaluation of the Performance of Nanofluid as Quenching Coolant

5.1 Introduction

This chapter describes a study of the performance of nanofluid as heat treatment (quenching process) coolant in the steel industry. From the previous chapter, silica nanofluid shows excellent cooling performance. Therefore, silica nanofluid uses as a quenching coolant in this chapter. Heat treatment is an essential process in the material modification of steel, such as hardness. Especially, this study deals with the immersion cooling method in the quenching process. Heat treatment coolant requires two characteristics: rapid cooling and uniformed cooling, but nothing satisfies both of those needs. The present study explored nanofluid's effectiveness as heat treatment coolant for Inconel 718 is experimental as follows. First, two characteristics (rapid cooling and uniformed cooling) are confirmed in a nanofluid. Second, the capability of silica nanofluid for heat treatment is checked from the Vickers hardness test.

5.2 Literature review

Heat treatment for Inconel 718 has consisted of three steps [87]. First, solution treatment: At room temperature, the alloy consists of two phases. By exposing the

alloy to a high temperature, a solid solution is created. Second, quenching process: Rapid cooling of the solid solution to make a supersaturated solid solution. Third, Aging treatment: Supersaturated solid solution is left at room temperature or heated weakly. Hardening is produced by the precipitation of γ'' particles [88, 89]. The present study focuses on the quenching process, which is essential to determine the hardness of Inconel 718. And also, this process is used in ordinary procedures in other heat treatment methods. A lot of liquid is applied to quenching coolant for heat treatment, such as water and oil, high-density salt solution, mineral oil [90–93]. When the fastest coolant water is used as the coolant, the cooling speed is not uniformed due to film boiling in the initial cooling step. This non-uniformity cooling causes crack of products [94]. One of the solutions for non-uniformity cooling is proposed to reduce cooling speed by using polymer solution, or oil [95, 96]. However, slow cooling does not lead to enough quality of product such as hardness. Recently, it is proposed that nanofluid is an effective heat transfer fluid. Nanofluid enhance critical heat flux (CHF) in pool boiling [37, 44, 47, 49, 50, 97, 98] and minimum heat flux temperature (T_{MHF}) [80]. It is considered that the mechanism of these phenomena is caused by nanoparticle layer that is formed on heat transfer surface [38,80,99]. In this study, the effectiveness of silica nanofluid for heat treatment coolant is investigated experimentally. First, cooling speed is compared with distilled water in immersion cooling. Second, the temperature distribution in the test piece is checked in immersion cooling. Finally, the effect of nanofluid is confirmed by the Vickers hardness test.

5.3 Experimental

Water-based silica nanofluid was prepared in the same procedure (sec. 4.2.1). And also, sec. 4.3 compared the cooling speed between distilled water and silica nanofluid. This section introduces two types of experiments to confirm the temperature distribution of test pieces during immersion cooling and the effectiveness of nanofluid for heat treatment.

5.3.1 Temperature distribution measurement experiment in the test piece during immersion cooling

The temperature distribution that was in the test piece was measured during immersion cooling experimentally. For this test, SUS304 rodlets (ϕ15 × 30 mm) were used due to circumstances in the manufacture of the thermocouple insertion hole. The properties of Inconel 718 and SUS 304 were same order in Table 4.1. Thus, the temperature distribution that occurs inside the rodlet was considered to be qualitatively similar. In Fig. 5-1, rodlets had two different depth holes (ϕ1.6 mm) at 4 mm from the wall. The depth of the two holes was 5 mm and 20 mm from the upper surface of rodlets. The experimental procedure was the same as sec. 4.2.3.

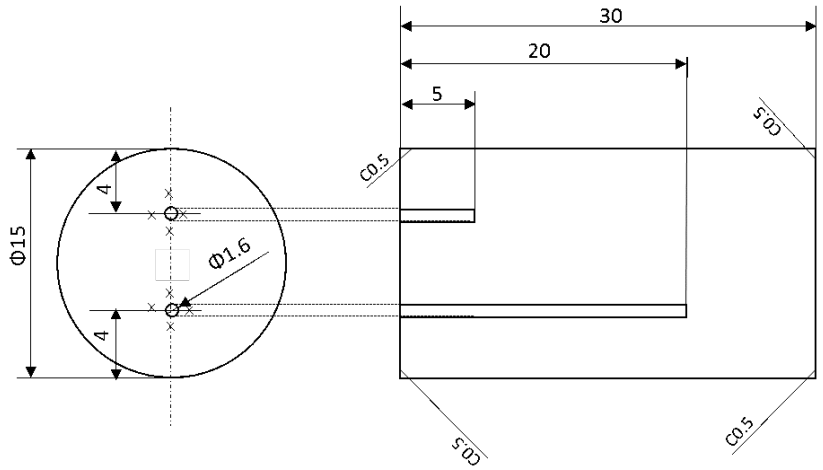

Figure 5-1: Dimension of the test piece (SUS304)

5.3.2 Measurement experiment of test piece hardness by aging treatment

It is known that the hardness of Inconel 718 is increased by aging treatment, and cooling speed before aging treatment plays an important role in the hardness [88,89]. Therefore, in this study, four different cooling (furnace cooling, air cooling, quenching

in distilled water, and quenching in silica nanofluid) was conducted in the quenching process. Experimental procedures are referred to as Aoki's method [100] as follows.

1. Test piece was cleaned with acetone and distilled water.
2. Test piece was kept in an electric furnace at 1025 °C for 10 minutes.
3. (First quenching process) Test piece was immersed in 1 L of coolant with a subcooling degree of 20 K and cooled to a temperature equal to that of the coolant. Distilled water was used as a coolant in case the cooling method of the second quenching process is quenching in distilled water, air cooling, and furnace cooling. When the sample is quenching in silica nanofluid in the second process, coolant was silica nanofluid used in the first process.
4. (Solution treatment) Test piece was kept in an electric furnace at 982 °C for one hour.
5. (Second quenching process) Four different cooling was conducted.
6. (Aging treatment) Test piece was kept in an electric furnace at 718 °C for 8 hours, then, test piece cooled down to 621 °C by furnace cooling and was kept for 8 hours. Finally, air cooling (at room temperature) was conducted.
7. (Vickers hardness test) Test piece was cut at 15 mm in the axial direction. Vickers hardness was measured 10 points every 0.5 mm from the circular surface to the center on a cutting surface. The load was 10 kgf, and the time is 10 s.

5.4 Result and discussion

5.4.1 Temperature distribution in test piece during immersion cooling

In Fig. 5-2, temperature history that was recorded at different depths (5 mm (Shallow) and 20 mm (Deep) from upper surface) is shown in the second cooling test. In

the case of distilled water, cooling was begun from a shallow position during film boiling. This may reflect the distance from the surface. While the shallow position is at 5 mm from the upper surface, the deep position is at 10 mm from the bottom surface. Rapid cooling was started with the deep position before the shallow position since vapor film collapse with nucleate boiling advanced from the bottom of rodlet to upward in Fig. 4-5. Temperature difference ($\Delta T_{\mathrm{SD}} = T_{\mathrm{Shallow}}$ - T_{Deep}) history shows in Fig. 5-3. Maximum temperature difference (ΔT_{SD} = 130 K) was occurred at 38 s due to the gap in the timing of vapor film collapse. Next, the temperature difference of the test piece in silica nanofluid was considered. In Fig. 5-2, the temperature difference history was the same with distilled water during film boiling. Cooling was progressed from the shallow position due to the difference in distance from the surface. After that, the temperature difference became small since rapid cooling was started in the full surface at about 900°C (Fig. 4-7(c)). Then, cooling proceeded from the bottom surface with nucleate boiling in Fig. 4-7 (e, f). The temperature difference is similar to distilled water in this regime. As a result, in silica nanofluid, maximum temperature difference (ΔT_{SD} = 90 K at 14 s) is smaller than distilled water in Fig. 5-3. In summary of the effect of silica nanofluid against temperature difference during immersion cooling, silica nanofluid is possible to mitigate temperature difference in the axial direction in immersion cooling. Therefore, when silica nanofluid is applied as a quenching coolant, the probability of occurrence of the defects such as crack and deformation can be reduced.

5.4.2 Hardness of test piece after aging treatment

After solution treatment, four different cooling methods (furnace cooling, air cooling, quenching in distilled water, and quenching in silica nanofluid) were done. The temperature history measured at the center of the test piece is shown in Fig. 5-4. Average cooling speed was calculated from the time required to cool the test piece from 982 °C to 600 °C in each cooling method [100]. The calculation results show in Table 5.1

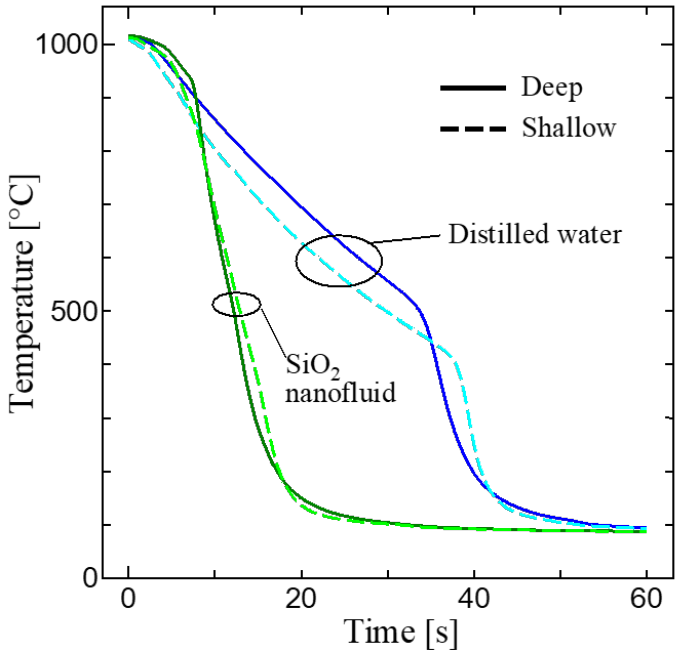

Figure 5-2: Temperature transients measured at two elevations within the test piece (SUS304, ϕ 15 $\times$ 30 mm)

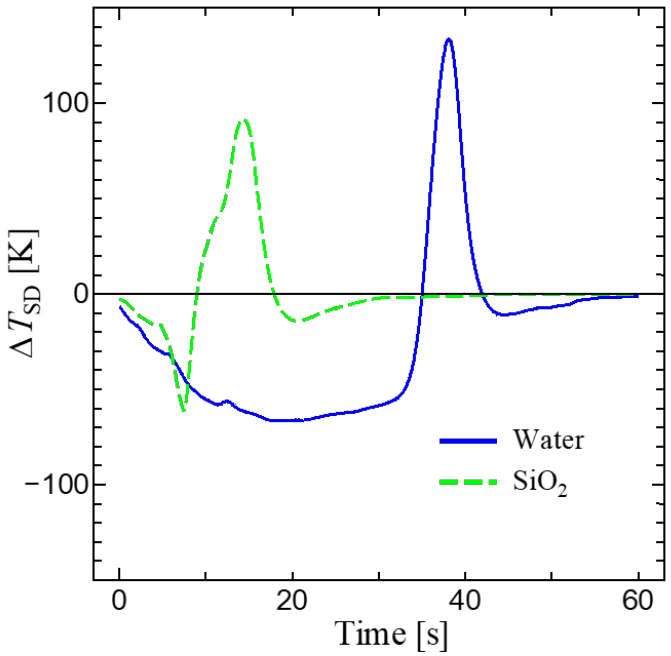

Figure 5-3: Transients of temperature difference between the two elevations within the test piece (SUS304, ϕ 15 $\times$ 30 mm)

for each measurement position. As a result, average cooling speed increased in the order of furnace cooling, air cooling, quenching in distilled water, and quenching in silica nanofluid. Based on the average cooling speed of furnace cooling, the average cooling speed is 16 times in air cooling, 74 times in quenching in distilled water, and 175 times in quenching in silica nanofluid. In Fig. 5-5, the average cooling speed at the center is compared with Rockwell hardness. It is noted that Vickers hardness measured in this study was converted to Rockwell hardness to compare with previous research.

The plots in Fig. 5-5 show average hardness in 8 measurements except for the maximum and minimum values. And error bars show maximum and minimum values in 8 measurements. As well as previous research results, Rockwell hardness was increased with cooling speed after solution treatment. However, the silica nanofluid and distilled water case displayed almost the same Rockwell hardness. The reason is considered that a higher cooling rate is needed to make harder Inconel 718.

Table 5.1: Time-averaged cooling rate

[K/min]

	Furnace cooling	Air cooling	Quenching in distilled water	Quenching in silica nanofluid
r = 0	12.8	21.4	958	2243
r = 6.2	12.8	222	940	2319

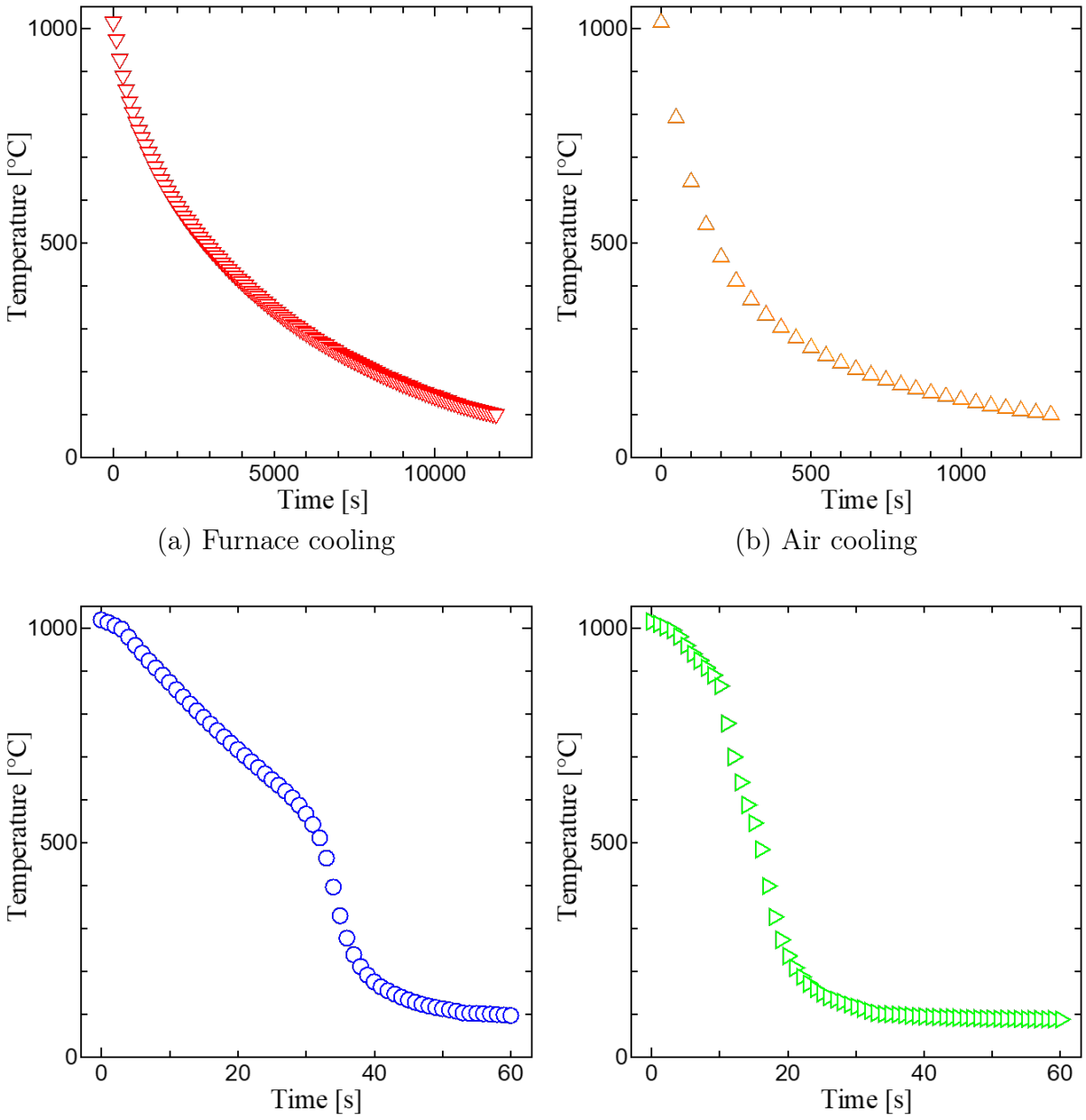

(a) Furnace cooling

(b) Air cooling

(c) Quenching in distilled water

(d) Quenching in silica nanofluid

Figure 5-4: Transient of test piece (Inconel718, ϕ16×30 mm) temperature during cooling after solution treatment

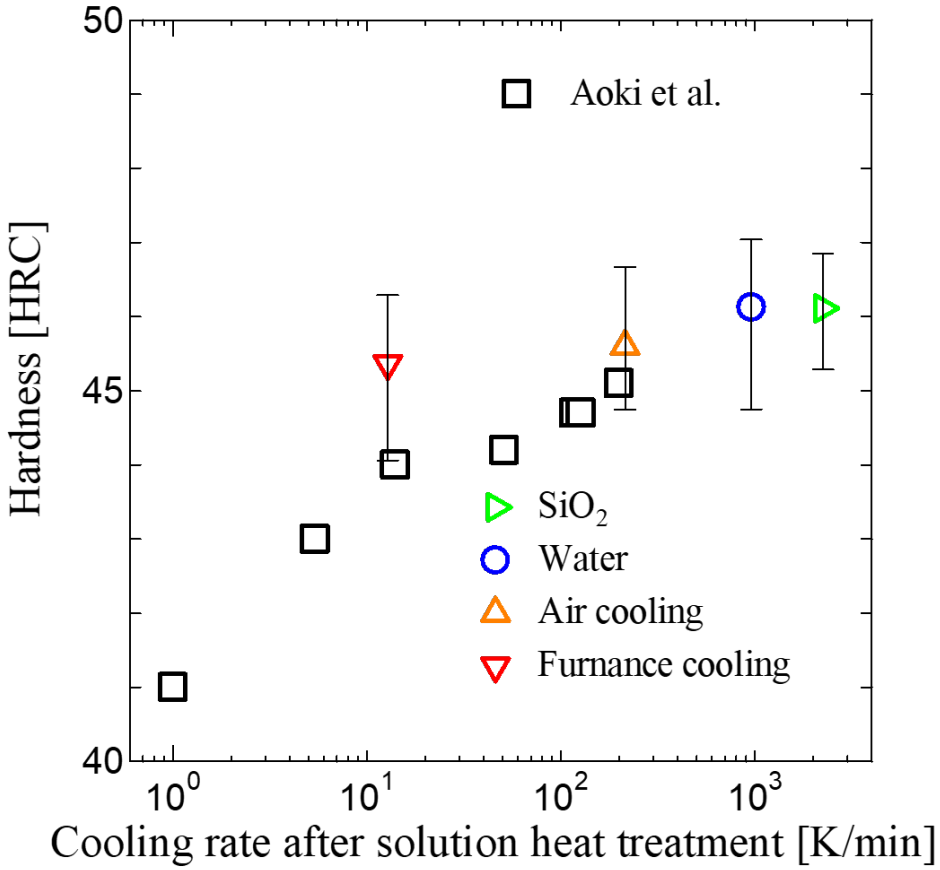

Figure 5-5: Hardness of test pieces (Inconel718, ϕ 16 $\times$ 30 mm) measured after aging treatment

5.5 Conclusions

The effectiveness of silica nanofluid as a quenching coolant was evaluated experimentally. The main findings of the present study are as follows.

1. When distilled water is used for quenching coolant, the temperature difference in axial direction expands due to the collapse of vapor film from the bottom. On the other hand, silica nanofluid reduces temperature differences in the axial direction. This is because vapor film collapse on the full surface at the same time. Therefore, it is considered that the unique phenomenon of silica nanofluid can prevent the products from crack and deformation during the quenching process.

2. Silica nanofluid is applied as a quenching coolant to make harder Inconel 718. As well as previous research, the hardness of Inconel 718 was improved by silica nanofluid quenching. However, the improvement of hardness is limited from the comparison with quenching in distilled water.

Future work includes a new faster cooling method to improve material properties and a more systematic investigation of the effect of nanofluid on material properties such as tensile test and material structure observation.

Chapter 6

Conclusions and recommended future work

The present study investigated quenching phenomena during rapid cooling of high-temperature objects. First, the details of the quenching phenomenon are elucidated from falling liquid film cooling experiment. Second, the enhancement technique of quenching phenomenon in nanofluids is studied. Each quenching phenomenon has confirmed the details of the phenomenon and developed the model to explain the phenomenon.

In Chapter 2, the quenching model for falling liquid film cooling was developed as HTC distribution based on experimental data. Since the limited performance of measuring instruments could not measure transient temperature distribution during falling liquid film cooling, the existing models (HTC distribution) were set up so that the calculated quenching velocity would match the experimental values. Thus, previous models proposed various HTC distributions. This study measured the transient temperature distribution directly during the falling liquid film cooling along a thin copper plate using a high-speed infrared ray (IR) camera. Four critical parameters (wetting temperature, peak of HTC, HTC distribution in wet and dry region) which compose the quenching model were decided from experimental results as experimental correlations. The new quenching model predicted experimental quenching velocity in the case of thin copper plate in ± 20 %. To validate the new quenching model,

quenching velocity was measured in a thick copper plate. The predicted values agreed with experimental data in ± 30 %. The experiment and analysis confirmed that the new quenching model is reasonable to estimate the quenching velocity. Future work needs to verify the validity of the experimental correlations by measuring quenching velocity on heat transfer plates with different properties such as SUS304, aluminum, and zircaloy.

In chapter 3, the quenching phenomenon was observed from the heat transfer phenomenon and liquid film condition using a synchronized high-speed camera and high-speed IR camera. Silicon wafer, which is transparent against infrared rays, was used as a heat transfer plate. The transient of wall temperature distribution was measured directly by using a high-speed IR camera. Moreover, liquid film condition during quenching was observed by using a high-speed camera. Based on the synchronized images and calculated heat flux distribution, the following is what we know about the heat transfer phenomenon during quenching near the liquid film front. The primary heat transfer mechanism is nucleate boiling. Liquid film cooling has three different heat transfer regions (wet, sputtering, and dry region from upstream) In the wet region, the stable liquid film exists on the wall. In the sputtering region, the stable liquid film does not exist due to the nucleate boiling, wet and dry condition is repeated. In the dry region, liquid film can not reach due to peeling off the liquid film from the wall in the sputtering region. The length of the sputtering region was the same size as the bubbles generated by nucleate boiling. Based on the above quenching mechanisms, a new quenching model is defined. The new quenching model estimates wetting velocity from this study in the error of ± 20 % and from previous research in the error of ± 30 %. In future work, quenching model should include the effect of not considered experimental parameters such as subcooling and liquid properties.

In chapter 4, the unique quenching phenomenon in nanofluid was elucidated by the model about contact duration between coolant and nanoparticle layer. Immersion cooling experiments were conducted from 1000 °C in distilled water, three nanofluid (SiO_2, Al_2O_3, TiO_2). SiO_2 and Al_2O_3 nanofluid indicated a unique quenching phenomenon and improved the heat transfer due to high minimum heat flux temperature

T_{MHF}. One of the unique quenching phenomenon triggers was the nanoparticle layer formed on the surface of high-temperature objects during immersion cooling. Thus, the properties of the nanoparticle layer (roughness, wettability, and wickability) were investigated, but these properties did not show a significant effect against enhancement of T_{MHF}. On the other hand, it was found that low thermal conductivity of nanoparticle layer is possible to cause liquid-solid contact under film boiling due to low contact temperature. Therefore, liquid-solid contact duration was calculated using effective thermal conductivity of nanoparticle layer estimated from thickness and weight of nanoparticle layer. Finally, a unique quenching phenomenon was explained by comparing the contact duration and minimum heat flux temperature. To develop the model, future work organized the effect of various concentrations and materials of nanofluid.

In chapter 5, the effectiveness of nanofluid for quenching coolant was confirmed experimentally. It was confirmed that nanofluid has two important characteristics: uniform cooling and high efficient cooling as a quenching coolant. The hardness of Inconel 718, which was conducted quenching in nanofluid, did not show the major difference with the Inconel 718, which was conducted quenching in water. The effectiveness of nanofluid in heat treatment has to consider other material properties, such as tensile test and material structure observation.

Nomenclature

Δh latent heat [kJ/kg]

ΔT_{MHF} $(= T_{\mathrm{MHF}} - T_{\mathrm{sat}})$ [K]

ΔT_{sub} $(= T_{\mathrm{sat}} - T_l)$ [K]

ΔT_{wet} $(= T_{\mathrm{wet}} - T_{\mathrm{sat}})$ [K]

ΔT_{iso} isothermal minimum film boiling temperature

ΔT_{SD} $(= T_{Shallow} - T_{Deep})$

$\dot{V}_0''$ wicked volume flux [mm/s]

A_w cross-sectional area of capillary tube [mm^2]

Bi Biot number [-]

c specific heat [J/kg·K]

d diameter [mm]

d_{film} liquid film thickness [m]

G flow rate [kg/s]

g gravitational acceleration [m/s^2]

h heat transfer coefficient [kW/m^2·K]

h^* dimensionless heat transfer coefficient (= h $l_{\mathrm{vis}}/\lambda_l$) [-]

L_a Laplace capillary length Eq.(2.8) [m]

L_{wet} width of wetted area by the liquid film [m]

L_{dry} length of dry region [mm]

l_{heat} heated surface length [m]

l_{vis} viscous length scale (= $(\mu_l^2/(\rho_l^2 g))^{1/3}$) [m]

Nu Nusselt number Eq. (2.6) [-]

P pressure [Pa]

P_{ata} pressure [ata]

Pe Peclet number, (=$\rho\delta c V_{wet}/\lambda$)[-]

Pr Prandtl number [-]

q heat flux [W/m^2]

q_e evaporation heat flux [W/m^2]

R radius [m]

Sa surface roughness [µm]

t time [s]

T_e environmental temperature [°C]

T_{crit} saturation temperature [K]

T_{MS} maximum liquid superheat [K]

T_{sat} saturation temperature [K]

T_{w0} initial wall temperature [°C]

T_{wet} wetting temperature [K]

u_e liquid film velocity [m/s]

V_{wet} quenching velocity [m/s]

We Weber number Eq. (2.9) [-]

Wi wickability Eq. (4.10) [-]

x spatial coordinate in the horizontal direction

y spatial coordinate in the direction perpendicular to the wall

z spatial coordinate in the vertical direction

Abbreviations

CHF Critical heat flux

ECCS Emergency core cooling system

HTC Heat transfer coefficient

ITO Indium tin oxide

IVR In-vessel retention

LOCA Loss of coolant accident

LWR Liquid water reactor

Greek

α thermal diffusivity [m^2/s]

β coefficient of thermal expansion ($= 1/(T_e + 273)$) [1/K]

δ thickness [m]

Γ liquid film flow rate [kg/m·s]

λ thermal conductivity [W/m·K]

μ viscosity [Pa·s]

ν kinematic viscosity [m^2/s]

ϕ volume fraction

Ψ flow rate per unit perimeter [g/cm·s]

ρ density [kg/m^3]

σ surface tension [N/m]

τ_c duration of conduction period [ms]

τ_e duration of evaporation period [ms]

θ dimensionless temperature [-]

θ^* dimensionless wall superheat Eq. (2.15) [-]

θ_0 dimensionless quenching temperature, $(= (T_{w0} - T_{quench})/(T_{w0} - T_{sat}))$ [-]

θ_1 dimensionless temperature, $(= (T_{w0} - T_{quench})/(T_{quench} - T_{sat}))$ [-]

ε porosity

Subscript

$Deep$ Deep position

dry Dry region

fb film boiling

g gas

l liquid

$layer$ layer

n nanoparticle

nl nanoparticle layer

$peak$ peak value

$Shallow$ Shallow position

sp specimen

v vapor

w wall

wet Wet region

Publications

Journal

1. Yutaro Umehara, Tomio Okawa, Role of nanoparticle layer in determining minimum heat flux temperature during quenching of high-temperature body, MEJ special issue, (17P), 2021

2. Tomio Okawa, Keisuke Yamagata, Yutaro Umehara, Measurement of heat transfer coefficient profile during quenching of a vertical hot wall with a falling liquid film, Nuclear Engineering and Design 363, 110629(6P), 2020

3. Yutaro Umehara, Tomio Okawa, Koji Enoki, Evaluation of the Performance of Nanofluid as Quenching Coolant, Tetsu-to-Hagane, Vol. 105, No. 11, pp18-26, 2019

4. Yutaro Umehara, Keisuke Yamagata, Tomio Okawa, Spatial distribution of heat transfer coefficient in the vicinity of wetting front during falling liquid film cooling of a vertical hot wall, Heat and mass transfer 185, 122422, 2022

International conference proceedings

1. Yutaro Umehara, Tomio Okawa, Microscopic Heat Transfer Characteristics During Cooling of High Temperature Surface by a Falling Liquid Film, 28th International Conference on Nuclear Engineering, ICONE28-61737, Online, (2021.8)

2. Yutaro Umehara, Tomio Okawa, Prediction of extremely high minimum heat

flux point during quenching in nanofluid, ASME's Nuclear Engineering Conference powered by ICONE, ICONE2020-4660, Online, (2020.8)

3. Yutaro Umehara, Koji Enoki, Tomio Okawa, Effect of surface properties on quenching characteristics of high-temperature body, 10th International Symposium on Measurement Techniques for Multiphase Flow, Hong-Kong (China), (2017.12)

4. Marco Pellegrini, Masanori Naitoh, Yutaro Umehara, Keisuke Yamagata, Tomio Okawa Experimental evaluation of heat transfer during clad rewetting, 27th International Conference on Nuclear Engineering, Ibaraki (Japan), (2019.5)

5. Yutaro Umehara, Tomio Okawa, Phenomenological interpretation of heat transfer coefficient distribution near the rewetting front, 19th International Topical Meeting on Nuclear Reactor Thermal Hydraulics (NURETH-19), (2022.3) (submitted)

Appendix A

Estimation of the temperature difference between the two sides of the copper plate

In this work, assuming that the copper plate was sufficiently thin, the temperature distribution on the heat transfer surface was measured using the infra-red camera from the back side of the plate. To explore the validity of this assumption, the temperature difference between the two faces is evaluated. First, the Biot number in the present experiment is calculated by

$$Bi = \frac{h\delta}{\dfrac{\delta}{\left(\dfrac{\delta_{copper}}{\lambda_{copper}} + \dfrac{\delta_{Blackbody}}{\lambda_{Blackbody}}\right)}} \simeq 0.09 \tag{A.1}$$

where the maximum value measured in the experiments is used for h (= 63162 W/m^2·K), the thickness of the wall including blackbody layer is used for δ, and the values of λ are evaluated at the initial wall temperature at which the maximum h was measured (= 543 K). As a result, the Biot number in the present experiments was estimated less than 0.1. In this case, the error associated with the lumped capacitance assumption adopted in this work is estimated negligible [101]. As a typical example, the temperature profiles on the two faces calculated using the finite differ-

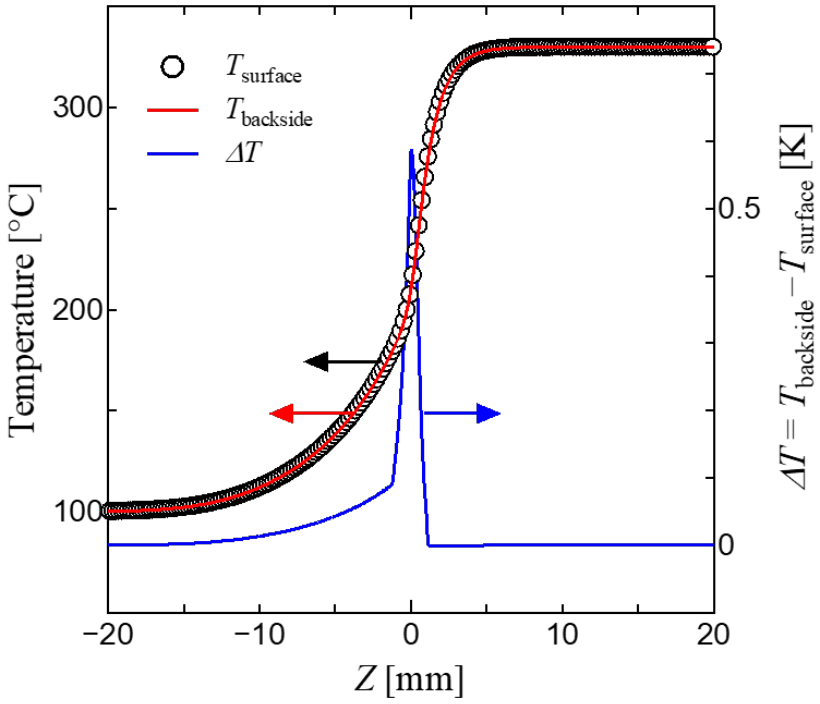

Figure A-1: Comparison of the temperature profiles on the front and back sides of the copper plate

ence method described in Sec. 2.4.1 (T_{w0} = 330°C, Γ = 0.24 kg/m·s, δ = 0.1 mm for copper plate and 0.02 mm for blackbody paint layer) are displayed in Fig. A-1. The location at which z is equal to zero indicates the peak position of HTC. The maximum temperature difference is about 0.6 K at the wetting front and small as expected from the Biot number calculation shown above. It can hence be assumed that the temperature difference between the two faces of the copper plate was sufficiently small in the present experiments.

Appendix B

Calculation method of the minimum heat flux point

The minimum heat flux point was determined using the boiling curve obtained by the inverse analysis. Figure B-1 shows the enlarged boiling curves for distilled water presented in Fig. 4-4(b). In these cases, the wall superheat at the minimum heat flux point ΔT_{MHF} can simply be defined as the value of ΔT_{w} at the local minimum of the heat flux. However, when rapid temperature reduction occurred at higher temperature, the minimum heat flux point was not obvious. The method to determine ΔT_{MHF} in this case is described in Fig. B-2 using the third run in the silica nanofluid as an example. In the experiment, the heat flux was kept increasing as shown in the figure. The temporal derivative of heat flux dq/dt is also plotted in Fig. B-2. In this work, the value of ΔT_{w} at the local minimum point of dq/dt just before the value of dq/dt was kept increasing was regarded as the minimum heat flux point ΔT_{MHF}.

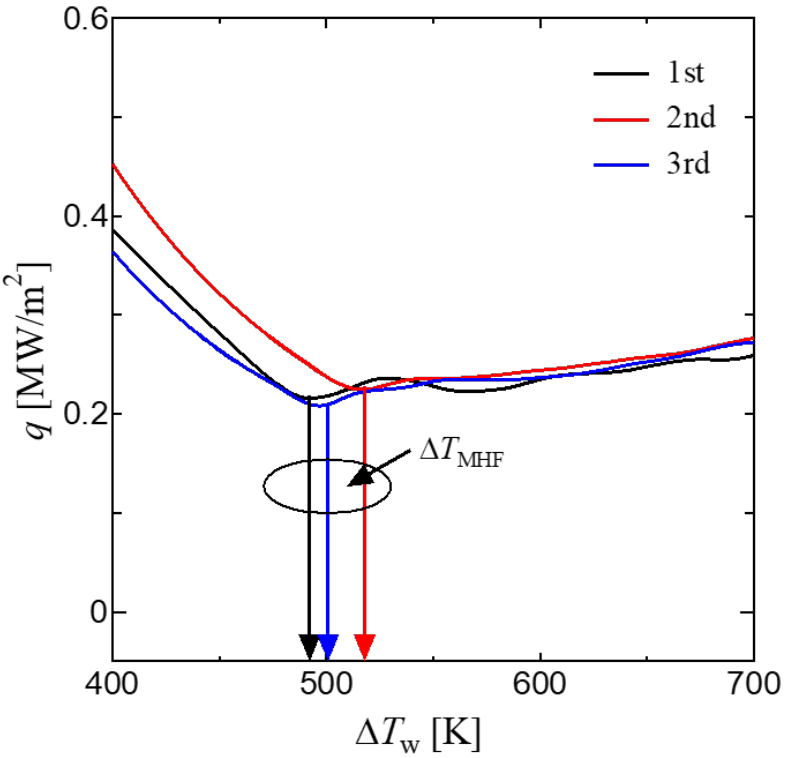

Figure B-1: Boiling curves in distilled water to determine minimum heat flux point

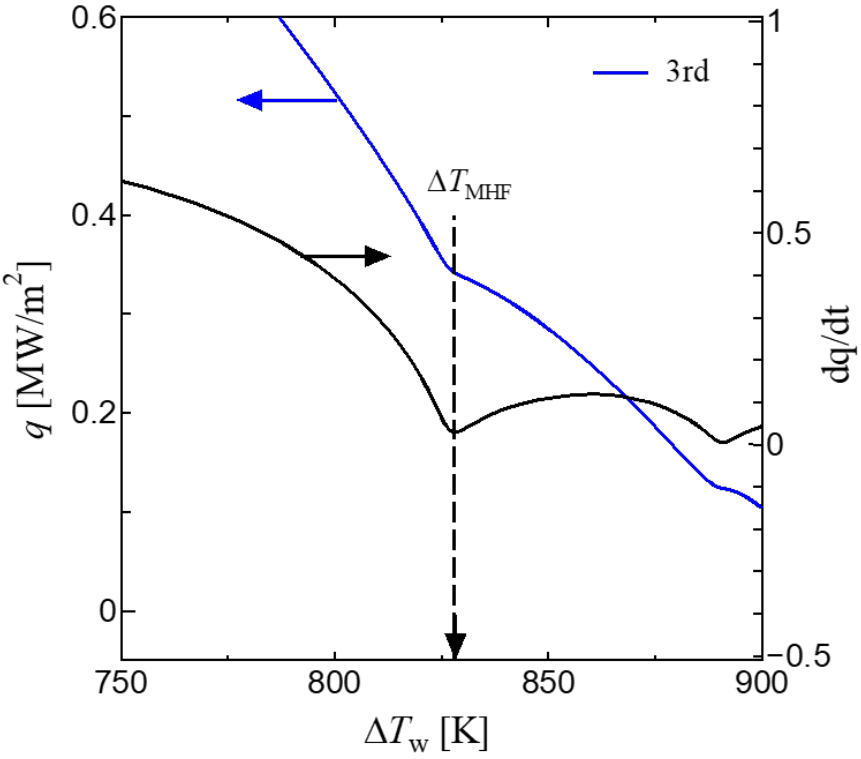

Figure B-2: Boiling curves in silica nanofluid to determine minimum heat flux point

Appendix C

Uncertainty analysis

This chapter shows the uncertainty analysis of HTC in Chapters 2 and 5 for a typical experimental condition. The methods of uncertainty analysis were referred Shiibara's method [102].

C.1 Uncertainty of HTC in Chapter 2

In Chapter 2, HTC distribution was calculated from temperature distribution by IR camera using

$$h = \frac{\delta \left\{ \dfrac{\partial}{\partial x}\left(\lambda \dfrac{\partial T_{\mathrm{wall}}}{\partial x}\right) + \dfrac{\partial}{\partial z}\left(\lambda \dfrac{\partial T_{\mathrm{wall}}}{\partial z}\right) - \dfrac{\partial}{\partial t}\left(\rho c T_{\mathrm{wall}}\right) \right\}}{T_{\mathrm{wall}} - T_{\mathrm{sat}}}$$

The uncertainty of instantaneous and local HTC was estimated following three terms.

1. Thermal diffusion term

$$\lambda_{Cu}\delta_{Cu}\left\{\left(\frac{\partial^2 T_{\mathrm{wall}}}{\partial x^2}\right) + \left(\frac{\partial^2 T_{\mathrm{wall}}}{\partial z^2}\right)\right\}$$

2. Thermal inertia term

$$\delta_{Cu}\frac{\partial}{\partial t}\left(\rho c T_{\mathrm{wall}}\right)$$

3. Temperature difference

$$T_{\text{wall}} - T_{\text{sat}}$$

Following analysis was based on a typical experimental condition(T_{w0} = 360 °C, Γ = 0.24 kg/m·s).

C.1.1 The uncertainty of thermal diffusion term

The uncertainty of thermal diffusion term was considered from two terms.

$$D_1 = \lambda_{Cu}\delta_{Cu}$$

$$D_2 = \frac{\partial^2 T_{\text{wall}}}{\partial x^2} + \frac{\partial^2 T_{\text{wall}}}{\partial z^2}$$

Table C.1 shows the uncertainty factor of D_1.

Table C.1: The uncertainty factor of D_1

Uncertainty factor	Accuracy B	Precision S	Sensitivity θ
Thermal conductivity λ_{Cu} 466.2 ± 2.0 W/m·K	B_{D11} = 2.0 W/m·K		θ_{D11} = 1.0×10^{-4} m
Thickness of copper plate δ_{Cu} 0.1 ± 0.01 mm	B_{D12} = 1.0×10^{-5} m		θ_{D12} = 466.2 W/m·K

Based on the Table C.1, the uncertainty of D_1 is :

- Accuracy

$$B_{D1} = \sqrt{(B_{D11} \times \theta_{D11})^2 + (B_{D12} \times \theta_{D12})^2} = 4.7 \times 10^{-3} \text{ W/K}$$

- Precision

$$S_{D1} = 0$$

- Uncertainty(95%)

$$U_{D1} = \sqrt{(B_{D1})^2 + (2 \times S_{D1})^2} = 4.7 \times 10^{-7} \text{ W/K}$$

Table C.2 shows the uncertainty factor of D_2.

Table C.2: The uncertainty factor of D_2

Uncertainty factor	Accuracy B	Precision S	Sensitivity θ
Temperature measurement $\lvert\Delta T_{\mathrm{w}}\rvert_x$ = 0.015 K $\lvert\Delta T_{\mathrm{w}}\rvert_z$ = 0.003 K		S_{D21} = 0.001 K	θ_{D21} = 4.0×10^{8} m^{-2}
Pixel size in z direction Δz 0.07 ± 0.001 mm		S_{D22} = 1.0×10^{-6} m	θ_{D22} = -1.7 × 10^{10} K/m^3
Pixel size in x direction Δx 0.07 ± 0.001 mm		S_{D23} = 1.0×10^{-6} m	θ_{D23} = -8.7 × 10^{10} K/m^3

Sensitivity was calculated by

$$\theta_{D21} = \frac{1}{(\Delta x)^2} + \frac{1}{(\Delta z)^2}$$

$$\theta_{D22} = \frac{-2|\Delta T_{\mathrm{w}}|_z}{(\Delta z)^3}$$

$$\theta_{D23} = \frac{-2|\Delta T_{\mathrm{w}}|_x}{(\Delta x)^3}$$

Based on the Table C.2, the uncertainty of D_2 is :

- Precision

$$S_{D2} = \sqrt{(S_{D21} \times \theta_{D21})^2 + (S_{D22} \times \theta_{D22})^2 + (S_{D23} \times \theta_{D23})^2} = 4.17 \times 10^5 \text{ K/m}^2$$

- Uncertainty(95%)

$$U_{D2} = \sqrt{(2 \times S_{D2})^2} = 8.35 \times 10^5 \text{ K/m}^2$$

Table C.3 summarized the uncertainty of thermal diffusion term.

Table C.3: The uncertainty factor of thermal diffusion term

Uncertainty factor	Accuracy B	Precision S	Sensitivity θ
Uncertainty of D_1 Ave.D_1 = 0.04 W/K	B_{D1} = 4.7×10^{-3} W/K	S_{D1} = 0 W/K	θ_{D1} = 3.67×10^{6} K/m^2
Uncertainty of D_2 Ave.D_2 = 3.67×10^{6} K/m^2		S_{D2} = 4.17×10^{5} K/m^2	θ_{D2} = 4.6×10^{-2} W/K

Based on the Table C.3, the uncertainty of D is :

- Accuracy

$$B_D = \sqrt{(B_{D1} \times \theta_{D1})^2} = 1.71 \times 10^4 \text{ W/m}^2$$

- Precision

$$S_D = \sqrt{(S_{D1} \times \theta_{D1})^2 + (S_{D2} \times \theta_{D2})^2} = 1.94 \times 10^4 \text{ W/m}^2$$

- Uncertainty(95%)

$$U_D = \sqrt{B_D^2 + (2 \times S_D)^2} = 4.25 \times 10^4 \text{ W/m}^2$$

C.1.2 The uncertainty of thermal inertia term

The uncertainty of thermal inertia term was considered from separated two terms.

$$I_1 = c_{Cu}\rho_{Cu}\delta_{Cu} \tag{C.1}$$

$$I_2 = \frac{\partial T_{\text{wall}}}{\partial t} \tag{C.2}$$

Table C.4 shows the uncertainty factor of D_1.

Based on the Table C.4, the uncertainty of I_1 is :

Table C.4: The uncertainty factor of I_1

Uncertainty factor	Accuracy B	Precision S	Sensitivity θ
Specific heat of copper plate 386 ± 5 J/kg·K	B_{I11} = 5 J/kg·K		θ_{I11} = 8.8×10^{-1} kg/m^2
Density of copper plate 8840 ± 2 kg/m^3	B_{I12} = 2 kg/m^3		θ_{I12} = $3.8 \times 10^{-}2$ J·m/kg·K
Thickness of copper plate 0.1 ± 0.01 mm	B_{I13} = 1.0×10^{-5} m		θ_{I13} = 3.4×10^{6} J/m^3·K

- Accuracy

$$B_{I1} = \sqrt{(B_{I11} \times \theta_{I11})^2 + (B_{I12} \times \theta_{I12})^2 + (B_{I13} \times \theta_{I13})^2} = 34.4 \text{ J/m}^2 \cdot \text{K}$$

- Precision

$$S_{I1} = 0$$

- Uncertainty(95%)

$$U_{I1} = \sqrt{(B_{I1})^2 + (2 \times S_{I1})^2} = 34.4 \text{ J/m}^2 \cdot \text{K}$$

Table C.5 shows the uncertainty factor of I_2.

Table C.5: The uncertainty factor of I_2

Uncertainty factor	Accuracy B	Precision S	Sensitivity θ
Temperature measurement		S_{I21} = 0.001 K	θ_{I21} = 2000 s^{-1}
frame rate Δt			

Based on the Table C.5, the uncertainty of I_2 is :

- Precision

$$S_{I2} = \sqrt{(S_{I21} \times \theta_{I21})^2} = 2 \text{ K/s}$$

- Uncertainty(95%)

$$U_{I1} = \sqrt{(2 \times S_{I2})^2} = 4 \text{ K/s}$$

Table C.6 summarized the uncertainty of thermal inertia term.

Table C.6: The uncertainty factor of thermal inertia term

Uncertainty factor	Accuracy B	Precision S	Sensitivity θ
Uncertainty of I_1 Ave.I_1 = 341 J/m^2·K	B_{I1} = 34.4 J/m^2· K	S_{I1} = 0 J/m^2· K	θ_{I1} = 100 K/s
Uncertainty of I_2 Ave.I_2 = 100 K/s		S_{I2} = 2 K/s	θ_{I2} = 341 J/m^2·K

Based on the Table C.6, the uncertainty of I is :

- Accuracy

$$B_I = \sqrt{(B_{I1} \times \theta_{I1})^2} = 3.44 \times 10^3 \text{ W/m}^2$$

- Precision

$$S_I = \sqrt{(S_{I1} \times \theta_{I1})^2 + (S_{I2} \times \theta_{I2})^2} = 683 \text{ W/m}^2$$

- Uncertainty(95%)

$$U_I = \sqrt{B_I^2 + (2 \times S_I)^2} = 4.7 \times 10^3 \text{ W/m}^2$$

C.1.3 The uncertainty of temperature difference

Table C.7 summarized the uncertainty factor of temperature difference ΔT.

Table C.7: The uncertainty factor of temperature difference

Uncertainty factor	Accuracy B	Precision S	Sensitivity θ
Uncertainty of T_{wall}	B_{DT1} = 0.43 K	S_{DT1} = 1.57 K	θ_{DT1} = 1
Uncertainty of T_{sat}	B_{DT2} = 0.01 K		θ_{DT2} = 1

Based on the Table C.7, the uncertainty of temperature difference is :

- Accuracy

$$B_{DT} = \sqrt{(B_{DT1} \times \theta_{DT1})^2 + (B_{DT2} \times \theta_{DT2})^2} = 0.44 \text{ K}$$

- Precision

$$S_{DT} = \sqrt{(S_{DT1} \times \theta_{DT1})^2} = 1.57 \text{ K}$$

- Uncertainty(95%)

$$U_{DT} = \sqrt{B_{DT}^2 + (2 \times S_{DT})^2} = 3.89 \times 10^4 \text{ K}$$

C.1.4 The uncertainty of HTC

Finally, the uncertainty of HTC was calculated by using above results. Table C.8 summarized the uncertainty of HTC.

Table C.8: The uncertainty factor of HTC

Uncertainty factor	Accuracy B	Precision S	Sensitivity θ
Uncertainty of D Ave. |D| = 5.82×10^5	B_{h1} = 1.71×10^4 W/m^2	S_{h1} = 1.94×10^4 W/m^2	θ_{h1} = 0.1 K^{-1}
Uncertainty of I Ave. |I| = 1.0×10^7	B_{h2} = 3.44×10^3 W/m^2	S_{h2} = 683 W/m^2	θ_{h2} = -0.1 K^{-1}
Uncertainty of ΔT Ave. |ΔT| = 260 K	B_{h3} = 0.44 K	S_{h3} = 1.57 K	θ_{h3} = 142 W/m$^2\cdot$ K^2

Sensitivity θ_{h4} was calculated by

$$\theta_{h3} = -\frac{D - I}{(\Delta T)^2}$$

Based on the Table C.8, the uncertainty of instantaneous and local HTC is :

- Accuracy

$$B_h = \sqrt{(B_{h1} \times \theta_{h1})^2 + (B_{h2} \times \theta_{h2})^2 + (B_{h3} \times \theta_{h3})^2} = 1.74 \times 10^3 \text{ W/m}^2 \cdot \text{K}$$

- Precision

$$S_h = \sqrt{(S_{h1} \times \theta_{h1})^2 + (S_{h2} \times \theta_{h2})^2 + (S_{h3} \times \theta_{h3})^2} = 1.96 \times 10^5 \text{ W/m}^2 \cdot \text{K}$$

- Uncertainty(95%)

$$U_h = \sqrt{B_h^2 + (2 \times S_h)^2} = 4.29 \times 10^3 \text{ W/m}^2 \cdot \text{K}$$

In a typical experimental condition (T_{w0} = 360 °C, Γ = 0.24 kg/m·s, h_{IL} = 100 kW/m^2· K), the relative uncertainty of instantaneous and local HTC was estimated as follows.

- Relative accuracy : $B_h/h_{\text{IL}} = 1.7$ %
- Relative precision : $S_h/h_{\text{IL}} = 1.9$ %
- Relative uncertainty(95%): $U_h/h_{\text{IL}} = \underline{4.3\ \%}$

When HTC is spatial and time averaged, the uncertainty of HTC is: (In a typical experimental condition, $h_{typical}$ = 26 kW/m^2·K)

- Accuracy :

$$B_{\bar{h}} = \sqrt{(B_{h1} \times \theta_{h1})^2 + (B_{h4} \times \theta_{h4})^2} = 62.8 \text{ W/m}^2 \cdot \text{K}$$

- Uncertainty(95%):

$$U_{\bar{h}} = B_{\bar{h}} = 62.8 \text{ W/m}^2 \cdot \text{K}$$

From the above calculations, the relative uncertainty of spatial and time averaged HTC is:

- Relative accuracy : $B_{\bar{h}}/h_{typical} = 0.2$ %
- Relative uncertainty(95%): $U_{\bar{h}}/h_{typical} = 0.2$ %

C.2 Uncertainty of HTC in Chapter 3

In Chapter 3, HTC distribution was calculated from temperature distribution by IR camera using

$$\rho c \frac{\partial T}{\partial t} = \frac{\partial}{\partial x}\left(\lambda \frac{\partial T}{\partial x}\right) + \frac{\partial}{\partial y}\left(\lambda \frac{\partial T}{\partial y}\right) + \frac{\partial}{\partial z}\left(\lambda \frac{\partial T}{\partial z}\right) \tag{C.3}$$

Based on the calculated temperature distribution in y-direction (thickness direction), HTC was calculated by

$$h = \frac{-\lambda(T_{(y=0)})\frac{T_{(y=0)} - T_{(y=dy)}}{dy}}{T_{(y=0)} - T_{sat}} \tag{C.4}$$

The uncertainty of instantaneous and local HTC was considered from two terms.

$$Q = -\lambda(T_{(y=0)})\frac{T_{(y=0)} - T_{(y=dy)}}{dy}$$

$$DT = T_{(y=0)} - T_{sat}$$

Following analysis was based on a typical experimental condition(T_{w0} = 250 °C, Γ = 0.28 kg/m·s)

C.2.1 The uncertainty of heat flux

Table C.9: The uncertainty factor of Q

Uncertainty factor	Accuracy B	Precision S	Sensitivity θ
Thermal conductivity λ_{Si} 88.9 ± 2.0 W/m·K	B_{Q1} = 2.0 W/m·K		θ_{Q1} = 1700 K/m
Temperature measurement 0.034 K		S_{Q2} = 0.001 K	θ_{Q2} = 4.4×10^6 W/m^2·K
Pixel size in y direction Δ y 0.02 mm			

The uncertainty of Δ y is negligible. Based on the Table C.9, the uncertainty of Q is :

- Accuracy

$$B_Q = \sqrt{(B_{Q1} \times \theta_{Q1})^2} = 3400 \text{ W/m}^2$$

- Precision

$$S_Q = \sqrt{(S_{Q2} \times \theta_{Q2})^2} = 4.4 \times 10^3 \text{ W/m}^2$$

- Uncertainty(95%)

$$U_Q = \sqrt{B_Q^2 + (2 \times S_Q)^2} = 9.5 \times 10^3 \text{ W/m}^2$$

C.2.2 The uncertainty of temperature difference

Table C.10 summarized the uncertainty factors of temperature difference ΔT.

Table C.10: The uncertainty factor of temperature difference in Si

Uncertainty factor	Accuracy B	Precision S	Sensitivity θ
Uncertainty of T_{wall}	B_{DT1} = 0.72 K	S_{DT1} = 1.05 K	θ_{DT1} = 1
Uncertainty of T_{sat}	B_{DT2} = 0.01 K		θ_{DT2} = 1

Based on the Table C.10, the uncertainty of temperature difference is :

- Accuracy

$$B_{DT} = \sqrt{(B_{DT1} \times \theta_{DT1})^2 + (B_{DT2} \times \theta_{DT2})^2} = 0.72 \text{ K}$$

- Precision

$$S_{DT} = \sqrt{(S_{DT1} \times \theta_{DT1})^2} = 1.05 \text{ K}$$

- Uncertainty(95%)

$$U_{DT} = \sqrt{B_{DT}^2 + (2 \times S_{DT})^2} = 2.22 \text{ K}$$

C.2.3 The uncertainty of HTC in Si

Finally, the uncertainty of HTC was calculated by using above results. Table C.11 summarized the uncertainty of HTC.

Table C.11: The uncertainty factor of HTC in Si

Uncertainty factor	Accuracy B	Precision S	Sensitivity θ
Uncertainty of Q = 4.6×10^5 W/m^2	B_{h1} 3400 W/m^2	S_{h1} = 4.4×10^3 W/m^2	θ_{h1} = 0.1 K^{-1}
Uncertainty of DT 150 K	B_{h2} = 0.72 K	S_{h2} 1.05 K	θ_{h2} = 3.0×10^3 W/m^2·K

Based on the Table C.11, the uncertainty of instantaneous and local HTC is :

- Accuracy

$$B_h = \sqrt{(B_{h1} \times \theta_{h1})^2 + (B_{h2} \times \theta_{h2})^2} = 2.2 \times 10^3 \text{ W/m}^2 \cdot \text{K}$$

- Precision

$$S_h = \sqrt{(S_{h1} \times \theta_{h1})^2 + (S_{h2} \times \theta_{h2})^2} = 3.2 \times 10^3 \text{ W/m}^2 \cdot \text{K}$$

- Uncertainty(95%)

$$U_h = \sqrt{B_h^2 + (2 \times S_h)^2} = 6.8 \times 10^3 \text{ W/m}^2 \cdot \text{K}$$

In a typical experimental condition (T_{w0} = 250 °C, Γ = 0.28 kg/m·s, h_{IL} = 40 kW/m^2· K), the relative uncertainty of instantaneous and local HTC was estimated as follows.

- Relative accuracy : B_h/h_{IL} = 5.6 %
- Relative precision : S_h/h_{IL} = 8.1 %
- Relative uncertainty(95%): U_h/h_{IL} = 17.2 %

Bibliography

[1] S. Lee, SUS. Choi, S. Li, and JA. Eastman. Measuring thermal conductivity of fluids containing oxide nanoparticles. *Journal of Heat Transfer*, 121:280–288, 1999.

[2] S. Pil. Jang and SUS. Choi. Effects of various parameters on nanofluid thermal conductivity. *Journal of Heat Transfer*, 129:617–623, 2007.

[3] S. M. Kwark, R. Kumar, G. Moreno, J. Yoo, and S. M. You. Pool boiling characteristics of low concentration nanofluids. *International Journal of Heat and Mass Transfer*, 53(5-6):972–981, 2010.

[4] M. Tariq, M. Abdelhamid, Y. Li, M. Omar, and Y. Zhou. Fusion of thermal and visible acquisitions for evaluating production-borne scratches and shunts in photo-voltaic pv cells. *Journal of Materials Science Research*, 1(4):57, 2012.

[5] I. Hamberg, A. Hjortsberg, and C. G. Granqvist. High quality transparent heat reflectors of reactively evaporated indium tin oxide. *Applied Physics Letters*, 40(5):362–364, 1982.

[6] S. K. W. Yu, P. R. Farmer, and M. W. E. Coney. Methods and correlations for the prediction of quenching rates on hot surfaces. *International Journal of Multiphase Flow*, 3(5):415–443, 1977.

[7] Y. Ye, J. Cai, X. Jiang, D. Dai, and D. Deng. Influence of groove type on welding-induced residual stress, deformation and width of sensitization region in a sus304 steel butt welded joint. *Advances in Engineering Software*, 86:39–48, 2015.

[8] I. Hernando, M. A. Renderos, M. Cortina, J. E. Riz, J. I. Arrizubieta, and A. Lamikiz. Inconel 718 laser welding simulation tool based on a moving heat source and phase change. *Procedia CIRP*, 74:674–678, 2018.

[9] Y. Kikuchi, T. Hori, and I. Michiyoshi. The effect of thin insulating layer on heat transfer characteristics during quenching of hot metals in saturated water. *Transactions of the Iron and Steel Institute of Japan*, 26(6):576–581, 1986.

[10] JSME. *JSME Data Book: Heat Transfer*, page 320. Japan Society of Mechanical Engineers, fourth edition, 1986.

[11] E. W. Lemmon, I. H. Bell, M. L. Huber, and M. O. McLinden. Nist standard reference database 23: Reference fluid thermodynamic and transport properties-refprop, version 10.0, national institute of standards and technology. *Standard Reference Data Program, Gaithersburg*, 2018.

[12] S. Nukiyama. The maximum and minimum values of the heat q transmitted from metal to boiling water under atmospheric pressure. *International Journal of Heat and Mass Transfer*, 9(12):1419–1433, 1966.

[13] T. Ueda. *Gas-Liquid Two-Phase Flow (Fluid Flow and Heat Transfer)*, chapter 19.4. Yokendo Publishing Co., 1989.

[14] P. B. Whalley. *Boiling, Condensation, and Gas-Liquid Flow*, chapter 21. Clarendon Press, 1987.

[15] Jr. R. T. Lahey and F. J. Moody. *The Thermal-Hydraulics of a Boling Water Nuclear Reactor (second ed.)*, chapter 8.5.2. American Nuclear Society, 1993.

[16] J. G. Leidenfrost. De aque communis nonnullis qualitatibus tractatus, duisburg on rhine. *International Journal of Heat and Mass Transfer*, 9(1966):1153–1166, 1756.

[17] E. Elias and G. Yadigaroglu. A general one-dimensional model for conduction-controlled rewetting of a surface. *Nuclear Engineering and design*, 42(2):185–194, 1977.

[18] A. Yamanouchi. Effect of core spray cooling in transient state after loss of coolant accident. *Journal of Nuclear Science and Technology*, 5(11):547–558, 1968.

[19] R. B. Duffey and D. T. C. Porthouse. The physics of rewetting in water reactor emergency core cooling. *Nuclear Engineering and Design*, 25(3):379–394, 1973.

[20] C. L. Tien and L. S. Yao. Analysis of conduction-controlled rewetting of a vertical surface. *J. Heat Transfer*, 97:161–165, 1975.

[21] J. M. Blair. An analytical solution to a two-dimensional model of the rewetting of a hot dry rod. *Nuclear Engineering and Design*, 32(2):159–170, 1975.

[22] T. S. Thompson. An analysis of the wet-side heat-transfer coefficient during rewetting of a hot dry patch. *Nuclear Engineering and Design*, 22(2):212–224, 1972.

[23] S. S. Dua and C. L. Tien. Two-dimensional analysis of conduction-controlled rewetting with precursory cooling. *J. Heat Transfer*, 98:407–413, 1976.

[24] K. H. Sun, G. E. Dix, and C. L. Tien. Cooling of a very hot vertical surface by a falling liquid film. *Transactions of American Society of Mechanical Engineers, Ser. C*, 96:126–131, 1974.

[25] W. M. Rohsenow. A method of correlating heat transfer data for surface boiling of liquids. *Transactions of ASME*, 74:969–976, 1952.

[26] K. Ramu and J. Weisman. A meth0d f0r the correlation of transition boiling heat transfer data. In *International Heat Transfer Conference 5*, 1974.

[27] L. A. Bromley. Heat transfer in stable film boiling. *Chemical Engineering Progress*, 46:221–227, 1950.

[28] K. H. Sun, G. E. Dix, and C. L. Tien. Effect of precursory cooling on falling-film rewetting. *J. Heat Transfer*, 97:360–365, 1975.

[29] P. Spiegler, J. Hopenfeld, M. Silberberg, CF. Bumpus Jr, and A. Norman. Onset of stable film boiling and the foam limit. *International Journal of Heat and Mass Transfer*, 6(11):987–989, 1963.

[30] J. H. Lienhard. Correlation for the limiting liquid superheat. *Chemical Engineering Science*, 31(9):847–849, 1976.

[31] P. J. Berenson. Film-boiling heat transfer from a horizontal surface. *J. Heat Transfer*, 83:351–356, 1961.

[32] J. J. Carbajo. A study on the rewetting temperature. *Nuclear Engineering and Design*, 84(1):21–52, 1985.

[33] P. A. Howard. An experimental and analytical study of the sputtering phenomena. 1975.

[34] G. L. Shires, A. R. Pickering, and P. T. Blacker. Film cooling of vertical fuel rods. Technical report, United Kingdom Atomic Energy Authority, 1964.

[35] S. K . Das, SUS. Choi, and H. E. Patel. Heat transfer in nanofluids—a review. *Heat transfer engineering*, 27(10):3–19, 2006.

[36] SUS. Choi, D. A. Singer, H. P. Wang, et al. Developments and applications of non-newtonian flows. *Asme Fed*, 66:99–105, 1995.

[37] H. Kim, J. Kim, and M. H. Kim. Effect of nanoparticles on chf enhancement in pool boiling of nano-fluids. *International Journal of Heat and Mass Transfer*, 49(25-26):5070–5074, 2006.

[38] H. D. Kim and M. H. Kim. Effect of nanoparticle deposition on capillary wicking that influences the critical heat flux in nanofluids. *Applied physics letters*, 91(1):014104, 2007.

[39] H. T. Phan, N. Caney, P. Marty, S. Colasson, and J. Gavillet. Surface wettability control by nanocoating: the effects on pool boiling heat transfer and nucleation mechanism. *International Journal of Heat and Mass Transfer*, 52(23-24):5459–5471, 2009.

[40] H. S. Ahn, H. J. Jo, S. H. Kang, and M. H. Kim. Effect of liquid spreading due to nano/microstructures on the critical heat flux during pool boiling. *Applied Physics Letters*, 98(7):071908, 2011.

[41] A. Bolukbasi and D. Ciloglu. Pool boiling heat transfer characteristics of vertical cylinder quenched by sio2–water nanofluids. *International Journal of Thermal Sciences*, 50(6):1013–1021, 2011.

[42] T. Okawa, M. Takamura, and T. Kamiya. Boiling time effect on chf enhancement in pool boiling of nanofluids. *International Journal of Heat and Mass Transfer*, 55(9-10):2719–2725, 2012.

[43] L. W. Fan, J. Q. Li, D. Y. Li, L. Zhang, Z. T. Yu, and K. F. Cen. The effect of concentration on transient pool boiling heat transfer of graphene-based aqueous nanofluids. *International Journal of Thermal Sciences*, 91:83–95, 2015.

[44] Y. Watanabe, K. Enoki, and T. Okawa. Nanoparticle layer detachment and its influence on the heat transfer characteristics in saturated pool boiling of nanofluids. *International Journal of Heat and Mass Transfer*, 125:171–178, 2018.

[45] S. J. Kim, I. C. Bang, J. Buongiorno, and L. W. Hu. Surface wettability change during pool boiling of nanofluids and its effect on critical heat flux. *International Journal of Heat and Mass Transfer*, 50(19-20):4105–4116, 2007.

[46] D. Wen and Y. Ding. Experimental investigation into the pool boiling heat transfer of aqueous based γ-alumina nanofluids. *Journal of Nanoparticle Research*, 7(2):265–274, 2005.

[47] R. Kamatchi and S. Venkatachalapathy. Parametric study of pool boiling heat transfer with nanofluids for the enhancement of critical heat flux: a review. *International Journal of Thermal Sciences*, 87:228–240, 2015.

[48] S. M. Kwark, G. Moreno, R. Kumar, H. Moon, and S. M. You. Nanocoating characterization in pool boiling heat transfer of pure water. *International Journal of Heat and Mass Transfer*, 53(21-22):4579–4587, 2010.

[49] H. Kim, G. DeWitt, T. McKrell, J. Buongiorno, and L. W. Hu. On the quenching of steel and zircaloy spheres in waterbased nanofluids with alumina, silica and diamond nanoparticles. *International Journal of Multiphase Flow*, 35(5):427–438, 2009.

[50] S. Kim, H. D. Kim, H. Kim, H. S. Ahn, H. Jo, J. Kim, and M. H. Kim. Effects of nano-fluid and surfaces with nano structure on the increase of chf. *Experimental thermal and fluid science*, 34(4):487–495, 2010.

[51] D. Ciloglu and A. Bolukbasi. The quenching behavior of aqueous nanofluids around rods with high temperature. *Nuclear Engineering and Design*, 241(7):2519–2527, 2011.

[52] J. Kang, T. K. Kim, G. C. Lee, H. S. Park, and M. H. Kim. Minimum heat flux and minimum film-boiling temperature on a completely wettable surface: effect of the bond number. *International Journal of Heat and Mass Transfer*, 120:399–410, 2018.

[53] Y. Kikuchi, T. Hori, and I. Michiyoshi. Minimum film boiling temperature for cooldown of insulated metals in saturated liquid. *International Journal of Heat and Mass Transfer*, 28(6):1105–1114, 1985.

[54] G. R. Chandratilleke, S. Nishio, and H. Ohkubo. Pool boiling heat transfer to saturated liquid helium from coated surface. *Cryogenics*, 29(6):588–592, 1989.

[55] E. Abu-Nada. Effects of variable viscosity and thermal conductivity of cuo-water nanofluid on heat transfer enhancement in natural convection: mathematical model and simulation. *J. Heat Transfer*, 132, 2010.

[56] H. Otake, Y. Koizumi, and A. Takahashi. Study on rewetting of vertical-hot-thick surface by a falling film. investigation from the aspect of boiling heat transfer characteristics and modeling. *Transactions of the Japan Society of Mechanical Engineers. Part B*, 64, 1998.

[57] T. Ueda. *Gas-Liquid Two-Phase Flow (Fluid Flow and Heat Transfer)*, chapter 12.3. Yokendo Publishing Co., 1989.

[58] Y. Katto and K. Ishii. Forced liquid supply by plane jet, burnout of high heat flux boiling system. *Trans. JSME*, 81:690, 1978.

[59] A. K. Mozumder, M. Monde, and P. L. Woodfield. Delay of wetting propagation during jet impingement quenching for a high temperature surface. *International Journal of Heat and Mass Transfer*, 48(25-26):5395–5407, 2005.

[60] W. Nusselt. Die oberfluchenkondensation des wasserdampfes. *Z. VDI*, 60(28):569, 1916.

[61] H. Takahama and S. Kato. Longitudinal flow characteristics of vertically falling liquid films without concurrent gas flow. *International Journal of Multiphase Flow*, 6(3):203–215, 1980.

[62] F. P. Incropera and D. P. Dewitt. *Fundamentals of Heat and Mass Transfer (fourth ed.)*, chapter 10. John Wiley & Sons, 1996.

[63] W. Wilke. *Wärmeübergang an Rieselfilme: Mitteilung d. Forschungsgruppe f. Wärme-u. Kältetechnik im Max-Planck-Inst. f. Strömungsforschung, Göttingen.* PhD thesis, VDI-Verlag, 1962.

[64] R. Takahashi and Y. Tanamachi. *Finite difference method*, chapter 4.4. Baifukan, 1991.

[65] S. K. Sahu, P. K. Das, and S. Bhattacharyya. Analytical and semi-analytical models of conduction controlled rewetting: a state of the art review. *Thermal Science*, 19(5):1479–1496, 2015.

[66] Z. Z. You. Combined afm, xps, and contact angle studies on treated indium–tin-oxide films for organic light-emitting devices. *Materials letters*, 61(18):3809–3814, 2007.

[67] E. R. Eckert and T. W. Jackson. Analysis of turbulent free-convection boundary layer on flat plate. Technical report, National Aeronautics and Space Administration Washington DC, 1950.

[68] S. K. Sahu, P. K. Das, and S. Bhattacharyya. Rewetting analysis of hot vertical surfaces with precursory cooling by the heat balance integral method. *Journal of heat transfer*, 130(2), 2008.

[69] M Monde and Y Katto. Burnout in a high heat-flux boiling system with an impinging jet. *International Journal of Heat and Mass Transfer*, 21(3):295–305, 1978.

[70] M. Monde. Heat transfer characteristics during quench of high temperature solid. *Journal of Thermal Science and Technology*, 3(2):292–308, 2008.

[71] K. Tsukamoto, Y. Kita, S. Inoue, T. Hamanosono, S. Hidaka, S. Ueoka, H. Fukuda, M. Kohno, and Y. Takata. On the onset of quench during spray cooling: The significance of oxide layers. *Applied Thermal Engineering*, 179:115682, 2020.

[72] T. Nakamura, H. Okawa, Y. Kawamura, and K. Sugawara. Solid–liquid separation by sonochemistry: A new approach for the separation of mineral suspensions. *Ultrasonics Sonochemistry*, 18(1):85–91, 2011.

[73] M. Monde, H. Arima, and Y. Mitsutake. Estimation of surface temperature and heat flux using inverse solution for one - dimensional heat conduction. *Journal of Heat Transfer*, 125(2):213–223, 2003.

[74] M. Monde, H. Arima, W. Liu, Y. Mitsutake, and J. A. Hammad. An analytical solution for two -dimensional inverse heat conduction problems using laplace transform. *International Journal of Heat and Mass Transfer*, 46(12):2135–2148, 2003.

[75] P. L Woodfield, M. Monde, and Y. Mitsutake. Implementation of an analytical two-dimensional inverse heat conduction technique to practical problems. *International Journal of Heat and Mass Transfer*, 49(1-2):187–197, 2006.

[76] P. L Woodfield, M. Monde, and Y. Mitsutake. Improved analytical solution for inverse heat conduction problems on thermally thick and semi-infinite solids. *International Journal of Heat and Mass Transfer*, 49(17-18):2864–2876, 2006.

[77] N. Zuber. On the stability of boiling heat transfer. *Trans. Am. Soc. Mech. Engrs*, 80, 1958.

[78] V. K. Dhir and G. P. Purohit. Subcooled film-boiling heat transfer from spheres. *Nuclear Engineering and Design*, 47(1):49–66, 1978.

[79] V. Saeid and T. Borca-Tasciuc. Role of nanoparticles on nanofluid boiling phenomenon: Nanoparticle deposition. *Chemical Engineering Research and Design*, 92(5):842–856, 2014.

[80] H. Kim, J. Buorgiorno, L. W. Hu, and T. McKrell. Nanoparticle deposition effects on the minimum heat flux point and quench front speed during quenching in water-based alumina nanofluids. *International Journal of Heat and Mass Transfer*, 53(7-8):1542–1553, 2010.

[81] M. M. Rahman, E. Olceroglu, and M. McCarthy. Role of wickability on the critical heat flux of structured superhydrophilic surfaces. *Langmuir*, 30(37):11225–11234, 2014.

[82] J. Q. Li, J. Y. Zhang, L. W. Mou, Y. H. Zhang, and L. W. Fan. Enhanced transitional heat flux by wicking during transition boiling on microporous hydrophilic and superhydrophilic surfaces. *International Journal of Heat and Mass Transfer*, 141:835–844, 2019.

[83] F. P. Incropera, D. P. Dewitt, T. L . Bergman, and A. S. Lavine. *Fundamentals of Heat and Mass Transfer*. John Wiley & Sons, sixth edition, 2007.

[84] W. S. Bradfield. Liquid-solid contact in stable film boiling. *Industrial & Engineering Chemistry Fundamentals*, 5:200–204, 1963.

[85] S. C. Yao and R. E. Henry. An investigation of the minimum film boiling temperature on horizontal surfaces. *Journal of Heat Transfer*, 100:260–267, 1978.

[86] Y. Kikuchi, T. Ebisu, and I. Michiyoshi. Measurement of liquid-solid contact in film boiling. *International Journal of Heat and Mass Transfer*, 35:1589–1594, 1992.

[87] E. Yajima, R. Ichikawa, K. Furusawa, T. Miyazaki, K. Kosakai, and Y. Nishino. *Wakai gijyutusha notameno kikai·kinnzokuzairyou (in japanese)*, page 85. Maruzen, second edition, 2002.

[88] K. Kusabiraki, H. Nagahama, L. Wang, and T. Ooka. The growth of γ'precipitates in nickel-base superalloy. *Tetsu-to-Hagané*, 75(8):1354–1361, 1989.

[89] K. Kusabiraki, L. Wang, T. Ooka, and K. Yamada. The growth of γ'and γ"precipitates in nickel-base superalloys. *Tetsu-to-Hagané*, 76(8):1341–1348, 1990.

[90] M. Tagaya and I. Tamura. Yakiire reikyakuzai no kennkyuu (vol. 4) mizu oyobi mizu wo shuseibunntosuru ekitaino reikyakunou. *J.Japan Inst.Met.Mater.*, 16(2):107–111, 1952.

[91] M. Tagaya and I. Tamura. Yakiire reikyakuzai no kennkyuu (vol. 6) noukouenn suiyoueki no reikyakunou. *J.Japan Inst.Met.Mater.*, 16(12):652–655, 1952.

[92] M. Tagaya and I. Tamura. Yakiire reikyakuzai no kennkyuu (vol. 5) doushokubutuyu(yushi) no reikyakunou. *J.Japan Inst.Met.Mater.*, 16(6):342–346, 1952.

[93] M. Tagaya and I. Tamura. Yakiire reikyakuzai no kennkyuu (vol. 7) koubutuyu no reikyakunou. *J.Japan Inst.Met.Mater.*, 17(5):217–220, 1953.

[94] S. Owaku. Criterion of quench cracking–its sources and prevention. *Netsu Shori(Journal of the Japan Society for Heat Treatment)*, 30(2):63–67, 1990.

[95] Y. Mikita and I. Nakabayashi. Polyethylene glycol kei porima yakiire eki noreikyaku tokusei to kakiware kannjyusei. *Transactions of the JSME (in Japanese)*, 52(473):229–232, 1986.

[96] Y. Mikita, I. Nakabayashi, K. Sakamaki, and S. Hori. koutannso kuromu jikuuke kou no yakiware nikannsuru kennkyuu : (vol. 5) yakiware ni oyobosu ethylene glycol-mizu kei yakiire eki no tokusei. *Transactions of the JSME (in Japanese)*, 55(513):1116–1120, 1989.

[97] L. Godson, B. Raja, D. Mohan Lal, and S. Wongwises. Enhancement of heat transfer using nanofluids—an overview. *Renewable and sustainable energy reviews*, 14(2):629–641, 2010.

[98] S. M. You, J. H. Kim, and K. H. Kim. Effect of nanoparticles on critical heat flux of water in pool boiling heat transfer. *Applied physics letters*, 83(16):3374–3376, 2003.

[99] I. C. Bang and S. H. Chang. Boiling heat transfer performance and phenomena of Al_2O_3 water nano-fluids from a plain surface in a pool. *International Journal of Heat and Mass Transfer*, 48(12):2407–2419, 2005.

[100] C. Aoki, T. Ueno, and T. Ohno. Control of alloy 718's metallographic structures through solution heat treatment. *Hitachi Met. Rep*, 32:26–29, 2016.

[101] F. P. Incropera and D. P. Dewitt. *Fundamentals of Heat and Mass Transfer (fourth ed.)*, chapter 5. John Wiley & Sons, 1996.

[102] N. Shiibara. *Development of a New Measurement Method of Turbulent Heat Transfer Fluctuation in a Circular Tube Using an Infrared Camera and Its Application to Complex Flow.* in japanese, National Defense Academy, 2017.